Trans-Neptunian and Exosolar Satellites and Dust:

Dynamics and Surface Effects

by

Simon Bernard Porter

A Dissertation Presented in Partial Fulfillment
of the Requirement for the Degree
Doctor of Philosophy

Approved May 2013 by the
Graduate Supervisory Committee:

Steven Desch, Chair
Mikhail Zolotov
Francis Timmes
Evan Scannapieco
Mark Robinson

ARIZONA STATE UNIVERSITY

August 2013

ABSTRACT

Solar system orbital dynamics can offer unique challenges. Impacts of interplanetary dust particles can significantly alter the surfaces of icy satellites and minor planets. Impact heating from these particles can anneal away radiation damage to the crystalline structure of surface water ice. This effect is enhanced by gravitational focusing for giant planet satellites. In addition, impacts of interplanetary dust particles on the small satellites of the Pluto system can eject into the system significant amounts of secondary intra-satellite dust. This dust is primarily swept up by Pluto and Charon, and could explain the observed albedo features on Pluto's surface.

In addition to Pluto, a large fraction of trans-neptunian objects (TNOs) are binary or multiple systems. The mutual orbits of these TNO binaries can range from very wide (periods of several years) to near-contact systems (less than a day period). No single formation mechanism can explain this distribution. However, if the systems generally formed wide, a combination of solar and body tides (commonly called Kozai Cycles-Tidal Friction, KCTF) can cause most systems to tighten sufficiently to explain the observed distributions. This KCTF process can also be used to describe the orbital evolution of a terrestrial-class exoplanet after being captured as a satellite of a habitable-zone giant exoplanet. The resulting exomoon would be both potentially habitable and potenially detectable in the full Kepler data set.

TABLE OF CONTENTS

Page

LIST OF TABLES v

LIST OF FIGURES vi

CHAPTER

1 Introduction 1

2 Micrometeorite Impact Annealing of Ice in the Outer Solar System 11

2.1 Introduction 11

2.2 Modeling Micrometeorite Annealing 14

2.2.1 Theoretical Model 14

2.2.2 Implementation and Results 16

2.3 Annealing on Icy Satellites 18

2.3.1 Dust Sources 19

2.3.2 Gravitational Focusing 20

2.3.3 Ice Amorphization 22

2.3.4 Icy Satellite Results 23

2.4 Discussion 25

3 Ejecta Transfer within the Pluto System 33

3.1 Motivation 33

3.2 Simulations 35

3.3 Results 37

3.3.1 Dust Trajectories 37

3.3.2 Effects of Radiation Pressure 39

3.3.3 Impact Locations 39

3.4 Discussion 40

3.5 Conclusions 41

CHAPTER Page

4 KCTF Evolution of Trans-Neptunian Binaries:
Connecting Formation to Observation 49
4.1 Motivation 49
4.2 KCTF Model 51
4.2.1 Frictional Timescale 53
4.2.2 Quadrupole Gravity 56
4.2.3 Integration Methods 57
4.3 Monte Carlo Simulations 59
4.4 Results 61
4.4.1 Stability of Orbits to KCTF 63
4.4.2 Effects of Physical Parameters 64
4.4.3 Survival Probability 66
4.4.4 Obliquity 67
4.5 Discussion 69
4.6 Conclusions 71
4.7 Acknowledgements 72
5 Post-Capture Evolution of Potentially Habitable Exomoons 82
5.1 Motivation 82
5.2 KCTF Model 84
5.3 Monte Carlo Simulations 85
5.4 Results and Discussion 87
5.5 Conclusions 91
5.6 Acknowledgments 92
6 Conclusion 98

CHAPTER Page

6.1 Future Work 99

REFERENCES 103

LIST OF TABLES

Table Page

2.1 Results for giant planet satellites 31

2.2 Results for KBOs 32

4.1 Summary of KCTF simulation results 79

4.2 H' for observed systems with fully-constrained orbits 80

4.3 Observed TNB systems with near-circular orbits 81

5.1 Relative fraction of end states for fully evolved exomoon systems. 96

5.2 Median Exomoon orbital period, Transit Timing Variation (TTV), and Transit Duration Variation (TDV) for full-evolved exomoon systems. . . 97

LIST OF FIGURES

Figure		Page
2.1	Mass Annealed as a Function of Kinetic Energy	29
2.2	IDP and E-Ring Energy Density	30
3.1	Fraction of Nix ejecta which impact Pluto	42
3.2	Fraction of Nix ejecta which impact Charon	43
3.3	Fraction of Hydra ejecta which impact Pluto	44
3.4	Fraction of Hydra ejecta which impact Charon	45
3.5	Longitudinal distribution of impacts from Nix	46
3.6	Longitudinal distribution of impacts from Hydra	47
3.7	Longitudinal albedo maps of Pluto and Charon	48
4.1	Example of rapid KCTF evolution	73
4.2	Evolution of 1000 synthetic TNBs	74
4.3	End states for different physical properties	75
4.4	Circularization times	76
4.5	$\|H'\|$ for different physical properties	77
4.6	Final spin rate and obliquity	78
5.1	Post-capture spin-orbit evolution of two exomoons	93
5.2	Post-evolution orbital period and inclinations	94
5.3	Post-capture circularization timescales	95

Chapter 1

INTRODUCTION

In this dissertation, we show how orbital dynamics has reshaped the solar system in several ways, both in the initial chaos and in ongoing processes ever since. We show how dust can transform surfaces in the outer solar system and is a currently active geologic process. We show how solar or stellar perturbations can transform satellite orbits, for satellites ranging in size from 1 μm to an Earth mass. And we show how apparently stable orbital systems today could undergone radical alterations in their past.

The discovery of the solar system beyond Saturn was arguably the greatest astronomical revelation of the pre-photographic astronomy. The process started in 1781 when the British composer-astronomer William Herschel began looking for stellar parallax (Lodge, 1893). One of the key predictions of the Copernican heliocentric model was that because of the motion of the Earth around the Sun, the nearest stars should be in slightly different positions relative to the distant stars at different times of the year. However, because of the enormous distance of even the nearest stars, stellar parallax was not observed until nearly 60 years later with much more specialized equipment. Thus, when Herschel observed with his hand-made telescope (roughly comparable to a modern Dobsonian Newtonian with a tarnished mirror) a large blue star appearing to move, he was immediately suspicious that it was probably not a star moving due to parallax, but rather that it was a distant comet (Jones, 1947; Lodge, 1893). He described it as such in all his correspondence, but calculations soon showed the object was in a circular orbit around the Sun and must be very large to

appear so bright. Herschel had therefore discovered an entire planet unknown to the ancients, and proved Copernicus right, just not in the way he had intended.

To say Herschel's discovery transformed astronomy is an understatement. It blasted away the medieval reverence for classical astronomy and proved that there were entire new worlds just waiting to be discovered. Before Uranus, telescope science had focused on increasingly delicate refractors, excellent for bright-object astronomy, but simply unable to look very deep into the sky. Herschel, however, showed that there was plenty to be discovered by going only slightly deeper with a reflector. He used the stipend he received from King George III to construct a series of increasing larger reflecting telescopes, up to a 40 foot long telescope in a massive wooden frame (Lodge, 1893). The mirror and guiding technology would not catch up enough to make such a telescope useful until decades after Herschel's death, but the course was set of continually looking deeper to find the edge of the solar system.

The next planet, though, was not really found with a telescope, but rather a quill. After the discovery of Uranus, astronomers across Europe raced to observe it and make ever more accurate predictions of its position (Standage, 2000). However by the 1820s, it was increasingly clear that a simple Keplerian orbit would not accurately predict Uranus's position. Alexis Bouvard at the Paris Observatory proposed that another planet exterior to Uranus could be causing the perturbation (Jones, 1947). By 1845, both John Couch Adams in Cambridge and Urbain Le Verrier in Paris had produced estimates of where such a planet should be. Both contacted observers to begin the search, and 1846 Johann Gottfried Galle at the Berlin Observatory found Neptune within one degree of Le Verrier's prediction (Jones, 1947; Standage, 2000). If Uranus had been final proof of the Copernican model, Neptune was a dramatic proof of Newton's universal law of gravitation. Adams and Le Verrier had calculated the existence and position of an entire planet through the direct extrapolation of

Newtonian gravity. It was also the first inkling that orbital mechanics at the edge of the solar system could be much more complicated than the simple procession of the inner solar system.

The discovery of Neptune by perturbations on Uranus naturally led astronomers to look for perturbations on Neptune by another planet. Percival Lowell, a wealthy American travel writer, was particularly struck by the idea and in 1906 began a search for a "Trans-Neptunian Planet" using his personal observatory in Flagstaff, Arizona Territory (Levy, 1991). For this search, he exploited two technologies that unavailable to Herschel or Le Verrier, photography and the mechanical computer. With his mechanical computer, Lowell predicted the position of a planet which would account for variations that were reported in the position of Neptune. The variations were later disproved by better estimates of the mass of Neptune, but his belief in their existence prompted Lowell to start looking. Right from the start, he began to record observations with photographic plates, as the motion of any trans-neptunian planet would be so slight that it would not easily be seen visually. The search continued after Lowell's death in 1916, collecting thousands of photographic plates, until finally in 1930, when Clyde Tombaugh found something (Levy, 1991). Tombaugh, a recent college graduate working on the survey, had been methodically collecting and analyzing the plates and found an object that moved at just the right speed across the sky to be beyond Neptune. The object was of course Pluto and immediately hailed as the ninth planet.

Pluto, however, was also immediately a quandary. Since it was right at the limit of detection for telescopes of the time, there was considerable uncertainty about just how bright Pluto was. Estimates usually erred on the side of making it larger (since it was a planet after all), meaning that as better measurements were made, the reported mass of Pluto began to fall. In 1978, James Christy at the US Naval Observatory

Flagstaff Station noticed that all his images of Pluto were elongated (Christy, 1997). The elongation did not appear on other images, and resembled a binary star. Going back, he realized that the elongation varied with the same period as Pluto's lightcurve. This could only happen if Pluto was actually two similar mass objects, orbiting around each other. Thus, Charon was discovered and Pluto revealed as the first true binary of the solar system, with a total mass about 1/5 that of Earth's Moon.

After the discovery of Pluto, the Irish economist-astronomer Kenneth Edgeworth proposed that it was part of a disk of material beyond Neptune (Davies, 2001). This theory was independently echoed by the Dutch-American astronomer Gerard Kuiper ten years later (Davies, 2001). However, telescopes of the 1950s could not see deep enough to detect any such disk. This did not change until the introduction of digital photography in the 1980s, especially the Charged-Coupled Detector, or CCD. CCDs could make extremely deep images with even modest telescopes. In 1992, David Jewitt and Jane Luu used a CCD camera at the 2.2 meter telescope on Mauna Kea, Hawaii to search the ecliptic for faint objects. Sure enough, the first object they found was (15760) 1992 QB_1, a 23rd magnitude object beyond Neptune (Jewitt *et al.*, 1992). Unlike Pluto, it was in a near-circular orbit that not resonant with Neptune, just as Edgeworth and Kuiper predicted.

Soon, more and more similar objects were found, with many thousands of objects now confirmed. Most were on similar orbits to 1992 QB_1 and are typically grouped as the "classical Kuiper Belt", on low-eccentricity low-inclination orbits between 40 and 50 AU from the Sun. Some of the others were on orbits similar to Pluto in a 3:2 mean motion resonance with Neptune, others at the 2:1 mean motion resonance, and the remainder were in highly inclined and eccentric orbits. Most of the largest objects discovered were in the scattered or resonant populations, including Eris, an object of near equal size to Pluto, but which appears to have a larger mass.

As the structure of the objects beyond Neptune began to fill in, Pluto's strangeness became a more general question: why were the classical and scattered objects on such different orbits? A clue came from Neptune's orbit, which was much more circular than the other giant planets. In 1993, Renu Malhotra proposed that Pluto's orbit was a result of being captured during an outward migration of Neptune (Malhotra, 1993). This would also explain Neptune's circularity, as the result of scattering a primordial outer disk of planetesimals. As more computer simulations were performed, the modest migration initially suggested by Malhotra grew to have the giant planets all form much closer to the Sun, and Neptune migrating tens of AU outwards. This has been termed the "Nice Model" (after the city in France), and has been used to explain the positions of the giant planets, the structure of the Kuiper and Asteroid Belts, and the Late Heavy Bombardment seen on the Moon (e.g. Tsiganis *et al.*, 2005).

The key to making the Nice Model work is the assumption of a several Earth-mass disk of material originally beyond the outermost giant planet (Uranus and Neptune often swap in these simulations). This disk extended from roughly 20 AU, Uranus's current orbit, to 50 AU, the outer edge of the current classical Kuiper Belt. As Uranus and Neptune were thrown away from the center of the solar system by perturbations from Jupiter and Saturn, they destroyed most of this disk by either accreting the objects or scattering them away from the solar system. The small number of survivors were emplaced as the scattered and resonant trans-neptunian objects. The classical Kuiper Belt is therefore the last remnant of the primordial circumsolar disk.

The well preserved nature of the classical Kuiper Belt is especially exciting because of its high binary fraction. Before the discovery of Charon, objects as small as Pluto were not considered likely to have any satellites. Even then, Charon was considered a special case until the *NASA* Galileo spacecraft flew past the main-belt asteroid 243 Ida in 1993 and serendipitously discovered that it had a small satellite, Dactyl. Five

years later, the Deep Ecliptic Survey, a Lowell-led successor to the original Pluto search, discovered 1998 WW_{31}. This was a binary classical Kuiper Belt "object" that actually consisted of two objects of almost equal mass, orbiting with a period of 570 days. Since then, many more binaries have been found, with an estimate of that least 30% of classical Kuiper Belt objects are binaries (or higher), and possibly even more due to the limit of current telescope resolution (Noll *et al.*, 2008a). These binaries provide the only way to measure the mass of trans-neptunian objects. Those masses can then be used with thermal infrared measurements of the radius, thus producing density and constraining the composition of the objects.

Unlike main-belt and near-Earth asteroid binaries, trans-neptunian binaries (TNBs) are often near-equal size to each other. This is indicative of a very different formation mechanism from the main belt process of solar radiation-driven rotational fission (BYORP; Scheeres, 2007). Instead, the mass ratios would more favor dynamical capture (Goldreich *et al.*, 2002), but the separations of observed binaries are typically too closer than captures would produce (Noll *et al.*, 2008a). Some amount of post-capture orbital evolution is thus needed to explain the observations. In addition, the similarity of binaries in the three populations implies that the orbital evolution must have happened early on, before the giant planet migration.

Another consequence of the classical Kuiper Belt being well preserved is that the cratering rate in the outer solar system has been very low since the giant planet migration. Voyager 2 observed that the uranian satellites mainly have very old cratered terrain with few rayed craters (Strom, 1987). Neptune's satellite Triton, an object likely captured at the end of migration, has what Schenk and Zahnle (2007) described as "negligible surface age" with very few craters on its surface. In addition to the low cratering rate, most of the outer solar system satellites and TNOs are too small for current cryovolcanic activity (Desch *et al.*, 2009).

Thus, any new activity on the surfaces trans-neptunian objects or icy giant satellites is probably dominated by the impacts of ice-silicate interplanetary dust particles (IDPs). These particles are produced in the Kuiper Belt from impacts on objects with small enough gravity that they can not keep impact ejecta on their surfaces. The dust then travels inwards towards the Sun due to Poynting-Robertson drag, a relativistic effect on the blackbody emission of the particles. The current flux of these particles have been measured both directly by *Pioneer 10* and *New Horizons* (Humes, 1980; Poppe and Horányi, 2011) and indirectly from radio measurements by *Voyager 2* (Pedersen *et al.*, 1991). The impact velocities of these particles can be increased by the gravity of a host planet, and so even a small number of IDP impacts can be a potent source of weathering on the surface of an icy satellite.

Triton's young surface age is partially due to its origin. Triton is on a retrograde orbit inclined 156° to Neptune's rotational axis. This orbit strongly implies that Triton was not formed from the same circumplanetary disk that produced the small regular satellites of Neptune, which are prograde and aligned to Neptune's equator. Rather, Triton was almost certainly captured by Neptune after regular satellite had finished. This likely occurred during Neptune's migration process, when it encountered many objects in the massive proto-Kuiper Belt. Several methods have been proposed for the capture, but the simplest is that Triton was originally a binary system, and when it flew past Neptune, one member of the binary was captured and the other ejected (Agnor and Hamilton, 2006).

Dynamical captures tend to produce eccentric orbits, as it only takes a slight change in velocity at closest approach to a planet to transform a hyperbolic approach orbit to a very eccentric one. However, Triton's orbit is circular to the accuracy of the observations (Jacobson *et al.*, 1991). Triton therefore possibly went through a process of extreme tidal evolution after its capture to leave it in its current orbit.

This capture and evolution process is especially intriguing, as the observations of the *Kepler* space telescope have shown that highly migrated giant planets are common (Lissauer *et al.*, 2011). Some of these migrated giant exoplanets may have captured satellites even larger than Triton through the same process.

The structure of this dissertation is four separate but related studies into these processes. We start with two ongoing processes in the outer solar system, dust impacts from interplanetary dust particles and secondary dust in the Pluto system. The impacts of IDPs on icy surfaces could help to explain why the water ice these surfaces looks so much more crystalline than would be expected. In addition, IDPs can throw off secondary dust from the small satellites of Pluto, which is then swept up by Pluto and Charon. We then explore orbital perturbations that happened closer to the solar system. Staying with the outer edges of our solar system, we analyzed the effect of solar gravitational perturbations of the orbits of binary minor planets beyond Neptune. We wrap up by applying this perturbation model to large, Earth-like captured satellites of exosolar giant planets. The chapters thus progress from the giant planets to Pluto to the classical Kuiper Belt to finally other star systems.

In Chapter 2, we show that dust impacts onto the surfaces of giant planet icy satellite and Kuiper Belt Objects (KBOs) can crystallize ice on their surfaces. The spectra of water ice on the surfaces of these objects indicate that their surface ice is in a crystalline state. This conflicts with theoretical models, which predict that radiation (Galactic cosmic rays and solar ultraviolet) should damage the crystalline structure of ice on geologically short timescales. Temperatures are too low in the outer solar system for the ice to anneal, and reflectance spectra of these bodies should match those of amorphous solid water (ASW). We assess whether the kinetic energy deposited as heat by micrometeorite impacts on outer solar system bodies is sufficient to anneal their surface ice down to a near infrared optical depth (350 μm). We cal-

culate the kinetic energy flux from interplanetary micrometeorite impacts, including gravitational focusing. We also calculate the thermal diffusion of impact heat in various surfaces and the rate of annealing of ice. We conclude that the rate of annealing from micrometeorite impacts is sufficient to explain the crystallinity of ice on nearly all the surfaces of the saturnian, uranian and neptunian satellites. We discuss how the model can be used in conjunction with spectra of KBOs to probe dust fluxes in the Kuiper Belt. This work was published as Porter *et al.* (2010).

In Chapter 3, we examine the role of intra-system dust in the Pluto system. The small satellites of Pluto have sufficiently low surface gravity that micrometeorite impacts can easily produce ejecta that escapes from their surfaces. This ejecta can either escape from the Pluto system or be swept up by Pluto or its satellites. We show through n-body integrations that Charon primarily sweeps up lower velocity ejecta, while Pluto is impacted by dust that is ejected at higher velocities. The dust also impacts Pluto in different locations depending on its ejection velocity. We show that the albedo features of Pluto and Charon correspond well to the expected distribution of impacts from higher velocity small satellite ejecta.

In Chapter 4, we show that the orbits of trans-neptunian binary systems can be transformed by solar perturbations. Recent observational surveys of TNBs have dramatically increased the number of known mutual orbits. Our Kozai Cycle Tidal Friction (KCTF) simulations of synthetic trans-neptunian binaries show that tidal dissipation in these systems can completely reshape their original orbits. Specifically, solar torques should have dramatically accelerated the semimajor axis decay and circularization timescales of primordial (or recently excited) TNBs. As a result, our initially random distribution of TNBs in our simulations evolved to have a large population of tight circular orbits. This tight circular population appears for a range of TNO physical properties, though a strong gravitational quadrupole can prevent

some from fully circularizing. We introduce a stability parameter to predict the effectiveness of KCTF on a TNB orbit, and show that a number of known TNBs must have a large gravitational quadrupole to be stable. This work was published as Porter and Grundy (2012).

In Chapter 5, we model the orbital evolution of an Earth-like planet captured as the satellite of an exosolar giant planet. The satellites of extrasolar planets (exomoons) have been recently proposed as astrobiological targets. Since giant planets in the habitable zone are thought to have migrated there, it is possible that they may have captured a former terrestrial planet or planetesimal. We therefore attempt to model the dynamical evolution of a terrestrial planet captured into orbit around a giant planet in the habitable zone of a star. We find that approximately half of loose elliptical orbits result in stable circular orbits over timescales of less than a few million years. We also find that those orbits are mostly low-inclination, but have no prograde/retrograde preference. In addition, we calculate the transit timing and duration variations for the resulting systems, and find that potentially habitable Earth-mass exomoons should be detectable. This work was published as Porter and Grundy (2011).

Finally in Chapter 6, we discuss the commonality of this work and how the four projects relate to each other. In addition, we discuss future work that could be done to advance these projects further.

Chapter 2

MICROMETEORITE IMPACT ANNEALING OF ICE IN THE OUTER SOLAR SYSTEM

2.1 Introduction

Effectively airless icy objects in the outer solar system — satellites, comets, and Kuiper Belt Objects (KBOs) — play host to one of the most common but least understood solid surfaces in the solar system. While spacecraft have observed their large-scale morphologies, which often are dominated by impact craters and tectonic features, the nature of their surfaces remain difficult to observe at small scales. Reflectance spectra represent the most reliable way of probing the composition of their surfaces. The dominant features in the reflectance spectra of outer solar system bodies are the vibrational modes of water ice, in the infrared. More detailed modeling often reveals that their surfaces are porous regoliths of mainly water ice, mixed with various organics, and a spectrally neutral phase, possibly hydrated silicates (Roush, 2001).

At low pressures below 150 K, water ice can exist in either a crystalline state (either hexagonal Ih or cubic Ic ice) or as amorphous ice (amorphous solid water; ASW) (Jenniskens and Blake, 1996). These can be spectrally distinguished by an absorption feature at 1.65 μm, which is strong in both Ic and Ih (especially at low temperatures: Mastrapa and Brown (2006)), but is much weaker in ASW. Spectra returned by the Visual and Infrared Mapping Spectrometer (VIMS) on the NASA/ESA *Cassini* spacecraft appear to show that crystalline water is present on the surfaces of nearly all the airless satellites of Saturn (Filacchione *et al.*, 2007). In addition, ground-

based spectra of both the regular satellites of Uranus (Bauer *et al.*, 2002; Grundy *et al.*, 2006) and several Kuiper Belt Objects (KBOs) also appear to show the 1.65 μm feature (Barkume *et al.*, 2008; Cook *et al.*, 2007; Jewitt and Luu, 2004). Nearly every large ($>$ 200 km) outer solar system body with water ice has shown evidence of crystalline water ice.

The prevalence of crystalline water ice surfaces beyond Jupiter's orbit is unexpected (Jenniskens and Blake, 1996). Below approximately 150 K, water vapor will deposit onto a surface as ASW, and can only be annealed to crystalline ice through the application of external heat (Jenniskens and Blake, 1996). More important, the crystalline structure of ice can be damaged by radiation; laboratory tests have shown that both solar ultraviolet (UV) radiation (Leto and Baratta, 2003) and Galactic cosmic rays (Mastrapa and Brown, 2006) can convert crystalline ice into ASW. The timescales for this amorphization are on the order of 1500 kyr for Galactic cosmic rays (GCRs) throughout the outer solar system, and 50 kyr for UV amorphization at 40 AU (assuming that all solar UV photons shortward of 200 nm are as capable, per photon energy, at amorphizing ice as Lyα photons), decreasing with greater distance from the Sun (Cook *et al.*, 2007). Some widespread annealing process must therefore be effectively competing with GCRs and solar UV in order for the 1.65 μm spectral feature to be so common.

Cook *et al.* (2007) reviewed several annealing mechanisms in the context of Charon, all of which are applicable to icy objects in general. A solid-state greenhouse effect, utilizing ice's transparency in the visual and opacity in the infrared, was shown to be ineffective at raising the temperature of surface ice more than a few Kelvin on that body. Likewise, solid-state convection cannot work effectively to expose subsurface crystalline ice for surface temperatures below 140 K (at which point ASW would self-anneal), because the viscosity is too high. Cook *et al.* (2007) therefore favored

for Charon the mechanism of cryovolcanism, in which subsurface liquid water erupts on the surface, freezing on the surface at above 150 K, and preserving its crystalline structure as it cools to the ambient temperature. Radar mapping by *Cassini* appears to show several surface morphologies on Titan that could indicate cryovolcanic flows (Lopes *et al.*, 2007). In addition, imaging by NASA's *Voyager 2* spacecraft appeared to show cryovolcanic flow features on both Ariel (Smith *et al.*, 1986) and Triton (Smith *et al.*, 1989). Desch *et al.* (2009) have recently shown through thermal interior modeling that cryovolcanism may be presently acting on many KBOs or icy satellites at least 600 km in radius and contain ammonia. However, many icy satellites with crystalline ice features are simply too small to sustain cryovolcanism, and an alternative annealing mechanism is still sought.

One final method reviewed by Cook *et al.* (2007) was micrometeorite impact annealing. In this process, interplanetary dust particles (IDPs) impact the surface ice and deposit their kinetic energy as heat. This heat then diffuses into the surrounding ice, briefly raising its temperature high enough to cause the ice to crystallize (into either Ic or Ih). Cook et al. (2007) did not favor this mechanism for KBOs or Charon, because the dust fluxes were thought to be too low (we revisit this point below). However, because IDPs are gravitationally focused in the gravity wells of large planets (Krivov *et al.*, 2003), the IDP kinetic energy fluxes at the orbits of the saturnian and uranian regular satellites can be much enhanced over the values previously inferred by Cook et al. (2007) for KBOs.

This paper re-examines the role of micrometeorite annealing on the crystallinity of ice on outer solar system icy bodies. First, the impact annealing process will be described and quantified. Next, it will be applied to the icy satellites of Saturn, Uranus, and Neptune. Finally, micrometeorite annealing on KBOs will estimated, and

methods of using micrometeorite annealing as a probe of Kuiper Belt dust production will be discussed.

2.2 Modeling Micrometeorite Annealing

In order to quantify the rate at which kinetic energy deposited by micrometeorite impacts could anneal ice on a surface, we first simulated the effects of a single impact. Cook *et al.* (2007) laid the groundwork for this model by estimating the mass of surface ice raised to greater than 185 K (even if only for a fraction of a second) during a given impact event. Under conditions appropriate for Charon, they found that ice approximately ten times the mass of the impactor is annealed. However, the micrometeorites impacting the moons of Saturn and Uranus are considerably faster and of higher number density than in the Kuiper Belt, due chiefly to planetary gravity (see below). We therefore decided to attempt a more rigorous simulation of the annealing of these moons' surface ice.

2.2.1 Theoretical Model

For the model, we assumed the micrometeorites implant themselves deeply (many particle diameters) in the icy regolith, and deposit a fraction ξ of their kinetic energy as heat where they are stopped. Typically $\xi = 2/3$, the rest being converted into mechanical work (Hartmann, 1985). This heat then diffuses spherically outward through the ice, assumed to be ASW. It is assumed in the calculations that the micrometeorites stop at depths at least 30 times their own radius, justifying spherical symmetry. Laboratory tests of hypervelocity impacts into silicate regoliths actually indicate that impactors generally do not penetrate that deep (Hartmann, 1985), so that some fraction of heat energy necessarily is lost at the surface and does not anneal ice, effectively lowering ξ.

While most of the mid-size moons of Saturn have a nearly pure ice surface (Grundy *et al.*, 1999), the surfaces of the moons of Uranus as well as nearly every KBO have mixtures of organics and silicates with a lower thermal conductivity than ice (Barkume *et al.*, 2008; Grundy *et al.*, 2006), which will lead to a higher fraction of ice being annealed than this model estimates.

In the results described below, we sought to parameterize these limits to the amount of ASW that a single impact can convert to crystalline ice. For the thermal model, we therefore set $\xi = 1$, allowing a lower ξ to be used once the relationship between energy and mass annealed is known (see Equation 2.6).

Within the model, the ice to be annealed is broken into 300 spherical shells of equal thickness Δx. The simulation is initialized by depositing the kinetic energy of the impactor evenly in the 10 innermost zones. All other zones are initialized at the given surface temperature. To convert between temperature and energy, we assumed the following simplified Debye model for specific heat within shell i (bounded by radii x_{i-1} and x_i):

$$E_i(T) = \int_0^T M_i \, C_P(T') \, dT' \approx \rho \, A \, T^2, \tag{2.1}$$

where M_i is the mass within shell i, equal to its volume times the material density ρ: $M_i = (4\pi/3) \left(x_i^3 - x_{i-1}^3\right) \rho$. For the innermost 10 zones corresponding to the impactor, we have assumed parameters appropriate for a silicate IDP (Messenger *et al.*, 2003), $A = 1.4\,\mathrm{J\,kg^{-1}\,K^{-2}}$ [corresponding to a heat capacity of $280\,(T/100\,\mathrm{K})\,\mathrm{J\,kg^{-1}\,K^{-1}}$], and $\rho = 2500\,\mathrm{kg\,m^{-3}}$. For the surrounding ice, we have assumed $A = 3.87\,\mathrm{J\,kg^{-1}\,K^{-2}}$ [corresponding to a heat capacity of $773\,(T/100\,\mathrm{K})\,\mathrm{J\,kg^{-1}\,K^{-1}}$], and $\rho = 500\,\mathrm{kg\,m^{-3}}$, which implies a regolith porosity of 0.5 (Grundy *et al.*, 1999). We then calculated the spherically symmetric heat flux (evaluated at the boundaries of zones) to be

$$F_i = -k \left.\frac{\partial T}{\partial r}\right|_{x_i} = -\frac{(k_i + k_{i+1})}{2} \cdot \frac{T_{i+1} - T_i}{(x_{i+1} - x_{i-1})/2}, \tag{2.2}$$

where F_i is the flux from zone i to $i+1$, and the resulting change in internal energy in zone i over a timestep Δt to be

$$\Delta E_i = \left(4\pi x_{i-1}^2 F_{i-1} - 4\pi x_i^2 F_i\right) \Delta t, \tag{2.3}$$

where k_i, and T_i are the thermal conductivity and temperature within shell i, evaluated at its center. We approximated the conductivity of the regolith to be that of crystalline ice (Klinger, 1980), setting $\rho = 0.5$ to account for porosity:

$$k(T) = 567 \left(\frac{\rho}{1\,\mathrm{g\,cm^{-3}}}\right) \left(\frac{T}{K}\right)^{-1} \mathrm{W\,m^{-1}\,K^{-1}} \tag{2.4}$$

The thermal conductivity of crystalline ice is much higher than ASW (Andersson and Suga, 2002), and thus a provides a lower limit on the mass annealed. Once the new thermal energies of all shells are calculated, Equation 2.1 is then inverted to find the new temperatures within the shells at each timestep.

The temperature within a shell, and the length of time it spends at each temperature, are used to assess whether the ice in the shell is annealed. Based on the data in Baragiola (2003), we assumed that the time it takes to fully anneal a sample of amorphous solid water is

$$t_{\mathrm{anneal}} \approx 8 \times 10^{16} \exp\left(-\frac{0.225\,\mathrm{T}}{K}\right) \mathrm{s} \tag{2.5}$$

During each timestep of length Δt (10^{-6} s), we assume a fraction $\Delta t / t_{\mathrm{anneal}} << 1$ of the ice is annealed.

2.2.2 Implementation and Results

We implemented the model above using a computer program in the C++ language with inputs of surface ice temperature T_{surf}, impactor diameter D_{p}, and impactor velocity V_{imp}, and outputs of mass annealed M_{anneal} and effective diffusion time. We

then ran this program across a parameter space ranging from $T_{\rm surf} = 40 - 100\,{\rm K}$, $D_{\rm p} = 10 - 150\,\mu{\rm m}$, and $V_{\rm imp} = 1 - 25\,{\rm km\,s^{-1}}$, at increments of $10\,{\rm K}$, $10\,\mu{\rm m}$, and $1\,{\rm km\,s^{-1}}$. Because the computing time needed to conduct a single impact simulation is long, we decided to seek an emperical relationship between the inputs and the mass of ice annealed per impact. We plotted the total mass annealed per impact versus the impactor's kinetic energy, and results can be seen in Figure 2.1. Because the diffusion times were so fast (less than a minute in all but highest energy cases), the mass annealed was mostly insensitive to the surface ice temperature. In addition, only the inner few shells were generally vaporized, and quickly recondensed, thus confirming the calculation of Cook *et al.* (2007). There did appear to be a strong power-law correspondence between the mass annealed and the impact energy. Using a simple regression fit, we found this relationship to be

$$M_{\rm anneal} \approx 3.9 \times 10^{-7} \left(\xi \, \frac{KE}{1\,{\rm J}} \right)^{1.33} {\rm kg} \tag{2.6}$$

Where KE is the impactor's kinetic energy, and ξ is the efficiency factor in converting KE into thermal energy capable of annealing ice, $\approx 2/3$ (Hartmann, 1985). Equation 2.6 also shows that the mass annealed, and thus the annealing rate, is directly proportional to $\xi^{1.33}$. The scatter in the plot is mainly due to there being a larger amount of data points with a moderate kinetic energy (e.g. large and slow or small and fast IDP) than the upper and lower ends of the energy range.

In order to estimate the effect of a rockier regolith, we ran a modified version of the above model with a 50% rock, 50% ice composition, with the thermal conductivities blended in the same way as in Desch *et al.* (2009). The result was that slightly more than half the mass of ice was annealed for a given input energy and regolith volume, resulting in relative crystalline fractions 10-20% higher than for pure ice. The fraction of ice annealed is mostly a function of the time the ice spends above the annealing

point, rather than the peak temperature. Thus, the slower thermal conductivity of the rock in the regolith allows for longer diffusion times, and thus slightly more annealing. Amorphous ice also has a lower thermal conductivity than crystalline ice, and versions of the code that accounted for this showed a similar effect. We thus considered the canonical case (all crystalline conductivity) to be a lower limit to ice annealed per impact.

Finally, we constructed a third model to represent the case where the micrometeorite distributes its energy equally along a linear path down to 350 μm, the optical depth of ice for 1.6 μm near infrared (NIR). Since there is no energy difference along the path, and thus no vertical thermal diffusion, this can be modeled as a one-dimensional cylindrical geometry, with heat diffusing perpendicular to the path. Since the major bottleneck to annealing in the spherical case was in transporting the heat initially out of the micrometeorite, the larger initial heated volume of the linear case promised a higher annealed mass. This did indeed turn out to be the case for most impact energies, with the linear pure ice model annealing up to a factor of ten more ice than the spherical pure ice model (Eq. 2.6). On the other hand, micrometeorites at the smaller / slower end of the considered range tended to dump their energy into the ice too fast, annealing as little as a quarter of the ice annealed in the spherical case. Since the actual diffusion geometry in real impacts would be somewhere in between these two end members, we considered the model fit to the spherical case to be a realistic conservative estimate.

2.3 Annealing on Icy Satellites

Observing the surfaces of airless icy satellites is on the one hand eased by the lack of any substantial interference other than telluric, but is also complicated by their small angular size. Grundy *et al.* (1999) provide a very comprehensive collection

of near-infrared ground-based spectra for large icy satellites. Europa and Ganymede both show noticeable 1.65 μm features, while the rockiness of Callisto mostly obscures the vibrational modes of water. Likewise, Iapetus, Rhea, Dione, Tethys, Enceladus, and the A and B rings all show deep absorption features at 1.65 μm. This has been confirmed by measurements from *Cassini* (Filacchione *et al.*, 2007), and crystallinity maps are available for Enceladus (Newman *et al.*, 2008). Ground-based spectra also show crystalline ice on all of the five regular satellites of Uranus, though the signal-to-noise for Umbriel is low due to the small amount of exposed ice on its surface (Bauer *et al.*, 2002; Grundy *et al.*, 1999, 2006).

2.3.1 Dust Sources

Micrometeorites that impact icy satellites can have two sources: interplanetary dust swept up by the planet's gravity; and dust particles native to the planetary system. Dust in orbit around the planet naturally imparts less kinetic energy onto satellites, due to its lower velocity relative to the satellites; it is therefore only competitive with IDPs at very high densities, such as in a planetary ring. The only dense ring known to hold large satellites is the E-ring of Saturn. Measurements of dust flux by the *Cassini* spacecraft appear to show that Enceladus is the source of the E-ring dust (Spahn *et al.*, 2006). As can be seen in Figure 2.2, only at Enceladus is the E-ring dense enough to have a kinetic energy flux comparable to (though lower than) IDPs at the same radius. The primary dust source for micrometeorite annealing on icy satellites is therefore interplanetary dust particles.

Dust densities are difficult to measure obsevationally, and so spacecraft mission offer the best dust data for the outer solar system. The first in-situ measurements of IDPs beyond the orbit of Jupiter were made by NASA's *Pioneer 10* and *11* spacecraft in the 1970s (Humes, 1980). Though the *Pioneer 11* detector was saturated during

its close encounter with Saturn, the *Pioneer 10* detector reported the interplanetary dust flux out to 18 AU. It found that the spatial density of particles $\geq 10^{-12}$ kg was nearly constant from Jupiter out to 18 AU, implying that Uranus encounters a similar flux as Saturn. Divine (1993) modeled this data and Krivov *et al.* (2003) adapted it to find a dust flux of $1.8 \times 10^{-16}\,\mathrm{kg\,m^{-2}\,s^{-1}}$ at Saturn; applying their modeling we expect a flux at Uranus of $1.2 \times 10^{-16}\,\mathrm{kg\,m^{-2}\,s^{-1}}$. Further modeling by Liou and Zook (1999) has revealed the two-dimensional structure of Kuiper Belt dust, and implies that the dust spatial density is similar at Neptune to Uranus (see their Figure 7). Scaling for orbital velocity, we can then assume the IDP flux at Neptune to be approximately $1.0 \times 10^{-16}\,\mathrm{kg\,m^{-2}\,s^{-1}}$. Experimental confirmation of these fluxes is being collected now by the Student Dust Counter on NASA's *New Horizons* spacecraft, which passed the orbit of Saturn in June 2008 and will reach Pluto in July 2015 (Horányi *et al.*, 2008). The Student Dust Counter has a sensitivity down to 10^{-15} kg, and so could detect whole populations of IDPs missed by *Pioneer 10*.

2.3.2 Gravitational Focusing

To find the amount of ice that could be annealed by IDPs, we need to find the kinetic energy they deposit on the satellites' surfaces. As an IDP enters a planet's Hill radius, it is accelerated towards the planet. Thus, both the velocity and the number of IDPs increases dramatically close to the planet. Colombo *et al.* (1966) found (using energy conservation arguments) the velocity scaling as a dust particle approaches a planet to be the sum in quadrature of the IDP's heliocentric velocity and the planetocentric escape velocity:

$$\frac{v_{\mathrm{imp}}}{v_{\mathrm{imp}}^{\infty}} = \sqrt{1 + \frac{2GM_{\mathrm{p}}}{r(v_{\mathrm{imp}}^{\infty})^2}}, \tag{2.7}$$

where $M_{\rm p}$ is the planet's mass, r the distance from the planet, and v_{imp}^{∞} is the dust's distant velocity relative to the planet, assumed here to be the planet's orbital velocity times $\sqrt{e^2+i^2}$, where $e \approx i \approx 0.3$. Spahn *et al.* (2006) corrected Colombo *et al.* (1966) to find the number density scaling to be

$$\frac{n_{\rm imp}}{n_{\rm imp}^{\infty}} = \frac{1}{2}\frac{v_{\rm imp}}{v_{\rm imp}^{\infty}} + \frac{1}{2}\left[\left(\frac{v_{\rm imp}}{v_{\rm imp}^{\infty}}\right)^2 - \left(\frac{R_{\rm p}}{r}\right)^2\left(1+\frac{2GM_{\rm p}}{R_{\rm p}(v_{\rm imp}^{\infty})^2}\right)\right]^{1/2}. \tag{2.8}$$

The velocity with which an IDP impacts a satellite is a combination of both its velocity relative to the planet, as well as the satellite's planetocentric velocity, $V_{\rm sat}$. If we assume that a median impact is perpendicular to the satellite's orbit, we can find the average kinetic energy on impact, $KE_{\rm imp} = (1/2)m_{\rm imp}V_{\rm net}^2$, where the impact velocity is

$$V_{\rm net} = \sqrt{V_{\rm sat}^2 + \left(\frac{V_{\rm imp}}{V_{\rm imp}^{\infty}}V_{\rm imp}^{\infty}\right)^2}. \tag{2.9}$$

To account for the eccentricity of satellites' orbits, the kinetic energy flux was numerically integrated and averaged over a full orbit. Since nearly all these satellites have circular orbits, this was generally a negligible effect, although the annealing rate on the highly eccentric satellite Nereid was doubled compared to the case where its orbit had zero eccentricity. Knowing the average kinetic energy imparted per impact, Equation 2.6 was used to find the mean mass of ice annealed per micrometeorite impact, $\bar{m}_{\rm anneal}$.

The annealing rate was then found by multiplying the mass annealed per impact by the number of impacts with this energy. This is related to the flux of kinetic energy onto the satellites,

$$KE_{\rm flux} = \left(\frac{F_{\rm imp}^{\infty}}{v_{\rm imp}^{\infty}}\right)\left(\frac{n_{\rm imp}}{n_{\rm imp}^{\infty}}\right)\frac{V_{\rm net}^3}{2} \tag{2.10}$$

where $F_{\rm imp}^{\infty}$ is the distant mass flux of IDPs in $\mathrm{kg\,m^{-2}\,s^{-1}}$. The rate at which ice is annealed on the surface of a satellite (mass per area per time) is then straightforwardly

found to be $(KE_{\rm flux}/KE_{\rm imp})\,\bar{m}_{\rm anneal}$, and the timescale to anneal all but $1/e$ of the ice down to a depth $d_{\rm ice}$ is

$$\tau_{\rm anneal} \approx 0.63\ d_{\rm ice}\rho_{\rm ice}\,\frac{KE_{\rm imp}}{KE_{\rm flux}\,\bar{m}_{\rm anneal}}. \tag{2.11}$$

2.3.3 Ice Amorphization

The most effective process micrometeorite annealing has to compete with is the conversion of crystalline water ice into amorphous solid water by either ultraviolet or GCR ion irradiation. Leto and Baratta (2003) have shown that low-temperature (16 K) ice exposed to Lyman α radiation will have its spectral signature transformed from crystalline (strong 1.65 μm feature) to amorphous (weak 1.65 μm feature) with a dosage of $\approx$ 10 eV/molecule. Likewise, Mastrapa and Brown (2006) have shown that a similar dose of protons is sufficient to amorphize ice at 40 K, but starts to become ineffective above 50 K. Since the H_2O ice temperatures reported by Grundy *et al.* (1999) for the Saturnian and Uranian systems are all above 70K, the efficiency of radiation amorphization per eV of dose should be considerably lower for icy satellites than in the colder Kuiper Belt. On the other hand, while the GCR dose is smaller closer to the Sun (deeper into the solar magnetosphere), the UV flux is much larger, as it scales with total solar flux. We therefore used a constant amorphization timescale of 1500 kyr for Galactic cosmic rays (GCRs) throughout the outer solar system. Solar wind particle radiation was not considered, as it is sufficiently weak in the outer solar system that GCRs dominate the radiation dose. We also did not consider the effects of sputtering from either GCRs or the IDPs themselves, as the yields are very low compared to the expected annealing and amorphization rates. In addition, sputtered H_2O would probably recondense in the regolith (Hapke, 1986) with sufficient thermal energy to form crystalline ice.

Cook *et al.* (2007) estimated that the UV amorphization timescale to be ≈40 kyr to anneal the fraction ($1 - e^{-1} \approx 63\%$) of crystalline ice down to 0.35 mm, the $1/e$ optical depth of ice at 1.65 μm. Considering the constraints above, we estimate the lower limit to the UV amorphization time $\tau_{\rm amor}$ to be 150 kyr, 100 kyr, and 50 kyr, for the saturnian, uranian, and neptunian systems, respectively. Since both τ_{amor} and τ_{anneal} are timescales to modify ≈ 63% of the ice, their relative proportion gives the fraction of ice currently in steady state crystalline form on an icy satellite's surface:

$$\%_{\rm Crystalline} = \frac{\tau_{amor}}{\tau_{anneal} + \tau_{amor}} \cdot 100\% \tag{2.12}$$

It should also be noted that Mastrapa *et al.* (2008) have shown that only a 20% fraction of crystalline ice is sufficient to make a sample's spectra look nearly fully crystalline. Therefore, a crystalline fraction greater than 20% should be considered sufficient to explain most observed crystalline features.

2.3.4 Icy Satellite Results

Table 2.1 lists the results of the above analysis for several icy satellites. In general, micrometeorite impact heating was found to be effective in annealing amorphous solid water into crystalline ice in fractions that can explain observed icy satellite spectra. Specifically, the number density and velocity scaling from gravitational focusing greatly increased the effectiveness of micrometeorites, by up to three orders of magnitude. In addition, the increased dust densities closer to the Sun allowed for generally higher crystalline fractions at Saturn relative to Neptune. This, though, appears to be a second-order effect when compared to gravitational focusing from the planets.

The three icy satellites of Jupiter have surface temperatures that could self-anneal amorphous ice (Grundy *et al.*, 1999), but also inhabit the very high radiation environment of the jovian magnetosphere. Determining the effect, therefore, of micromete-

orite impacts on surface crystallinity is difficult; for a full treatment, see Hansen and McCord (2004). Nonetheless, we calculate that the micrometeorite annealing times for Europa, Ganymede, and Callisto to be 2.3 kyr, 6.7 kyr, and 24 kyr, respectively.

The saturnian system boasts a great variety of icy satellites, and their wide range of orbits shows the effectiveness of gravitational focusing. While close-in Mimas is annealed very rapidly (4.4 kyr), distant Phoebe is only annealed in 14 Myr. Enceladus's active endogenic processes (Waite *et al.*, 2006) may mask any effect of IDP micrometeorites, especially in the southern hemisphere. However, on the apparently more geologically quiescent Mimas, Tethys, Dione, Rhea, and Iapetus, micrometeorite annealing may be the dominant active process controlling the observed ice spectra. Hyperion and Phoebe are both irregular, low density objects whose pockmarked surfaces may act as blackbody cavities to mask their thermal infrared spectral structure (Cooper *et al.*, 2002). However, their surface ice could still be noticeably affected by micrometeorite impact heating. Titan was obviously not considered due to its dense atmosphere.

Uranus has five regular satellites orbiting around its askew rotational axis. Though this means that the effective day/night cycle on these moons is 84 years, this is sufficiently lower than the predicted annealing and amorphization timescales as to not be a concern. The regular spacing of their orbits also shows very well the drop-off of gravitational focusing with distance from the host planet. The uranian satellites have considerably more non-icy material on their surfaces than the similar-sized moons of Saturn, but still show strong crystalline ice spectral signatures. This corresponds well with the predicted annealing timescales, which range from 121 kyr for Mimas, to 2.4 Myr for Oberon.

The satellite system of Neptune is less regular, but could offer a better test of micrometeorite annealing. The close-in proximity of Proteus to the planet allows for

a comparable annealing rate to Rhea. Triton is probably a captured dwarf planet from the Kuiper Belt (Agnor and Hamilton, 2006), and the active geysers and surface features observed on it by the NASA *Voyager 2* probe may mask any IDP annealing signature. Nereid is notable for its highly eccentric orbit (e=0.75) which nearly doubles its annealing rate, but not enough to effectively anneal its surface.

To see the upper bound of the annealing based on uncertainties in the *Pioneer 10* data, Table 2.1 lists the effectiveness of multiplying IDP fluxes by ten. This increases the number of satellites on which micrometeorite annealing is effective by one or two per planetary system. Likewise, assuming that UV amorphization is ineffective, and the Galactic Cosmic Ray (GCR) amorphization timescale is ≈ 1.5 Myr, allows all but the most distant satellites to be crystalline.

2.4 Discussion

In addition to the possible diffusion geometries discussed above, some uncertainty in these estimates comes from the estimate of ξ. This estimate is based on relatively low velocity (<5 km/s) laboratory tests onto silicate (versus icy) powders. Additional experimentation would help to constrain this value for high velocity impacts onto cryogenic ices. Also, better constraints on the interplanetary dust flux beyond Jupiter would be very beneficial to estimating annealing rates. The Student Dust Counter on the *New Horizons* spacecraft will help considerably with this, as will *New Horizon*'s direct observations of Pluto and Charon.

The nature of these calculations also allowed for an estimate of the total mass of IDP material that would accumulate on the surfaces of these satellites. Multiplying the gravitationally-focused mass flux by 4.0 Gyr produced a mass density ranging from 300 kg/m^2 (for Mimas) to 30 kg/m^2 (for Phoebe). If all these particles had a mean density of 2500 kg/m^3 (as assumed above), and were stacked with a 50%

porosity, they would be 240 mm and 24 mm deep, respectively. While this is deeper than our assumed penetration depths for IDPs, they are reasonable depths to be fully mixed into the regolith by impact gardening in 4.0 Gyr. In addition, if the IDP are sourced mainly from comets and KBO, they could be mostly water ice themselves.

Observationally testing the effectiveness of micrometeorite annealing from Earth requires a well-constrained comparison. The irregular satellites of Neptune could be used, as they all recieve the same solar and galactic illumination, are small enough that endogenic processes would not affect their spectra, but experience a broad range of gravitationally-focused dust velocities. Proteus and Nereid have very different predicted annealing rates, and thus could represent opposite endmembers of micrometeorite annealing effectiveness. The spectra of Nereid obsevered by Brown *et al.* (1999) show water ice, but not at sufficient resolution to measure crystallinity. Likewise, HST NICMOS photometry of Proteus did not cover the 1.65 μm feature (Dumas *et al.*, 2003). Future near IR obsevations of theses two satellites are thus required to use them as tests of micrometoerite annealing.

Micrometeorite annealing appears to be effective for most icy satellites, raising the question of how much effect this process may have on Kuiper Belt Objects (KBOs). Since the lower temperatures of the Kuiper Belt allow for faster radiation amorphization times, and considering the lack of a giant planet to gravitationally focus IDPs, the immediate answer would seem to be that annealing should be minimal on these objects. However, the Kuiper Belt is potentially the dustiest part of the solar system (Liou and Zook, 1999). Since no in-situ dust data is available yet for beyond the orbit of Uranus, current models for Kuiper Belt dust are based on dust measurements farther in, and inferences about the rate of inward migration. These models tend to show a peak in dust density at around 40-45 AU. If this true, then KBOs passing through this region could be effectively annealed by micrometeorites.

To quantify this effect, Table 2.2 lists the IDP fluxes required to anneal a variety of Kuiper Belt objects to 20% crystalline. The UV and GCR amorphization timescales used are the same as previously calculated by Cook *et al.* (2007) for Charon (40 kyr and 1.5 Myr, respectively). The range of these two timescales thus provides a upper and lower limit to the minimum required dust flux for annealing to be effective. Since the regression fit used in Equation 2.6 is more appropriate for higher thermal and kinetic energies, the full thermal diffusion model was applied to each case. The calculations were made by integrating each object across its orbit to find the mean kinetic energy flux per a constant mass flux. Generally, the KBOs required an order magnitude less dust than Pioneer 10 observed at Uranus (1.0×10^{-16} kg $s^{-1}m^{-2}$) to compete with UV amorphization, and even less to compete with galactic cosmic rays.

Since not all of these objects appear to have large amounts of water ice on their surfaces, measuring the crystalline/amorphous ratio can difficult. Values that have been reported in the literature thus far include Orcus at 50% crystalline (Barucci *et al.*, 2008), Quaoar at 50% (Jewitt and Luu, 2004), Charon at 90% (Cook *et al.*, 2007), and Haumea (formerly 2003 EL_{61}) at 66-80% (Trujillo *et al.*, 2007) or 40-60% (Pinilla-Alonso *et al.*, 2009). Haumea is an interesting case; it has a highly irregular shape, a rapid rotation rate, and a surface that appears to be mostly water ice (Rabinowitz *et al.*, 2006; Lacerda *et al.*, 2008; Trujillo *et al.*, 2007). Impact annealing could be effective on its surface, explaining its crystallinity without need for surface cryovolcanism. Indeed, as Table 2.2 shows, micrometeorite annealing is potentially a very effective process for crystallizing surface ice across the Kuiper Belt.

In summary, micrometeorite annealing is effective for most icy satellites. The micrometeorite impact heating process was modeled diffusively for an icy regolith, allowing for the estimation of mass annealed per impact as a function of impact kinetic energy. In addition, the gravitational focusing of IDPs by giant planets can

considerably increase the micrometeorite kinetic energy flux onto the surfaces of their satellites. These can then be combined to calculate the amount of time to anneal the surface of an icy satellite. UV and ion irradiation work to reverse this process, but not effectively so for nearly all the saturnian and uranian satellites. This model has the potential to explain some of the crystalline ice present on Kuiper Belt Objects and could be expanded to use the crystalline fraction measured for KBOs as a probe of dust fluxes in the Kuiper Belt.

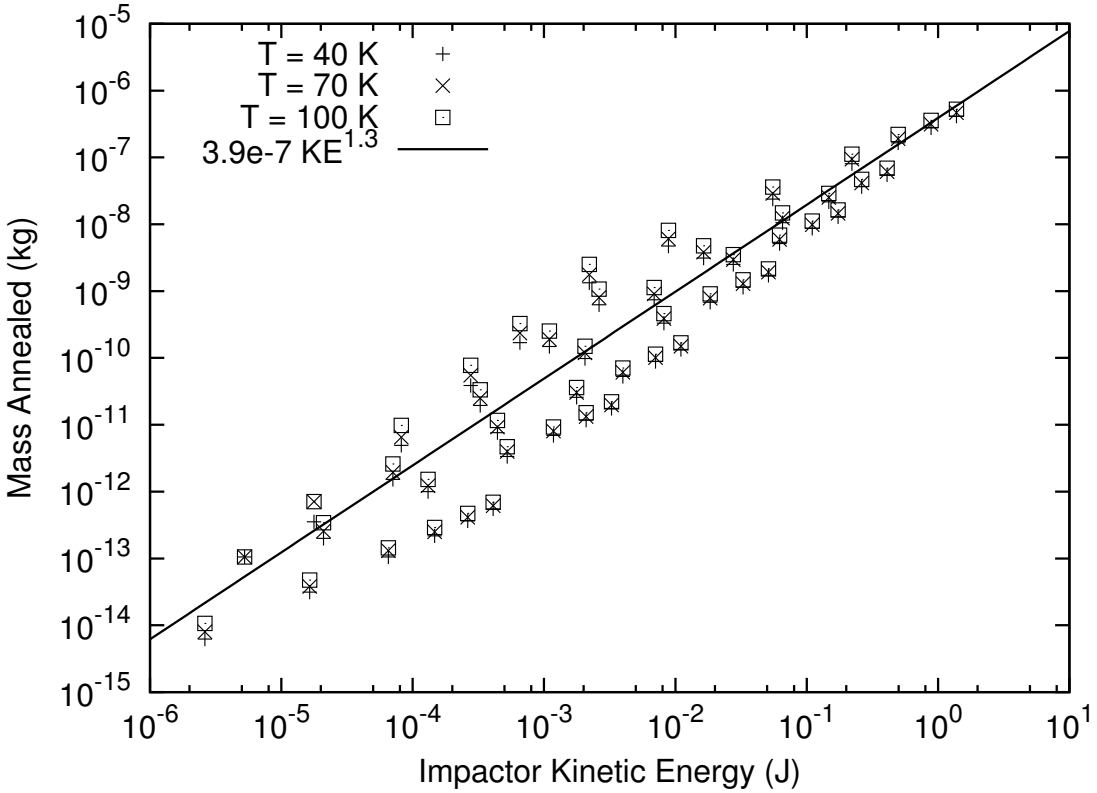

Figure 2.1: Mass of ice annealed as a function of impactor kinetic energy and surface temperature. The symbols are data points produced by the diffusion simulation, and the line is a regression fit.

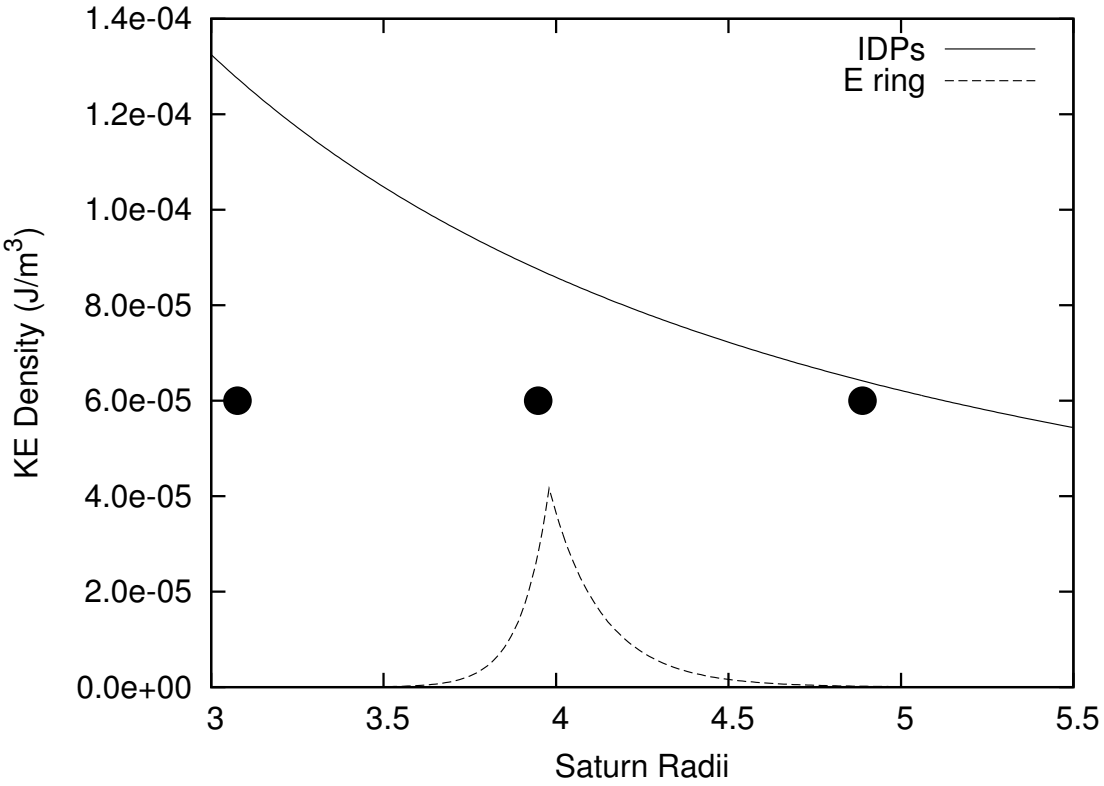

Figure 2.2: Sum of kinetic energy per unit volume around Saturn for IDP and E-Ring particles from the model of Spahn *et al.* (2006). The three circles represent the orbits of Mimas, Enceladus, and Tethys.

Object	$V_{\rm net}$ (km/s)	$n_{\rm imp}/n_{\rm imp}^{\infty}$	Annealing Time (kyr)	% Crystalline w/UV Amor.	Annealing effective with: UV	GCR	10x IDPs
Mimas	25.3	12.7	4.39	97.2	Yes	Yes	Yes
Enceladus	22.5	10.7	7.90	95.0	Yes	Yes	Yes
Tethys	20.5	9.21	12.9	92.1	Yes	Yes	Yes
Dione	18.3	7.69	22.9	86.8	Yes	Yes	Yes
Rhea	15.9	6.03	49.0	75.4	Yes	Yes	Yes
Hyperion	9.73	3.00	567	20.9	Yes	Yes	Yes
Iapetus	7.55	1.88	2290	6.16	No	Yes	Yes
Phoebe	5.15	1.26	13500	1.10	No	Maybe	No
Miranda	12.1	6.88	121	45.3	Yes	Yes	Yes
Ariel	10.5	5.24	264	27.5	Yes	Yes	Yes
Umbriel	9.10	4.19	557	15.2	Maybe	Yes	Yes
Titania	7.71	3.05	1390	6.72	No	Yes	Yes
Oberon	6.89	2.57	2460	3.91	No	Yes	Yes
Proteus	13.6	12.4	42.2	54.2	Yes	Yes	Yes
Triton	9.42	5.41	364	12.1	Maybe	Yes	Yes
Nereid	3.12	1.34	65200	0.0767	No	No	No

Table 2.1: Micrometeorite annealing results for the saturnian, uranian, and neptunian satellite systems. 'GCR' discounts all amorphization but by galactic cosmic rays, and '10x IDPs' scales the IDP flux by ten while assuming UV amorphization.

Object	Semimajor axis (AU)	$V_{\rm net}$ (km/s)	Needed $F_{\rm imp}^{\infty}$(kg s^{-1}m^{-2}): UV	GCR
Orcus	39.2	2.48	1.9e-17	5.1e-19
Charon	39.5	2.61	1.9e-17	5.0e-19
Pluto	39.5	3.25	1.6e-17	4.4e-19
Haumea	43.1	2.79	1.8e-17	4.9e-19
Quaoar	43.6	2.64	1.8e-17	4.9e-19
Makemake	45.8	2.69	1.9e-17	5.1e-19
Eris	67.7	2.85	1.8e-17	4.9e-19
Sedna	526	1.02	1.4e-16	3.6e-18

Table 2.2: Micrometeorite annealing results for selected Kuiper Belt objects. $F_{\rm imp}^{\infty}$ is the IDP mass flux required to produce an annealed fraction of 20%, and assumes an amorphization time of 40 kyr for UV and 1.5 Myr for GCR.

Chapter 3

EJECTA TRANSFER WITHIN THE PLUTO SYSTEM

3.1 Motivation

Pluto and its satellites form a uniquely complex dynamical system. Pluto and Charon are a true binary system with a mass ratio of 8.6 to 1 (Tholen *et al.*, 2008), and a center of mass about 1130 km (0.98 Pluto radii) above the surface of Pluto. Around them orbit several small satellites, Nix and Hydra (Weaver *et al.*, 2006), P/4 (Showalter *et al.*, 2011), and P/5 (Showalter *et al.*, 2012). The small satellites follow circular orbits centered on the Pluto-Charon center of mass and coplanar with the Pluto-Charon orbital plane. These orbits are stable, however only a slight change in eccentricity or inclination would lead to chaotic trajectories (Youdin *et al.*, 2012). It is therefore not trivial to predict the behavior of dust in the Pluto system.

Impacts onto Jupiter's innermost four satellites (from inner to outer, Metis, Adrastea, Amalthea, and Thebe) produce faint rings of short-lived dust particles (Burns *et al.*, 1999). This dust is typically ejecta from impacts of interplanetary dust particles (IDPs) onto the inner satellites, and has a mean grain size of 5 μm. Observations from the *Spitzer* space telescope have shown that Saturn hosts a similar (but much larger) impact generated ring, formed from material ejected from the retrograde irregular satellite Phoebe (Verbiscer *et al.*, 2009). The Phoebe ring extends inwards from Phoebe's orbit to the outermost regular satellite of Saturn, Iapetus. The ring material is swept up by Iapetus, accumulating over the age of the solar system approximately 20 cm of material, globally averaged (Verbiscer *et al.*, 2009). Importantly, though, the Phoebe ring impacts are not isotropic on the surface of Iapetus, but are instead

preferentially on the leading hemisphere. This accumulation of dark Phoebe material on the leading hemisphere and relatively clean water ice trailing hemisphere explains the wildly different albedo of the two hemispheres.

Thiessenhusen *et al.* (2002) suggested that Pluto and Charon are surrounded by a cloud of dust ejected from their surfaces, similar to Jupiter's impact-generated rings. This was difficult to show for dust from Pluto or Charon, though, as it would require a significant fraction of its impact velocity to escape from their surfaces. Stern *et al.* (2006) then suggested that impact ejecta dust from the newly discovered small satellites Nix and Hydra could produce temporary dust rings. The small satellites have much lower surface escape velocities, and so could potentially eject much more dust into the system. Steffl and Stern (2007) measured an upper limit for any dust in the system which they used to limit the dust particle lifetime to approximately 900 years. Poppe and Horányi (2011) and Pires dos Santos *et al.* (2013) both performed numerical simulations of dust particles ejected from Nix and Hydra, with Pires dos Santos *et al.* (2013) adding the additional complication of solar radiation pressure for dust grains of various sizes. They were able show that a significant fraction of ejected dust particles larger than 10 μm are able to orbit Pluto-Charon for timescales greater than 200 years, thus potentially providing a collision hazard to the *New Horizons* spacecraft when it flies through the system (Young *et al.*, 2008).

Poppe and Horányi (2011) and Pires dos Santos *et al.* (2013) also showed that the small satellite ejecta generally transfers inward, producing secondary impacts on Pluto and Charon. Here, we reproduce their simulations, but focusing on the impacts rather than the long-lived dust trajectories. In addition to estimating the fraction of small satellite ejecta which impacts Pluto and Charon, we also estimate the spatial distribution of those impacts on Pluto and Charon. Over time, the small satellites could have transfered a considerable amount of material to the surfaces of Pluto and

Charon. If the spatial distribution of the those impacts is sufficiently unique, it may produce observable features on those surfaces.

3.2 Simulations

We performed a large number of computational simulations of dust trajectories after being ejected from a small satellite. In these simulations, we randomizing the start time and the initial direction of the dust particle relative to the source satellite.

These simulations used a variable-timestep implicit 8th-order (with embedded 6th-order) Runge-Kutta-Nystrom integrator (Cash, 2005) to directly evolve the N-Body system consisting of Pluto, Charon, Nix, Hydra, and the dust particle. In addition to mutual gravitation between Pluto and its satellites, we also included solar gravitation and solar radiation pressure. For the radiation pressure, we assumed the dust particle was roughly spherical, and so the acceleration on the particle was:

$$\ddot{\vec{r}} = \frac{3}{8\pi} \frac{L_\odot Q_{pr}}{c\rho} \frac{\vec{r_\odot}}{r_\odot^3 D} \tag{3.1}$$

$$\ddot{\vec{r}} \approx 1.1 \times 10^{12} \frac{km^4}{day^2} \frac{\vec{r_\odot}}{r_\odot^3 D} \tag{3.2}$$

where $L_\odot$ is the solar luminosity, Q_{pr} is the radiation pressure efficiency (assumed to be unity), c is the speed of light in a vacuum, ρ is the density of the dust grain (assumed to be 1 g/cm^3), $\vec{r_\odot}$ is a vector from the Sun to the dust, and D is the diameter of the dust grain. Following after Pires dos Santos *et al.* (2013), we did not include Poynting-Robertson forces nor any non-spherical gravity fields, as both are very small for this case.

Since both gravity and radiation pressure are conservative forces, we were able to use a symplectic integrator, reducing both the numerical error and the execution time. Because the integrator is implicit, it performs several iterations per timestep, integrating the system forwards and backwards until the two converge. If they do

not converge, then the system is moving too fast for the given timestep, and a new, smaller timestep is attempted instead. Physically, this only occurs when the dust particle is close enough to one of the other objects that it accelerates rapidly, as it does right before an impact occurs.

We used the state vector and masses for Pluto, Charon, Nix, and Hydra from Tholen *et al.* (2008) as an initial condition, and evolved it forward a using the N-Body integrator for random amount of time, up to x days. We then chose a random unit vector for the dust ejection direction ($\vec{u}_{random}$), using the algorithm given in Knop (1970). The dust's initial position ($\vec{r}_{dust}$) and velocity ($\vec{v}_{dust}$) were then:

$$\vec{r}_{dust} = \vec{r}_{source} + ((R_{source} + 100m) \cdot \vec{u}_{random}) \tag{3.3}$$

$$\vec{v}_{dust} = \vec{v}_{source} + (v_{ejection} \cdot \vec{u}_{random}) \tag{3.4}$$

This starts the dust particle 100 meters above the surface of the source satellite (to prevent an immediate recollision), and travelling vertically up from the local surface (assuming the source is spherical). The ejection speed ($v_{ejection}$) and dust diameter are given values, and remain constant for each set of simulations.

Impacts, when the dust particle is within the nominal radius of another object, are checked for at the start of each timestep. If an impact is detected, the simulation is stopped and the final state output. All the impacts were detected within 10% of the nominal radius of the object, and most within 0.1%. Thus, the implicit integrator is sufficiently responsive to detect impacts at or near the surfaces. The simulations was also stopped if the dust exceeded a maximum distance from Pluto (1.2×10^7 km, approximately twice Pluto's Hill Radius), or if the dust exceeded the maximum allowed lifetime (10^6 days).

3.3 Results

Once a dust particle leaves the surface of its source satellite, it can have one of three different fates. If its velocity relative to its source is low enough, it will follow an orbit similar to the source, and reimpact after a few orbits. This happened for all our simulations with an ejection velocity smaller than 40 m/s. Alternatively, the dust particle can have enough velocity to escape from the Pluto system. This happened for all of our simulations with ejection velocities larger than 400 m/s, as well as most of the rest of the simulations. In addition to the dust particles that are initially ejected fast enough to escape, many slower particles also escaped after having a close encounter with either Pluto or Charon.

The third potential fate is for the dust particle to impact the surface of another body, chiefly Pluto or Charon. For a given ejection velocity and particle size, this only occurred in less than 20% of simulations, and typically much less. The probability of impact was mostly a function of ejection velocity. Charon impacts were primarily low-speed ejecta just fast enough to prevent reimpacting the source. Pluto-impacting dust, on the other hand, was typically ejected at slightly higher velocities. The impact velocities were just faster than the surface escape velocities of Pluto or Charon, and therefore nearly an order of magnitude faster than the ejection velocities from the small satellites.

3.3.1 Dust Trajectories

All the ejected dust particles follow orbits dominated by the Pluto-Charon barycenter. If the particle's ejection velocity is fast enough, it will leave the system on a hyperbolic trajectory. Since the small satellites are on almost-circular orbits relative to the barycenter, the minimum escape velocity is $\sqrt{2}$ times their orbital velocity.

This equates to a barycenter-relative velocity of about 200 m/s for Nix and 173 m/s for Hydra. The smallest-magnitude ejection velocity vector for direct escape is from the center of the leading hemisphere (and slightly Pluto-ward, due to the curve of the orbit) which equates to an ejection speed of 59 m/s for Nix and 50 m/s for Hydra. Any dust ejected slower than this can only escape through a close encounter with Pluto or Charon. Dust ejected from the trailing hemisphere of the small satellites, on the other hand, must be going fast enough to both cancel out the satellite's velocity and then escape from the system. This requires an ejection speed of 340 m/s for Nix and 296 m/s for Hydra. Any dust ejected faster than this, regardless of direction, will immediately leave the system.

These different regimes can be seen clearly in Figures 3.1 to 3.4. Only a very small amount of dust ejected at 400 m/s or faster impacts either Pluto or Charon, and only then because their trajectories out of the system happen to intersect with the large bodies. Charon impacts predominately come from dust ejected at slow velocities with periapses close to Charon's orbit. The peak in Charon impacts for both Nix and Hydra dust is centered close to the minimum escape velocities (50 and 59 m/s, respectively), which corresponds to the maximum likelihood of a bound orbit which will not reimpact the source. The number of Charon impacts then falls off for higher velocities.

Pluto impacts, on the other hand, show a double-peaked structure. Most Pluto impacts have ejection velocities between 50 and 200 m/s. This range easily produces initially bound orbits with periapses close to the barycenter, and therefore Pluto. The dust particle then eventually impacts Pluto, generally after less than 20 periapse passages. The second peak for Pluto impacts is for similar velocities as Charon impacts. These trajectories initially are similar to Charon impacts, but instead have a close encounter with Charon and are perturbed into similarly tight orbits to the

higher velocity ejecta. Pluto thus sweeps up a much wider range of ejecta velocities than Charon.

3.3.2 Effects of Radiation Pressure

To probe the effect of radiation pressure on the dust trajectories, we repeated all of our simulations for particle grain sizes of 1, 10, 100, and 1000 μm. The basic effect was to increase the lifetime of the smallest particles at the slowest speeds (ejection velocity around 50 m/s), delaying the time until they either impact or are ejected. This in turn increased the Charon encounter rate, and therefore the number of both Pluto and Charon impacts for the slow ejecta. At higher velocities the dust particle size (and thus radiation pressure) had little effect on the impact rate.

3.3.3 Impact Locations

Figure 3.5 shows the longitudinal distribution of Nix dust impacts on Pluto and Charon, and Figure 3.6 does the same for Hydra dust.

Charon impacts are clearly more common for low velocity dust, and are concentrated on the leading, anti-Pluto quadrant. This corresponds to impacts of dust which is moving faster than Charon. Dust approaching Charon on both the inbound and outbound leg of the orbit will favor this quadrant. Dust on the inbound leg is moving slower as it approaches Charon than dust outbound from a periapse passage, simply due to Kepler's Third Law and the typically large eccentricity of the dust's orbit. Thus, the inbound dust has a lower relative velocity to Charon and will impact faster, while the outbound dust will take longer to impact. Both of these result in a preference for the anti-Pluto hemisphere. And since the dust's barycentric velocity is faster than Charon, the impacts are preferentially on the leading hemisphere. Thus,

the leading, anti-Pluto quadrant of Charon receives most impacts from small satellite ejecta.

Pluto impacts show a transition between slow dust impacting the trailing, Charon-facing quadrant and faster dust impacting the leading, anti-Charon quadrant. At low velocities, the inverse of the Charon impact scenario occurs. The dust is moving slower than Pluto relative to the barycenter, and so the trailing hemisphere is favored. Also, because the dust is moving slower, there is a much larger cross-section for it to impact on the Charon-facing hemisphere. The peak in Pluto impacts is when the typical Pluto-relative velocity during an encounter is close to zero. This occurs for ejections at around 150 m/s and results in a near-uniform longitudinal distribution of impacts. At higher velocities, the final trajectory of the impactor more closely resembles the Charon impactors.

3.4 Discussion

Figure 3.7 shows the albedo longitudinal distribution of Pluto and Charon from (Buie *et al.*, 2010) reformatted to be the same as Figures 3.5 and 3.6. These maps only used the albedoes from 40°N to 40°S in order to account for the lack of data south of 45°S. Pluto's most dominant features are a bright patch on the leading, anti-Charon quadrant, which is next to a very dark patch on the trailing, anti-Charon quadrant. The Charon-facing hemisphere has an intermediate albedo between the anti-Charon extremes. Charon, on the other hand, has a relatively featureless terrain (to the resolution of these maps), with a much darker overall albedo than Pluto.

Comparing the albedoes and impact distributions, it is immediately clear that unless the small satellites have similar albedoes to Charon, it is unlikely that much dust is ejected at low velocities. Otherwise, the prominent concentration of impacts on Charon's leading, anti-Pluto quadrant would be more obvious. Instead, the albedo

maps fit much better to the higher ejection velocities, with few Charon impacts and many impacts on Pluto's leading, anti-Charon quadrant. Assuming that the dust particles are primarily high albedo, their concentration on this quadrant would help to explain the bright spot, while the dark patch on the trailing, anti-Charon quadrant is simply the equatorial region that receives the least amount of dust impacts.

3.5 Conclusions

Dust ejected from the small satellites of the Pluto system can impact both Pluto and Charon. Charon impacts are much more likely from low-velocity ejections, between 40 and 60 m/s. These impacts are concentrated on the leading, anti-Pluto quadrant of Charon. Pluto impacts are most likely for higher ejection velocities (125-175 m/s), but occur for low velocity ejections too. Impacts from low-velocity ejections are centered on the trailing, Charon-facing quadrant of Pluto, impacts from high-velocity ejections are centered on the leading, anti-Charon quadrant, and velocities in between are uniform in longitude. Comparison of simulated impact fluxes and observed albedo maps shows the best match for high-velocity ejecta, potentially helping to explain Pluto's albedo distribution.

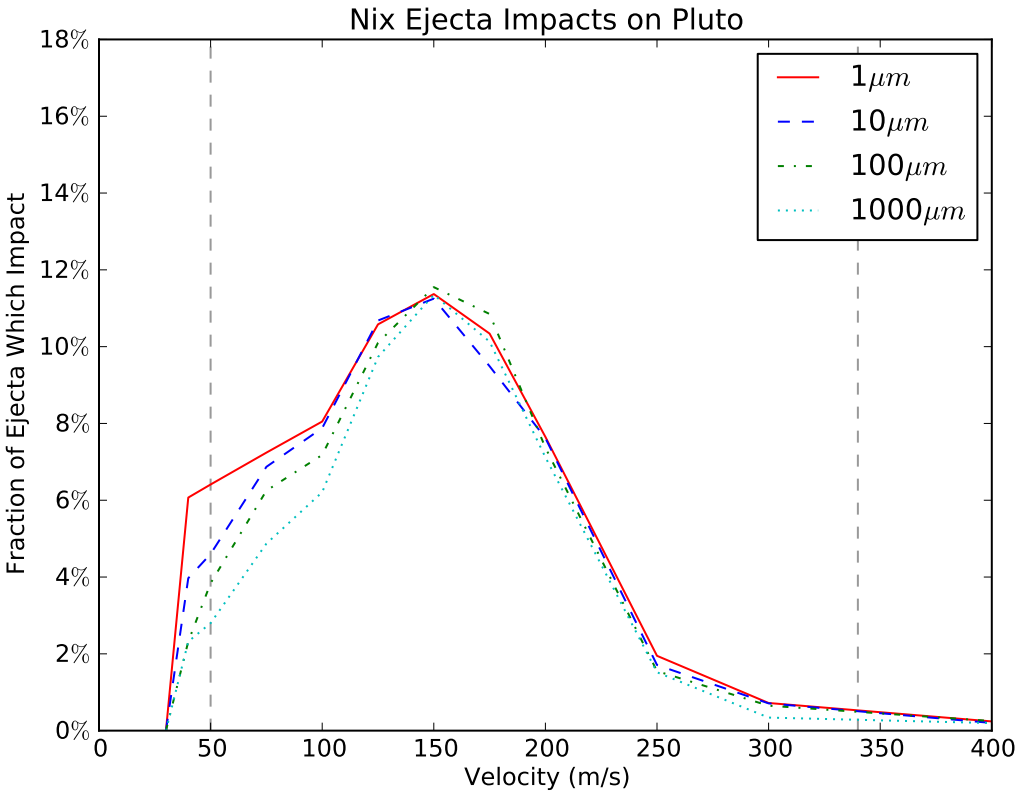

Figure 3.1: Fraction of Nix ejecta which impact Pluto as a function of ejection velocity and particle size. The vertical dashed lines correspond to the minimum escape ejection velocity from the leading and trailing points of Nix.

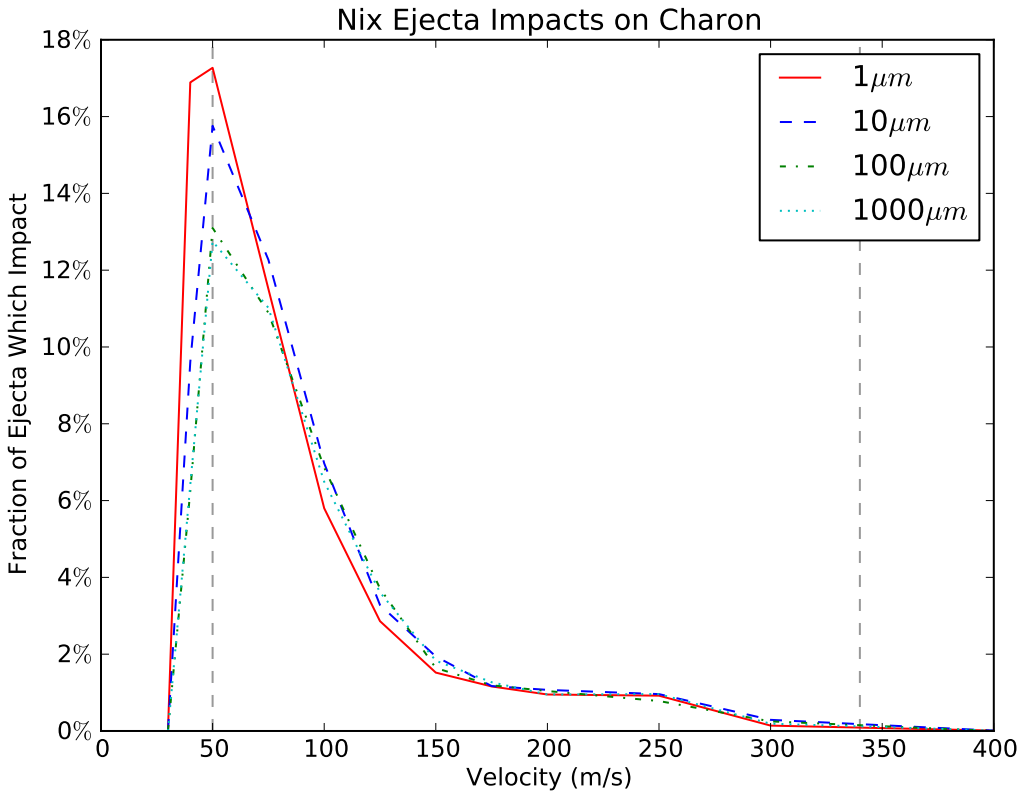

Figure 3.2: Fraction of Nix ejecta which impact Charon as a function of ejection velocity and particle size.

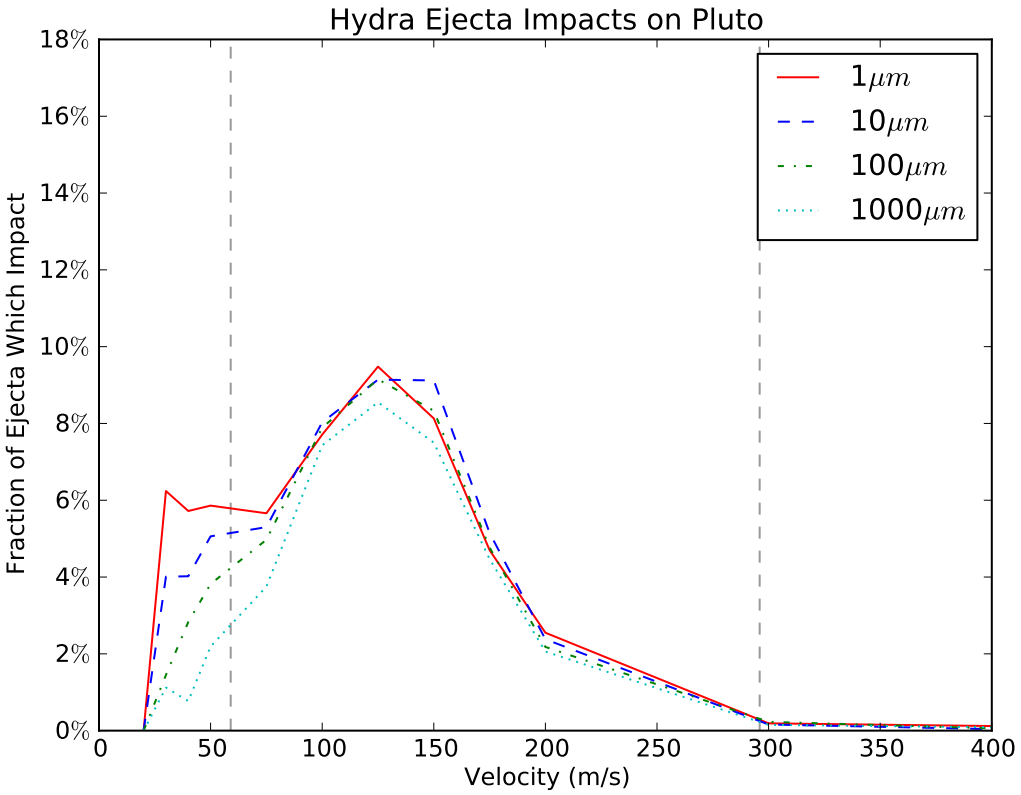

Figure 3.3: Fraction of Hydra ejecta which impact Pluto as a function of ejection velocity and particle size. The vertical dashed lines correspond to the minimum escape ejection velocity from the leading and trailing points of Hydra.

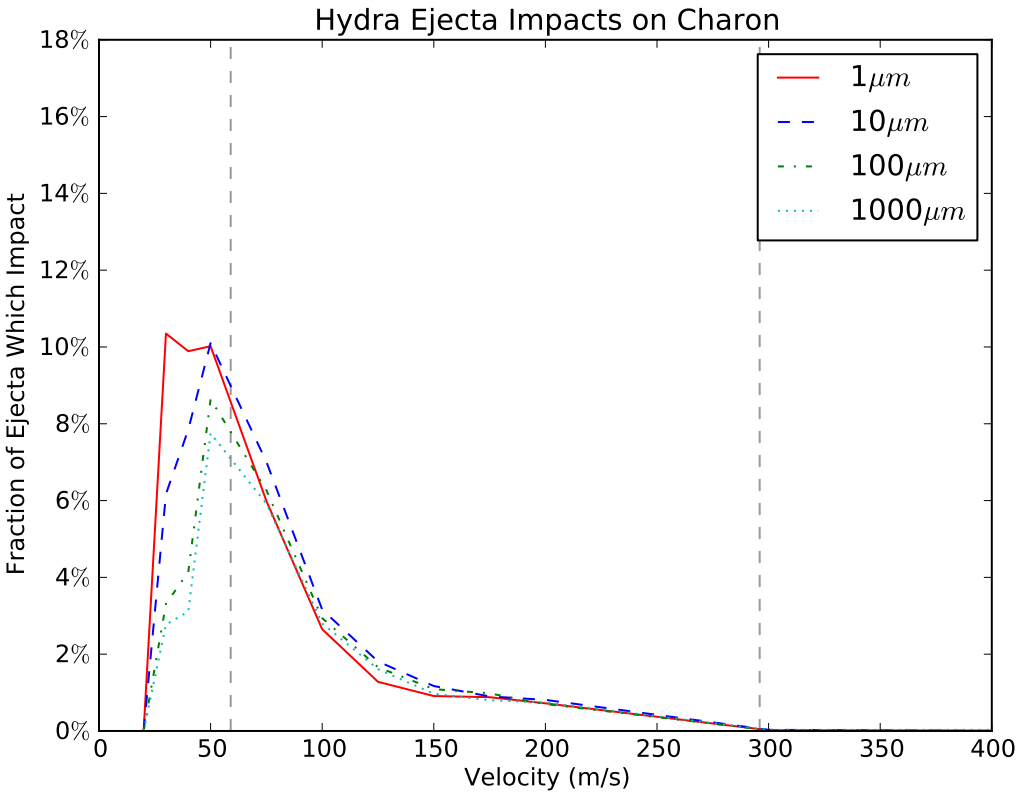

Figure 3.4: Fraction of Hydra ejecta which impact Charon as a function of ejection velocity and particle size.

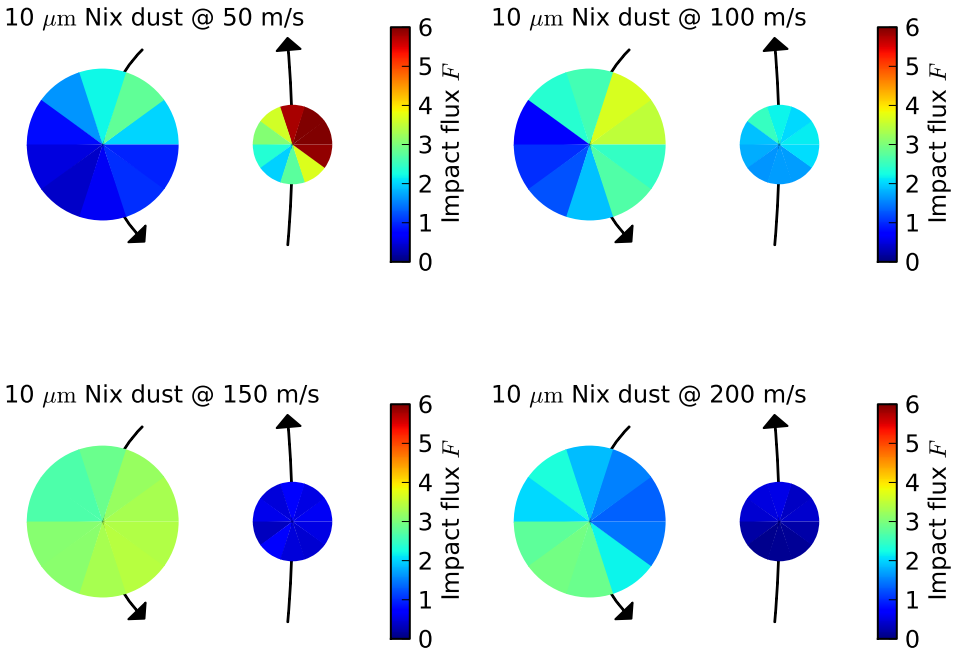

Figure 3.5: Longitudinal distribution of impacts from Nix for four different ejection velocities. The impact flux unit F is normalized to 10^4 impacts per degree longitude per ejected dust particle. Pluto is the larger circle, Charon the smaller. Both are viewed from the orbital north pole, with their barycentric directions of motion indicated by the arrows. Note that Pluto's tight orbit means that the leading point is significantly offset from the leading hemisphere, as is the trailing point.

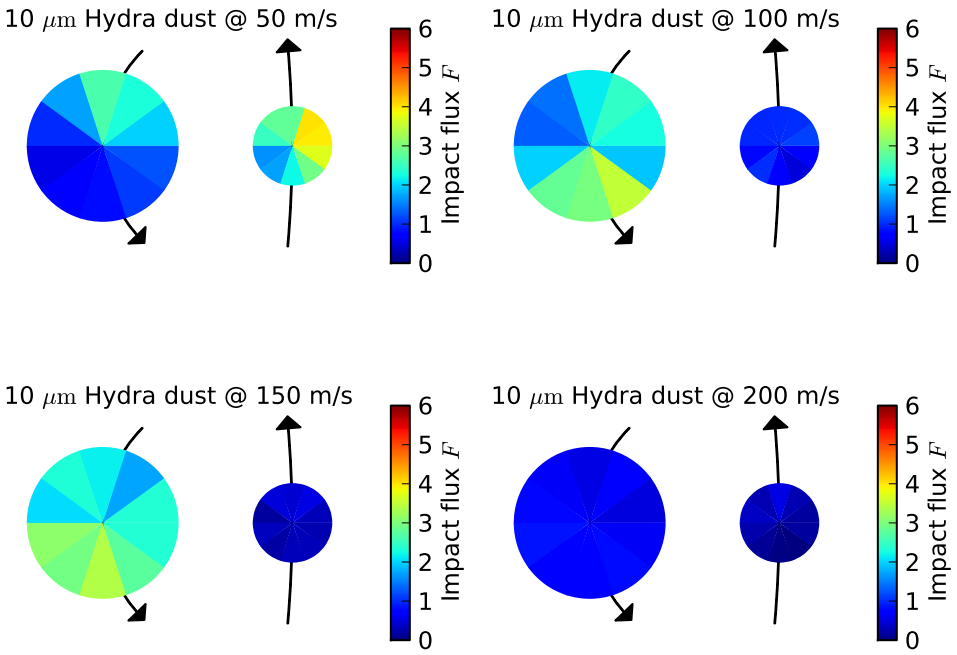

Figure 3.6: Longitudinal distribution of impacts from Hydra for four different ejection velocities. Pluto and Charon are as in Figure 3.5.

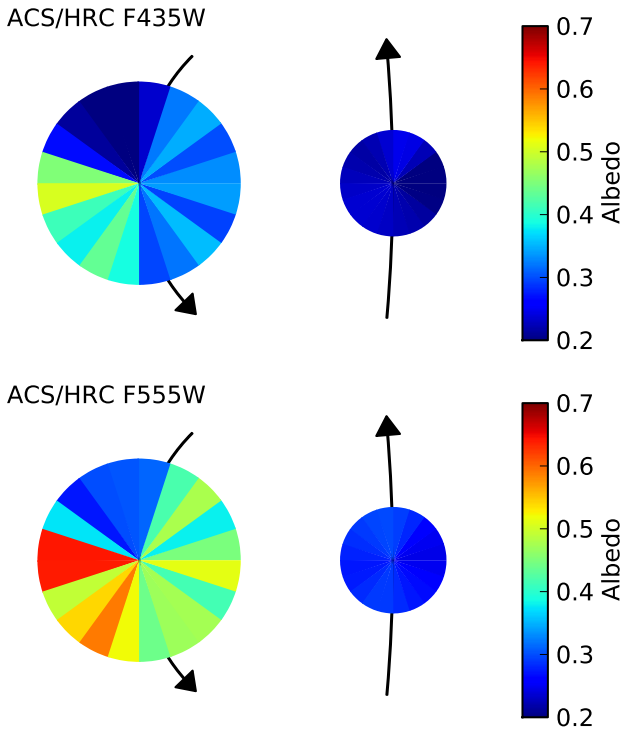

Figure 3.7: Longitudinal albedo maps of Pluto and Charon as observed with HST ACS/HRC in the F435W (blue) and F555W (visual) bands and reported in Buie *et al.* (2010). To account for the lack of data in the south, only latitudes from 40°N to 40°S are considered. Pluto and Charon are as in Figure 3.5.

Chapter 4

KCTF EVOLUTION OF TRANS-NEPTUNIAN BINARIES: CONNECTING FORMATION TO OBSERVATION

4.1 Motivation

Trans-neptunian binary systems (TNBs) constitute at least 10% of the objects between 30 and 70 AU (Stephens and Noll, 2006), and up to 30% of the Cold Classical Kuiper Belt (Noll *et al.*, 2008b). As of spring 2012, 72 TNBs have been reported in the literature, with full mutual orbits having been reported for 18 objects, partial orbits with ambiguous orbits for 30 more (e.g. Noll *et al.*, 2008a; Grundy *et al.*, 2009, 2011; Parker *et al.*, 2011, and the list at http://www2.lowell.edu/users/grundy/tnbs). These observations show that the majority of detected TNB systems have a separation of less than 2% of the Hill Radius (r_{Hill}), defined as:

$$r_{Hill} = a_{helio}(1 - e_{helio})\sqrt[3]{\frac{M_{binary}}{3M_{Sun}}} \tag{4.1}$$

where a_{helio} and e_{helio} are the semimajor axis and eccentricity of the heliocentric orbit. Even more striking is the very small fraction of TNB systems which are widely-separated (>10% a/r_{Hill}), despite their being easier to detect. This implies that TNBs are generally in very close mutual orbits, and the fraction of orbits that are very close has only increased with better detection methods. In addition, most known TNBs are of almost equal brightness (Noll *et al.*, 2008a), implying near-equal masses.

Several formation methods have been proposed to create TNBs, though none as yet can fully describe the observed population, nor account for any post-formation orbital evolution. Large impacts are an obvious contender for formation, but tend to

produce smaller satellites (and thus less equal mass ratios) than are observed. Indeed, Canup (2005) showed the Charon-forming impact required a very slow relative velocity ($v_{imp} \approx v_{esc} \approx 0.7$ km/s), and even then only allowed a mass ratio of approximately 10:1. Dynamical captures can also produce TNBs (e.g. Goldreich *et al.*, 2002; Lee *et al.*, 2007). These methods do favor near-equal mass ratios (as it provides a deeper gravity well per size of the primary object), but have great preference for producing wide (>5% r_{Hill}) binaries on eccentric orbits. Funato *et al.* (2004) combines a small impact and dynamical capture to efficiently produce TNBs, but only at very high eccentricities. Nesvorný *et al.* (2010) shows that binaries formed by gravitational collapse also tend to have near-equal mass ratios, but again have wide, moderately eccentric orbits. The unbinding of binaries by impacts (Petit and Mousis, 2004) or Neptune encounters (Parker and Kavelaars, 2010) would reduce the number of wide TNBs, but would not correspondingly increase the number of tight systems. The deficit of these wide systems, and the abundance of tight ones, therefore hints at the existence of some non-disruptive post-formation processing of TNB mutual orbits.

In this paper, we propose that Kozai Cycle Tidal Friction (KCTF, after Eggleton and Kisseleva-Eggleton, 2006) may be the method by which these orbits were tightened and circularized. We will show through several sets of Monte Carlo simulations that KCTF can transform a large fraction of primordial TNB systems into very close and circular orbits. In addition, we show that the tidal evolution this implies means that Kozai cycles are very inefficient at destroying TNB systems. We also show how KCTF is influenced by the physical properties of the TNB system, such as tidal Q and k_L, density, J_2, rotation rate, and mass ratio.

4.2 KCTF Model

In order to understand how TNB orbits may have evolved since they were formed, we created a numerical Kozai Cycle and Tidal Friction model. Kozai Cycles in this context are periodic oscillations in eccentricity and inclination of the TNB mutual orbit caused by solar torques. For this paper, the outer orbit is the heliocentric orbit of the binary's barycenter, and the inner orbit is the mutual orbit of the binary pair. These oscillations preserve the orbit's semimajor axis and the quantity $cos\ I \times \sqrt{1 - e_{in}^2}$, where I is the inclination of the mutual orbit with respect to the heliocentric orbit and e_{in} is the eccentricity of the inner orbit. This process was first described in Kozai (1962), in the context of perturbations by Jupiter on asteroid orbits. Without any tidal or quadrupole effects, these oscillations would vary eccentricity periodically with a period between approximately 2 ka and 2 Ma. Kozai (1962) showed that for an initially circular orbit, the minimum inclination for oscillation to initiate is $\pm 39.2°$. However, this limiting inclination becomes much lower at non-zero initial eccentricities. Thus, the only mutual orbits that could be excluded from this effect are those which form with both low initial eccentricity and low inclination relative to their heliocentric orbit. Kozai cycles have been suggested as a method of evolving the mutual orbits of TNBs (Perets and Naoz, 2009), as well as binary and triple Near-Earth asteroids, which may have Kozai cycles short enough to be observable (Fang *et al.*, 2011).

A significant consequence of these Kozai oscillations is that the eccentricity of the mutual orbit can become very high, especially if the initial orbit has a low eccentricity but high inclination (or vice versa). Since the tidal dissipation rate for these objects is chiefly a function of their mutual separation at periapse (see Equations 5 to 7 in Eggleton and Kiseleva-Eggleton, 2001), a minor increase in eccentricity can have a

major effect on the amount of tidal dissipation. This is important, as tidal models that assume near-zero eccentricity would produce much slower tidal evolution than is realistic for an orbit with high eccentricity due to solar Kozai effects. Mutual orbits with Kozai-pumped eccentricities can therefore decay due to tidal friction much faster than their initial state would imply; see Figure 4.1 for an example. The strength of Kozai-driven tidal decay is inversely proportional to the magnitude of the binary orbit's angular momentum as projected on the axis of the heliocentric orbit's angular momentum vector. Also, because this projected angular momentum is perpendicular to the solar-driven precession of the system, it can be completely determined from the instantaneous orbit without knowledge of the precession. Here, we normalize this quantity to a percent of the Hill radius of the system:

$$H' = cos\ I \sqrt{a_{in}(1 - e_{in}^2)\frac{100}{r_{Hill}}} \tag{4.2}$$

Where a_{in} is the semimajor axis of the inner orbit. We find this to be a particularly useful normalization, as values of H' smaller than one will experience strong body tides over the course of a Kozai cycle, while larger values generally will not (depending on their physical properties). Also, since we do not evolve the binary's heliocentric orbit in our simulations, $100/r_{Hill}$ is a constant normalization parameter. H' is effectively Tisserand's Parameter for a three-body system with only quadrupole perturbations, which is appropriate here because all known TNBs have $a_{helio} \gg a_{in}$ by at least five orders of magnitude.

Since H' is a much stronger function of the orbit's orientation than separation, even very wide binaries can be affected by KCTF if their inclination (or eccentricity) is high enough. This KCTF process has been previously identified as significant for TNBs by Perets and Naoz (2009), but only demonstrated for the Orcus-Vanth dwarf planet system (Ragozzine, 2009). We used a similar model based on Eggleton

and Kiseleva-Eggleton (2001, herein EKE01) to Ragozzine (2009), which is described below. This model directly evolves the mutual orbital elements and spin vectors of the binary while holding the heliocentric orbit constant. We did not include any dynamical effects from objects external to the binary other than the Sun. The general equations of the EKE01 KCTF model are summarized in Fabrycky and Tremaine (2007); below we describe the modifications and additions we used. These consist of our estimation of frictional timescale, quadrupole gravity terms, and integration methods.

4.2.1 Frictional Timescale

Since the EKE01 model was developed for binary stars and giant planets, we needed to modify the terms relating to the physical characteristics of the objects. One benefit of the EKE01 method is that all these terms are condensed into a single frictional timescale for each object. This timescale, however, is also a function of the mutual orbit's semimajor axis and is thus time-varying. We therefore reformulated the frictional timescale in a way that is computationally more useful.

In the EKE01 model, the behavior of the objects' body tides is determined by the second tidal Love number ($k_L = k_2$) and the tidal dissipative function (Q) for each object. The Love number is highly dependent on both the composition of the object and whether it is physically a solid object or a rubble pile. For half of our simulations, we assumed the objects were solid homogeneous elastic bodies (Burns, 1977):

$$k_{L,solid} = \frac{3}{2}\left(1 + \frac{19\mu_r R}{2GM\rho}\right)^{-1} \tag{4.3}$$

We took the rigidity of the objects, μ_r, to be $4 \times 10^9 N/m^2$, using the value for icy bodies from Gladman *et al.* (1996). For the other half of the simulations, we assumed

the objects were rubble piles, using the approximation of Goldreich and Sari (2009):

$$k_{L,rubble} = \frac{R}{10^5 \text{ km}} \tag{4.4}$$

In addition, we assumed a constant value for Q, the inverse of the average fraction of tidal energy lost to heat per radian of the orbit (Goldreich and Soter, 1966). We can then find the tidal timescales as a function of the binary's orbit (a_{in}, n_{in}), k_L, and Q. The viscosity (t_V) and frictional (t_F) timescales for the primary object as were formulated in Fabrycky and Tremaine (2007, Equations A9 and A10) as:

$$t_{V,1} = \frac{3}{2}\frac{(1+k_{L,1})^2}{k_{L,1}}\frac{Q_1 n_{in} R_1^3}{GM_1} \tag{4.5}$$

$$t_{F,1} = \frac{t_{V,1}}{9}\left(\frac{a_{in}}{R_1}\right)^8 \frac{M_1^2}{(M_1+M_2)M_2}(1+k_{L,1})^{-2} \tag{4.6}$$

The timescales for the secondary object are the same equations, but switch the subscripts 1 and 2. Combining these two equations allows a_{in} to be separated out, thus reducing the number of calculations required per iteration:

$$t_{F,1} = \frac{1}{6}\frac{Q_1}{k_{L,1}}\frac{M_1}{M_2}\frac{R_1^{-5}}{\sqrt{G(M_1+M_2)}} \times a_{in}^{13/2} \tag{4.7}$$

Note the leading factor of 1/6 is erroneously listed as 2/3 in Ragozzine (2009), leading to longer frictional timescales, and thus slower orbital decay. In addition, this timescale is for an object in a perfectly circular orbit with its rotation synchronized to the orbit. Equations 5 and 6 in EKE01 combine these factors to account for the eccentricity of the orbit and the rotation of the objects. Since the closest separation of the two objects is the key driver for tidal evolution, the effective timescale is very sensitive to eccentricity.

This frictional timescale gives the approximate rates of evolution for a near-circular orbit, but the actual rates are strongly dependant on the orbit's eccentricity. To illustrate this point, consider the special case of a system where the objects have

equal values of t_F, have $e \gg 0$, and their rotation is synchronized to the orbit, the rates of change for the semimajor axis and eccentricity can be approximated as:

$$\frac{da}{dt} = \frac{-a}{t_F(1-e)^{15/2}} \tag{4.8}$$

$$\frac{de}{dt} = \frac{-1}{t_F(1-e)^{13/2}} \tag{4.9}$$

While the eccentricity is $e \gg 0$, the semimajor axis decay can then be estimated as:

$$\frac{a}{a_0} = \frac{t_{F,0}(1-e_0)^{15/2}}{t + t_{F,0}(1-e_0)^{15/2}} \tag{4.10}$$

Where a_0, e_0, and $t_{F,0}$ are the initial semimajor axis, eccentricity, and frictional timescale. As an example, consider an equal-mass TNB system with objects having a radius of 100 km, Q=100, rubble-pile k_L, and density of 1.0 g/cm^3. At a semimajor axis of 10^4 km (100 radii), the objects would have values of $t_F \approx 7 \times 10^{12}$ years. If the initial eccentricity were 0.5, the orbit would only have decayed to 9998 km after one million years. At an eccentricity of 0.8, the semimajor axis would decay to 8512 km in that time. And at an eccentricity of 0.9, the orbit would shrink to just 306.5 km (3 radii) after a million years. By the time the system reaches an orbit this tight, t_F has decreased to less than 1000 years, allowing for rapid circularization. Clearly then, only a brief excursion to high eccentricity is needed to start a feedback loop of tidal decay to a tight circular orbit. In KCTF, those excursions happen when Kozai cycles pump up the eccentricity.

The system in Figure 4.1 shows this process in action. The two objects are equal mass rubble-piles with Q=10 and radii of 42 km. The initial orbit is at 9.7% of r_{Hill}, e=0.99, and inclination of 99°. However, the system's orientation puts it initially past the peak of its Kozai cycle, and so the orbit starts to become more circular and less inclined with little tidal evolution. After reaching a minimum of e=0.46 at 3200 years, the eccentricity then grows again. By the time it reaches e=0.98, the

semimajor axis is shrinking at a rate of 2 km/year and 45 km/year at e=0.983. The shrunken semimajor axis reduces t_F, so the peak decay rate is 150 km/year at 6550 years since the start, e=0.985, and a=6.1% of r_{Hill}. This corresponds to a periapse distance of 212 km, or 5 radii apart. The orbit then gradually decays down to a tight circular orbit at 0.15% r_{Hill} or 8.1 radii.

Most KCTF systems do not evolve as rapidly as this, and will often have several eccentricity peaks with a small amount of decay until the periapse becomes close enough for rapid decay to occur. Still, a large range of orientations can produce strong KCTF evolution. To measure this effect, we reran a number of the simulations described below without any solar perturbations. In all these cases, the number of systems which circularized was reduced by at least a factor of 3.5 compared to the full KCTF model. These systems all oriented randomly on the sphere of the sky (corresponding to observed systems), so the joint process of KCTF can cause fast tidal evolution in a large variety of TNB mutual orbits.

4.2.2 Quadrupole Gravity

Ragozzine (2009) expanded this model by adding the capacity for the objects to have a permanent quadrupole term in their gravity field. The non-uniform gravity field this allows is more physically appropriate for solid objects (like TNOs) than the stars and giant planets for which the EKE01 model was developed. This non-uniformity is especially relevant for objects the size of most known TNBs (less than 400 km diameter), which are likely not large enough to have reached hydrostatic equilibrium (Yasui and Arakawa, 2010), and thus could have relatively large quadrupole fields. The quadrupole moment is defined for an axisymmetric body as J_2=$(C - A)/(MR^2)$, where C is the moment of inertia about the polar radius, A is the moment of inertia about the equatorial radius, R is the equatorial radius, and M

is the mass. In the EKE01 model, the vector (X, Y, Z) provides the angular precession rate relative to the inertial frame, and is in the $(\hat{e}_{in}, \hat{q}_{in}, \hat{h}_{in})$ orthonormal basis, where $\hat{e}_{in}$ is the normalization of the mutual orbit's Laplace-Runge-Lenz vector, which points in the direction of the periapse, $\hat{h}_{in}$ is in the direction of the orbit's angular momentum vector, and $\hat{q}_{in} = \hat{h}_{in} \times \hat{e}_{in}$. This vector due to solar torques is given by Equations 10 to 12 in EKE01, and their relation to the secular evolution of the orbit is summarized by Equations A6 to A8 in Fabrycky and Tremaine (2007). Ragozzine (2009) formulated the additional precession due to the primary's quadrupole field as being:

$$X_{J_{2,1}} = \frac{3}{2} J_{2,1} \left(\frac{R_1}{a_{in}}\right)^2 \frac{n_{in}}{(1-e_{in}^2)^2} \frac{\Omega_{1h}\Omega_{1e}}{\Omega_1^2} \tag{4.11}$$

$$Y_{J_{2,1}} = \frac{3}{2} J_{2,1} \left(\frac{R_1}{a_{in}}\right)^2 \frac{n_{in}}{(1-e_{in}^2)^2} \frac{\Omega_{1h}\Omega_{1q}}{\Omega_1^2} \tag{4.12}$$

$$Z_{J_{2,1}} = \frac{3}{4} J_{2,1} \left(\frac{R_1}{a_{in}}\right)^2 \frac{n_{in}}{(1-e_{in}^2)^2} \frac{2\Omega_{1h}^2 - \Omega_{1e}^2 - \Omega_{1q}^2}{\Omega_1^2} \tag{4.13}$$

Where the terms a_{in}, e_{in}, and n_{in} are the semimajor axis, eccentricity, and mean motion of the mutual orbit, and R_1 is the radius of the primary. In addition, Ω_{1i} is the projection of primary's spin angular velocity vector onto the axis i. Since the binaries dealt with in this work are of similar size, this process was repeated to account for the secondary's quadrupole field, and the two quadrupole precession vectors added on to the (X, Y, Z) vectors defined in the EKE01 model. The total (X, Y, Z) vector was then combined with the dissipative terms (our Equation 4.7) to feed the full evolution equations (Equations 1 to 6 in EKE01).

4.2.3 Integration Methods

Since the EKE01 model defines the evolution of the system by a set of four related inhomogeneous vector differential equations, we needed a numerical integra-

tor that could solve them rapidly and precisely on a modern computer. For this we based our integrator on a Burlisch-Stoer method, which combines a modified-midpoint integrator with an polynomial interpolation method to increase precision and control error. Since the system was conservative when the dissipative terms where close to zero, we used a fixed timestep of 1.1 mutual orbital periods when $|V_1| + |V_2| < 10^{-18} sec^{-1}$ (equating to an approximate circularization timescale of 3.2×10^{10} years). On the other hand, if the system were dissipative, we used the adaptive timestep management algorithm described in Press *et al.* (2007), setting a minimum timestep of 10 days (864000 sec). This algorithm estimated the total error for each step as the root-mean-square of the normalized error estimates for each component ($e_{in},\ \hat{e_{in}},\ h_{in},\ \hat{h_{in}},\ \vec{\Omega}_1,\ \vec{\Omega}_2$), and kept it below a tolerance of 10^{-13} for each timestep. Throughout the simulation, the program keeps track of the total angular momentum (spin plus orbit) in the direction of the heliocentric orbit's angular momentum vector. As described above, this term determines the magnitude of solar perturbations on the mutual orbit and should be precisely preserved over the entire integration. The small number of cases (generally those with non-zero values of J_2) which did not preserve angular momentum were rerun at sufficiently smaller tolerances that momentum was again conserved. Conversely, if this tight tolerance proved to be numerically unstable, the tolerance was slowly increased until it was stable but still conservative.

We ended each simulation when it reached either 4.5 Ga (i.e. the maximum physically possible evolution time) or reached an eccentricity smaller than 10^{-4}. This value of minimum eccentricity was chosen for an end state because preliminary simulations down to 10^{-10} showed no further orbital evolution beyond circularization. In addition, the simulation would end prematurely if the periapse fell below the Roche limit ($\approx 1.26(R_1 + R_2)$, which we consider an impact), the apoapse grew beyond the

Hill radius of the system, or one of the objects reached a spin period faster than the breakup rotation rate. The condition for the latter case was a rotation rate greater than $2\pi\sqrt{G\rho/(3\pi)}$, and in practice was never reached in our simulations.

4.3 Monte Carlo Simulations

To test the responses of TNBs to the KCTF model, we conducted a series of Monte Carlo simulations in which we created a sample set of 1000 synthetic TNBs with randomized mutual orbital elements and system masses. The heliocentric orbit, physical properties, and range of rotation rates were all kept constant for each set. We then evolved each system for 4.5 billion years, or until the system either circularized, impacted itself, became unbound, or spun to breakup.

As common initial parameters, we set the heliocentric orbits to a semimajor axis of 45 AU and eccentricity of 0.05, representative of the cold-classical belt, which contains the highest fraction of TNBs. We then varied the system GM range from 0.02 to 0.20 km^3/s^2. This corresponds to a radius range from 33 to 71 km for an equal-mass, $\rho = 1.0$ g/cm^3 system, appropriate for the lower range of detectable TNB systems. The semimajor axis of the mutual orbit (in the frame of the primary) was varied uniformly from 0.1% to 10% of the system's Hill radius. This range is inclusive of nearly all known TNB orbits, as well as published formation models. The mutual eccentricity was varied uniformly from 10^{-4} to 0.9999. The orbits were all orientated randomly on the sky by first generating a random direction for the $\hat{h_{in}}$ vector with the algorithm of Knop (1970). A second random vector perpendicular to the first was then generated and used as the $\hat{e_{in}}$ vector. These two vectors plus the semimajor axis, eccentricity, and system mass then fully describe the randomized orbit. This random orientation corresponds to dynamical simulations of binary capture (Kominami *et al.*,

2011). Likewise, the initial spin poles of the two objects were pointed at two different vectors also randomized on the sky.

We considered two different densities, 0.5 and 1.0 g/cm^3, representative of the range of reported densities for binary TNOs in this size range (Stansberry *et al.*, 2012). As noted above, we also considered both solid and rubble-pile assumptions for k_L. For each simulation set, we replicated the runs for each of the four combinations of density and k_L. For most of the simulations, we allowed the initial rotational periods of the objects to vary between 4-48 hours. This range is consistent with observed lightcurves for solitary TNOs (Trilling and Bernstein, 2006; Thirouin *et al.*, 2010). To check the sensitivity of this range, we also ran simulations with 2-7 day rotation rates. We ran most of our simulations with J_2=0, but we also ran sets at J_2=0.01 and J_2=0.1. The former being comparable to Saturn's satellite Phoebe, and the later to Hyperion, both of which are in the same size range as our simulations. We ran most simulations with Q=100, a typically canonical value for large solid objects. However, since smaller objects may have much smaller Q (Goldreich and Sari, 2009; Zhang and Hamilton, 2008), we also performed a set of simulations with Q=10. Finally, in addition to the equal-mass simulations, we ran a set with a mass ratio of 10:1. Since most observed binaries have a brightness difference of less than one magnitude (Noll *et al.*, 2008a), these two mass ratios are representative of the observed population.

The parameters varied per each set of 1000 simulations were thus Q, J_2, rotation rate, mass ratio, density, and k_L. Table 4.1 lists the 24 sets considered, for a total of 24,000 simulations and approximately 1 million CPU-hours. Because the initial conditions of these systems were distributed across reasonable ranges of a, e, i, and obliquity, they do not necessarily represent the primordial population of TNBs. Rather, they are a superposition of all the possible initial states. KCTF can then

act as a filter to check whether a certain range of initial orbits (and thus formation methods) corresponds to the observed population of TNBs.

4.4 Results

We found that a significant fraction of our simulations resulted in the synthetic TNB systems evolving to very tight circular orbits; Table 4.1 lists the relative fractions for each simulation. These tight, circular orbits were at less than 1% of r_{Hill} and eccentricities smaller than 10^{-5}, meaning that they were entirely dominated by mutual tidal interactions. In addition to these highly-evolved systems, a number of systems evolved to orbits that were tighter but still eccentric. Figure 4.2 shows the time evolution of one set of simulations and Figure 4.3 separates initial and final states for the circularized and elliptical cases of the same set. The conservation of H' is quite evident in these plots, as is its dependence on $cos\ I$ and $\sqrt{a}$. Figures 4.4, 4.5, and 4.6 show the final states of a range of different simulation sets, varying in both the speed of body tides and physical shape.

Much of the tightly-bound population is beyond current TNB detection methods, including the WFC3 camera on the Hubble Space Telescope and the laser guide star adaptive optics system at the Keck Observatory. However, some of the known TNO orbits do fall within this population. The closest published full orbit is (79360) Sila-Numan, formerly 1997 CS_{29}, at 0.35% r_{Hill} (Grundy *et al.*, 2012). The published eccentricity is 0.02, but a fully circular orbit is only excluded at 1.8 σ confidence. In addition, (120347) Salacia-Actaea at 0.23% r_{Hill} (Stansberry *et al.*, 2012) and the centaur (65489) Ceto-Phorcys at 0.46% r_{Hill} (Grundy *et al.*, 2007) both have extremely circular orbits. These three objects likely represent the inner edge of the potentially very numerous tight circular population, and should become less unique as observations improve.

Our simulations also naturally produced a deficit of systems with a final semimajor axis smaller than $1.26\times(R_1+R_2)$, our approximate Roche limit. It is perfectly possible that these systems could survive, either as a contact binary or breaking apart and reforming in a more stable configuration (Jacobson and Scheeres, 2011). However, any of these cases are beyond the capabilities of our model and would require further work. This inner edge corresponds to a J/J' of approximately 0.4, where J is the total orbit + spin angular momentum, $J' = \sqrt{GM_t^3 R_{eff}}$, M_t is the system mass, and R_{eff} is the radius of a sphere of mass M_t and density equal to the average density of the two objects. Canup (2005) showed that binaries with $J/J' < 0.8$ can be produced by collisions. Thus, we found that KCTF can transform a wide range of binaries formed by capture into ones sufficiently close as to be indistinguishable from collision-produced binaries, the general case of what was shown for Orcus-Vanth by Ragozzine (2009).

Because the quadrupole component of Kozai perturbations are axisymmetric, the resulting systems also preserve the direction of their initial mutual orbit relative to the plane of their heliocentric orbit. The EKE01 model only includes the quadrupole component, though in the actual dynamics of these systems there are also higher-order terms. The next higher term is the octupole component, which is not axisymmetric and can therefore cause a system to flip from prograde to retrograde (and vice versa, Naoz *et al.*, 2011). However, the relative strength of the octupole to the quadrupole goes as a_{in}/a_{helio}, and so the quadrupole completely dominates in all the cases we considered (Ragozzine, 2009). Thus, the initial prograde/retrograde ratio was preserved in all our simulations.

4.4.1 Stability of Orbits to KCTF

A further inclination effect can be seen in Figure 4.3; the inclination region within 10° of perpendicular to the heliocentric orbit is empty for all but the tightest semi-major axes. This range of inclination equates to such low values of H' that all orbits starting there reach very high levels of eccentricity, and therefore initiate runaway KCTF decay (e.g. Figure 4.1). Figure 4.5 clearly shows that these orbits mostly end up tighter than 1% of r_{Hill}. Indeed, as Figure 4.5 shows, there is a clear limiting value of $|H'|$ below which orbits are not stable to KCTF.

We define this limiting value, $|H'_{tide}|$, as the minimum value of $|H'|$ where the relative difference in the initial and final semimajor axes is less than 10%, i.e. $|a_i - a_f|/a_i < 0.1$. The values of $|H'_{tide}|$ for all our simulations are listed in Table 4.1. The average values of this $|H'_{tide}|$ are all close to 1.0, with the higher-dissipation cases above and the lower below. Thus, $|H'|$ appears to be a good normalized indicator of KCTF susceptibility for TNB orbits; values below 1.0 likely will have experienced Kozai cycle-driven tidal evolution, while values above will likely have not. This is especially useful for determining the stability of observed binary systems where the mutual orbit is known, but not any physical or rotational properties.

In addition, we found it useful to define $|H'_{circ}|$, the minimum value of $|H'|$ for an orbit that did not circularize. This value ranges from 0.2-0.7 for non-J_2 runs, but is close to zero for the simulations with J_2. This shows that J_2 can provide an island of stability for eccentric orbits close enough that J_2 blocks further Kozai cycles, but not close enough for further tidal decay. These systems have tidally evolved beforehand to reach this state, but are stable once they reach it.

4.4.2 *Effects of Physical Parameters*

For our base sets of simulations, we assumed Q=100, J_2=0, rotation rates between 4 and 48 hours, and equal masses for the two objects. Using these parameters, we ran sets at each combination of density equals 0.5 or 1.0 g/cm^3 and a Love number appropriate for either a rubble pile or elastic solid body. The remainder of the simulations perturbed one of the first set of parameters and ran the same set of four density/Love number combinations; Table 4.1 shows this grouping.

In general, the low-density rubble piles were the most susceptible to tidal decay, followed by the high-density rubble piles. This makes sense, as the internal friction of a rubble pile allows it to dissipate tidal forces very effectively. The lower density allowed a larger radius per mass, thus raising larger tides and a higher Love number (by Equation 4.4). Less obvious is that fewer of the low-density elastic solid simulations decayed to stable circular orbits than the high-density cases. Here, the difference can be seen in the final column of Table 4.1; these low-density, rigid systems suffered a much higher rate of mutual collisions. Their larger radius prevented a significant fraction of the very eccentric systems from circularizing, lowering the overall efficiently of producing close, circular orbits. As noted below, these mutual collisions could still produce close or contact binaries, but that is beyond the capabilities of these simulations.

While we assumed the canonical value of tidal Q=100 for most of the simulations, a lower value is likely more physical for the size of objects we considered (Goldreich and Sari, 2009). The simulations that we ran with Q=10 did show an average of 20% greater propensity to tidally decay and circularize. This small increase in tidal decay for a full order of magnitude decrease in Q shows the true driver in this evolution is the closest periapse the system reaches. Either the objects become close enough

to undergo decay or they do not, there is not much space in between. Indeed, the increase is roughly comparable $(100/10)^{1/8}$, where the strength of the tides goes as a^8. An additional effect of the lower Q is to remove the higher mutual collision probability for the low-density, elastic solid case. As shown in Figure 4.4, the faster tides allow these cases to circularize at larger separations, limiting the impact probability.

We ran sets of simulations with a J_2 of both 0.01 and 0.1. As seen in Figure 4.6, the main effect of J_2 on wider systems was to decrease the obliquity of the objects with respect to their mutual orbit. For slightly more evolved systems, though, an interesting effect could be seen; a number of the systems decayed to a point where J_2 was strong enough to block further Kozai cycles, but their periapse was wide enough at the point of being frozen that no further tidal decay could occur. This freezing-in of Kozai-blocked systems created the island of high-inclination, moderately eccentric systems seen in Figures 4.3 and 4.5. Since the frozen systems did not evolve further, they reduced the total fraction of systems that circularized. However, since they had to first tidally evolve to reach the frozen state, the total fraction that tidally evolved (and thus $|H'_{circ}|$) is almost the same as the non-J_2. Also, since tidal evolution is strongly driven by the periapse, there is a noticeable gradient in eccentricity, with the closest frozen systems having $e < 0.2$. Thus, the effect of J_2 on KCTF of TNBs is produce stable high-inclination, moderately eccentric TNBs, while not eliminating the tight circular population.

We also ran a group of simulations with much slower initial rotation rates, from 2-7 days (and at random initial orientations, just as before). These simulations were slightly less likely to evolve to close circular orbits than their fast rotating counterparts. This may be because the final orbital periods of the close circular orbits were closer to the initial rotation rates of the faster rotators. Thus, the slower rotators required, on average, a larger amount of spin-orbit interaction to reach a doubly-

synchronous state (with both spin periods equal to the orbital period). The effect was slight enough, though, to conclude that initial rotation rate is not a significant factor in the evolution of these TNBs.

Finally, we changed the mass ratio of the two objects to be 10:1. Since most known TNBs have near-equal brightness ratios (Noll *et al.*, 2008a), this covers most of known TNBs that are not dwarf planetary systems. The effect on tidal decay was again similar to the slower initial rotation rates, a slight decrease in the efficiency of producing close circular orbits. Here the reason is that most of the dissipation is taking place on the secondary, which can only have smaller tides due to its smaller radius. Again, though, the effect is slight enough that most systems would be completely insensitive to mass ratios between 1:1 and 10:1.

4.4.3 Survival Probability

Not all of the simulated binaries survived to either circularize or reach 4.5 Ga. As shown in Table 4.1, about 1-15% of our random initial orbits proved in some way unstable. The largest fraction of destroyed systems was due to impacts when Kozai Cycles drove the periapse of the system within the mutual Roche radii of the objects. This was especially apparent for systems with elastic solid values of k_L (weak tides) and large radii, which consistently had destruction rates higher than 10%. Every other case had destruction rates smaller than 10%. As noted above, this is because the low-density solid systems circularize slowly enough that semimajor axis decay can bring their periapse below the Roche limit. In real TNBs, such a close approach could result in the temporary breakup of the secondary and reformation of one or more new satellites in tight circular orbits. The simulated systems were also considered destroyed if the apoapse of the system exceeded r_{Hill}, though this case did not occur in any of our simulations. Likewise, we had no systems spin to breakup, with spins

either slowing to synchronize or not changing at all (see Figure 4.6). It therefore appears that mutual collisions are the only practical way to destroy a TNB system with KCTF, and even then only with an efficiency of a few percent. In addition, 90% is a lower limit for the number of TNBs (of an initially random population) which survive as binaries once formed, exclusive of impacts or close encounters.

The survival rate in our simulations is much higher than that calculated by Petit and Mousis (2004), who found that non-disruptive impacts were the most effective means of destabilizing wide TNBs. This implies that small impacts and disruption by Neptune encounter (Parker and Kavelaars, 2010) are still the most efficient means to cause a TNB to become unbound. However, our results show that KCTF is very efficient at transforming wide binaries into tight ones, which would presently be observed as single objects. Indeed, KCTF can quickly shrink wide binaries down to orbits tight enough to have a high survival probability in the event of a Neptune encounter (Parker and Kavelaars, 2010). Thus, any scaling of the initial population of wide TNBs based on survival rates must also account for the fraction which decay into much tighter orbits.

4.4.4 Obliquity

All the systems we simulated started out with randomly directed spin axes, and thus each object had random initial obliquities. We define obliquity here to be the angle between the spin pole of the objects and a vector perpendicular to the plane of the mutual orbit. Thus, an obliquity of 0° is parallel to the orbit's angular momentum vector, while an obliquity of 90° is perpendicular. Figure 4.6 shows the final obliquities of equal-mass, Q=100 simulations with and without J_2.

In general, the non-J_2 runs experienced two stages of obliquity evolution. At less than about 3% r_{Hill}, the spins of the two objects begin interacting with each other

and with the orbit. This causes any objects rotating retrograde to their orbit to flip around to prograde, causing the step jump in Figure 4.6. In addition, the two objects begin to match their obliquities and rotation rates to each other, thus producing the star shapes in Figure 4.6. The second (and terminal) stage is for the objects to match their spin poles and rotation rates to their mutual orbit. This drive to zero obliquity only occurs for the non-J_2 simulations when tidal forces are also strong enough to circularize the orbit.

The simulations with J_2 were similar, but the additional gravitational factor from J_2 caused them to go to zero obliquity much faster. Indeed, even some very wide orbits with little tidal evolution were still driven to zero obliquity by J_2. Shape effects thus can have a major effect on the rotational evolution of even wide systems.

A further effect can be seen in Figure 4.6, as some circularized orbits ended with non-zero obliquities and non-synchronous rotation rates. This effect was more pronounced for less-dissipative simulations. These systems appear to have been captured into Cassini state 2, which is low obliquity for fast precession and high obliquity for slow precession (Fabrycky *et al.*, 2007). As they circularize at near-constant semi-major axes, their precession rate due to J_2 drops (equations 11-13). Since they are sufficiently close that J_2 precession dominates, the overall precession rate becomes very small and the objects follow Cassini state 2 to high obliquity.

This capture process is not necessarily observable in real systems. Most small objects with known shapes (asteroids and minor satellites) are not pure oblate spheroids, but rather more complex shapes. It is possible for these shapes to capture into Cassini state 2 (Peale, 1969; Bills and Nimmo, 2008), but it is much more difficult. In addition, they may have precession rates due to higher-order terms that are large enough to prevent even a very circular system in Cassini state 2 from going to high obliq-

uity. Thus, a much more through study of the possible post-circularization rotational evolution of TNBs is needed to properly predict their current states.

4.5 Discussion

KCTF provides an evolutionary path to convert wide, elliptical binaries into close, circular ones. It therefore helps to explain the observed dichotomy between the few (but well-sampled) wide TNB systems and the apparently numerous tight systems. In addition, because it is a process that does not require any external forces other than the Sun, it applies to all objects that could be called trans-neptunian binaries, from classical Kuiper Belt objects to highly scattered centaurs like Ceto-Phorcys. And, because it is independent of the surrounding disk, KCTF can shrink and circularize orbits over a much longer timescale than disk dynamical friction (e.g. L^2S).

A consequence of this extensive evolution is that KCTF should have significantly reshaped the orbits of most TNBs since their formation. In the process, some information is lost, as tidal decay is an irreversible thermodynamic reaction. The distribution of semimajor axes for present-day TNBs is thus necessarily tighter than at formation. By what factor it is tighter is hard to determine, as the physical properties of the objects do affect the efficiency of semimajor axis decay (see Table 4.1). Similarly, the exact eccentricity and inclination of the orbit are changed in ways that have partially erased their history.

More clear is that KCTF generally preserves the prograde/retrograde ratio of initial distribution. Though the octupole term from the solar perturbations can flip a very inclined system (Naoz *et al.*, 2011), it also has no preference for the directionality of the system. Schlichting and Sari (2008) predicted a retrograde preference for binaries formed by the L^2S capture method. On the other hand, the gravitational collapse method of Nesvorný *et al.* (2010) favors orbits in the direction of disk clump

rotation, which simulations (cited therein) generally show as prograde. Three-body methods (L^3 and momentum exchange) have a much weaker inclination dependence. The current inclination distribution could therefore serve as a tracer for these various formation methods. Because the sense of motion can be hard to determine for TNBs, only a few TNBs have published unambiguous inclinations. However, for the 16 TNB orbits listed in Table 4.2, there is a 4:1 prograde preference.

The H' parameter introduced above is also preserved by KCTF (except for spin-orbit interactions), and Table 4.2 also lists the H' for those 16 known orbits. The widest orbits ($a > 5\%r_{Hill}$) are apparently stable, with their large a and low inclinations keeping them stable even at high eccentricities. These systems likely have thus been undergoing low-amplitude Kozai cycles for most of the history of the solar system. Table 4.3 lists the known TNB systems in near-circular orbits; these systems appear to represent the outer edge of the close circular population identified in our simulations. As more sensitive high-resolution imaging systems come on line, an increasing number of these tight systems should be detected. The remaining systems smaller than $5\%r_{Hill}$ have values of $|H'|$ at or below unity, implying that they all should have some amount of tidal evolution. Most still have a larger $|H'|$ than the typical values of $|H'_{circ}|$ in Table 4.1, meaning they could have a range of physical properties and still not circularize.

Two eccentric systems do have an $|H'|$ small enough to stand out, though: 2004 PB_{108} and 2001 QC_{298}. These two systems happen to be the only scattered-disk binaries by the DES classification (Elliot *et al.*, 2005; Osip *et al.*, 2002) in Table 4.2, but we think it more likely that their apparent stability is due to their non spherical shapes. Indeed, Table 4.1 shows that if both of the objects in each system had a J_2 of at least 0.01, they could easily be stably eccentric for the lifetime of the solar system.

The other eccentric systems do not require J_2 to be stable, but it would do no harm to their stability.

The three systems just wider, 2001 XR_{254}, Altjira, and 275809, all have values of $|H'|$ just larger than one. Since they are all also in the classical Kuiper Belt, these systems have potentially had very little tidal evolution since their original formation as binaries. Interestingly, they also have very similar systems masses and mutual orbit inclinations. Future investigations could help determine if this is simply coincidence or an optimal point for stability.

4.6 Conclusions

KCTF can significantly transform the orbits of trans-neptunian binaries. At least 90% of random synthetic TNB systems survive 4.5 Ga of KCTF evolution. A third to half of the surviving TNB systems decay to circular orbits at less than 1% of their mutual Hill radius. Some of these systems can have values of J/J' similar to impact-generated systems. The remaining systems are stable being eccentric over the lifetime of the solar system. All resulting systems preserve their initial prograde/retrograde preference.

The inclusion of J_2 lowers the effectiveness of KCTF, but does not eliminate it, especially for rubble-pile objects. In addition, J_2 creates an island of stability that allows otherwise unstable observed system to be in permanent eccentric orbits. A slower initial rotation rate or 10:1 mass ratio also slightly lower the effectiveness of KCTF, but do not change the basic trends.

The observed population of TNB orbits fits well to our simulations with J_2. These simulations predict that, as high-resolution observational systems improve, a large number of TNBs will be detected with very tight, circular orbits. Indeed, considering

the fraction of known wider binaries, tight near equal-mass TNBs may be extremely common.

4.7 Acknowledgements

This work was partially supported by grants HST-GO-11178 and HST-GO-11650 from the Space Telescope Science Institute, which is operated by the Association of Universities for Research in Astronomy, Incorporated, under NASA contract NAS5-26555. Partial support was also provided by NASA through Spitzer Space Telescope Cycle 5 grant RSA#1353066 funded through a contract issued by the Jet Propulsion Laboratory, California Institute of Technology under a contract with NASA. Partial support was also provided by NSF Planetary Astronomy grant AST-1109872. Special thanks to Frank Timmes and Travis Barman for contributing to the many CPU-hours it took to complete this project. Thanks also to Darin Ragozzine and an anonymous reviewer for their helpful comments and suggestions.

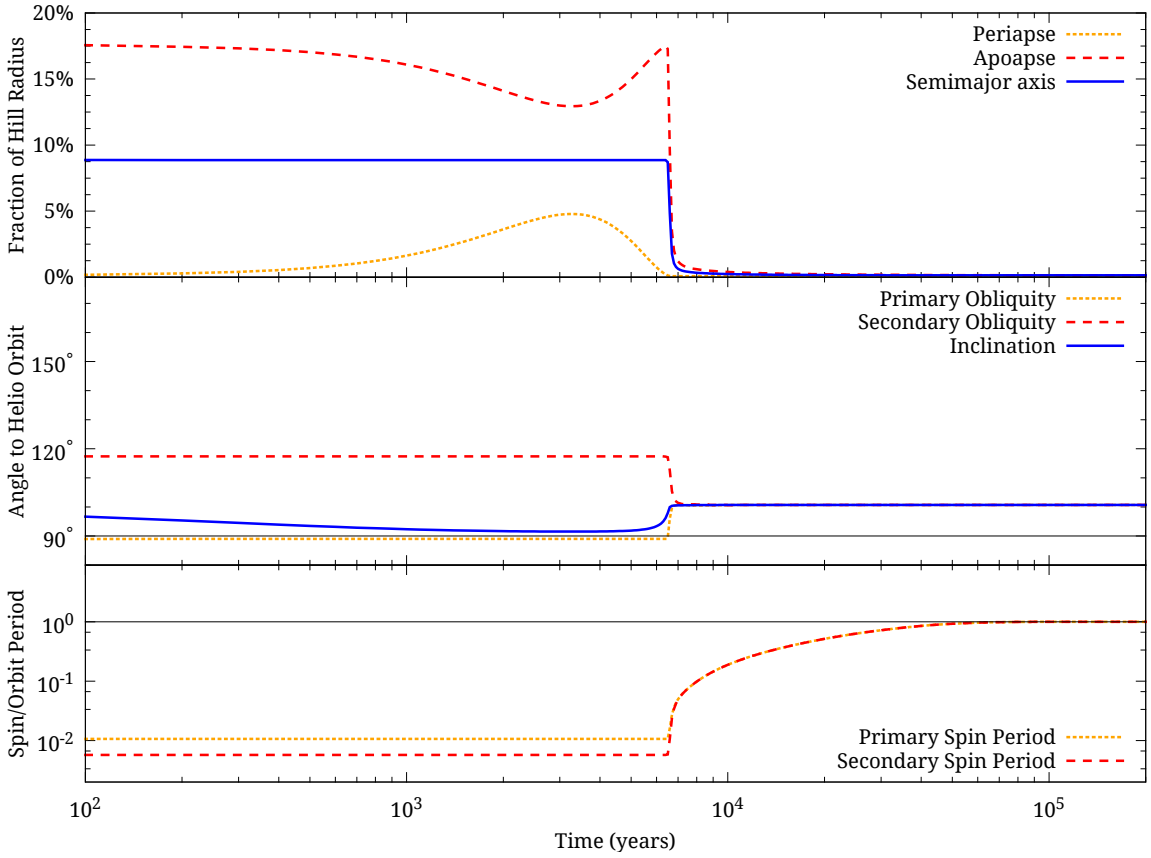

Figure 4.1: An example of rapid KCTF evolution of a TNB mutual orbit; see Section 2.1 for a full description.

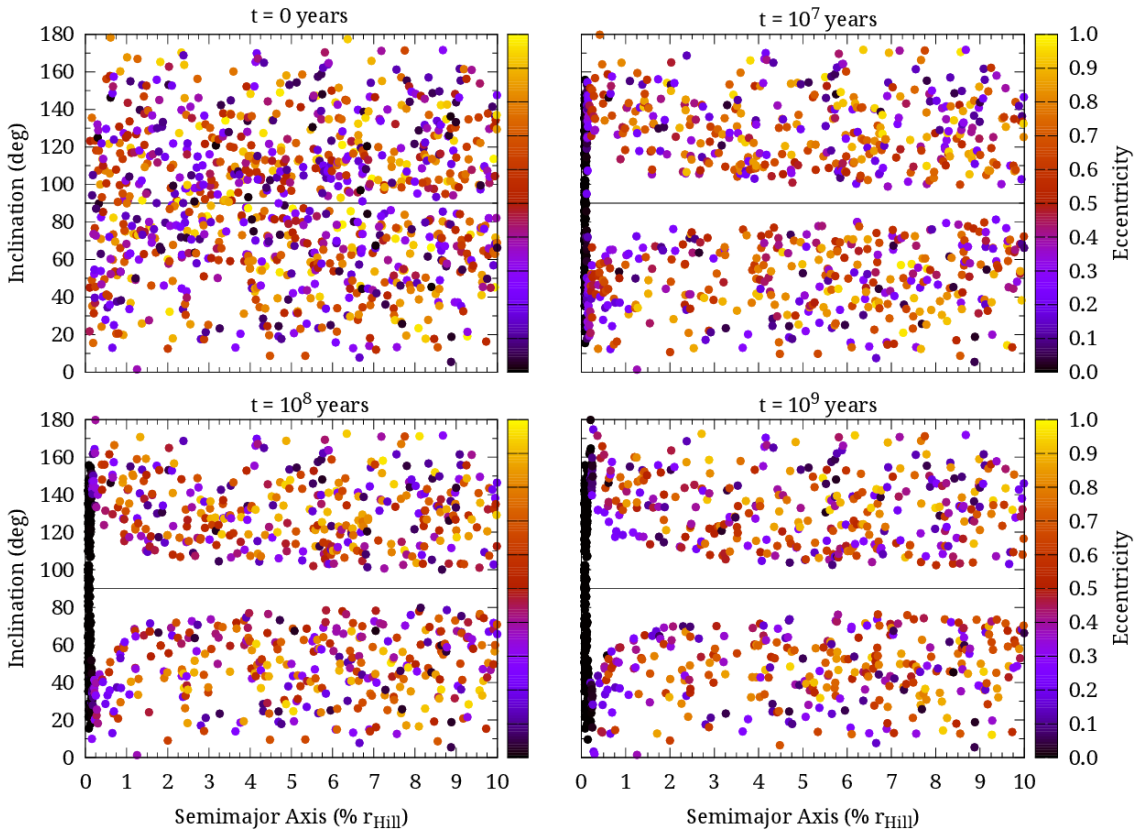

Figure 4.2: The evolution over time of 1000 synthetic equal-mass TNBs with $Q = 100$, $\rho = 1.0$ g/cm^3, elastic solid k_L, and $J_2 = 0$.

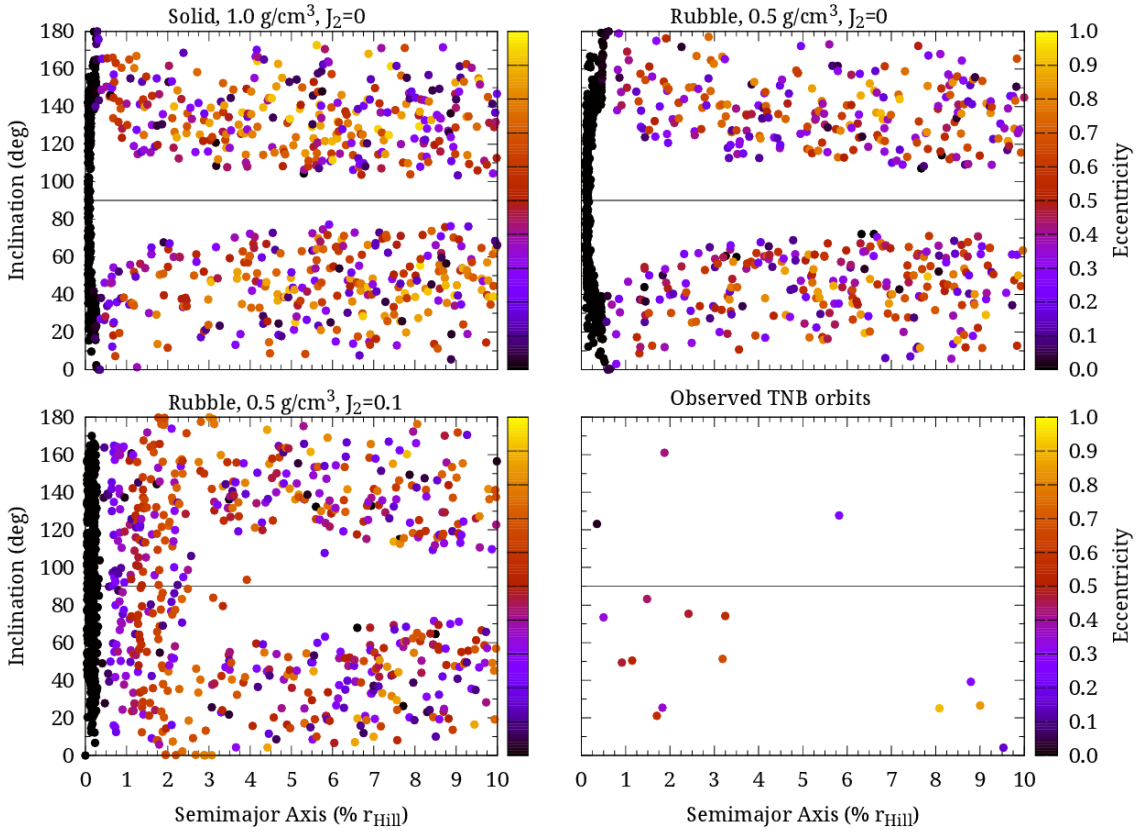

Figure 4.3: A comparison of end states for three different physical properties and observed orbits. The simulations are all equal-mass, $Q = 100$. Observed orbits are as listed in Table 4.2.

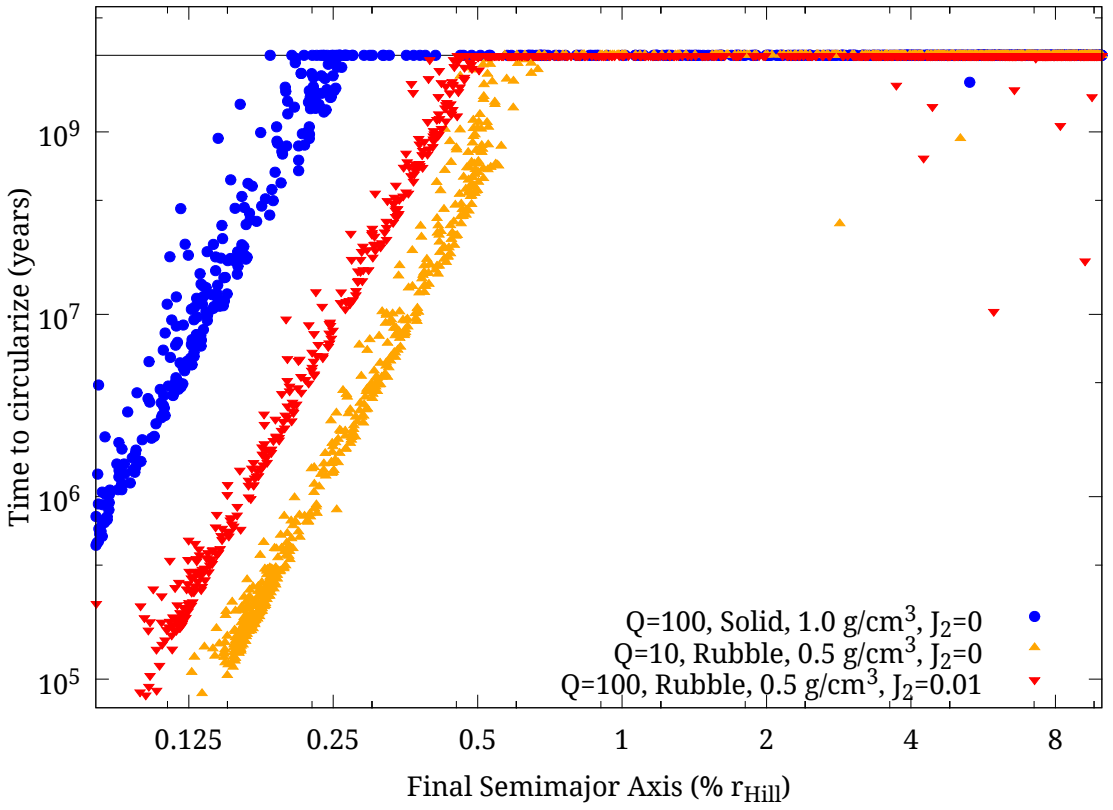

Figure 4.4: The circularization times for three different physical properties; the simulations are all equal-mass systems. The horizontal line corresponds to 4.5 billion years, and any points along it represent stable elliptical orbits. The points on the left below the line are simulations that were evolved by KCTF to close circular orbits, while the points on the right below the line started at very low eccentricity and evolved to $e < 10^{-4}$. The final semimajor axis in tidally-evolved systems is usually very close to the periapse of the orbit when body tides become the dominant force, as most of the energy loss in an evolving orbit is at the periapse.

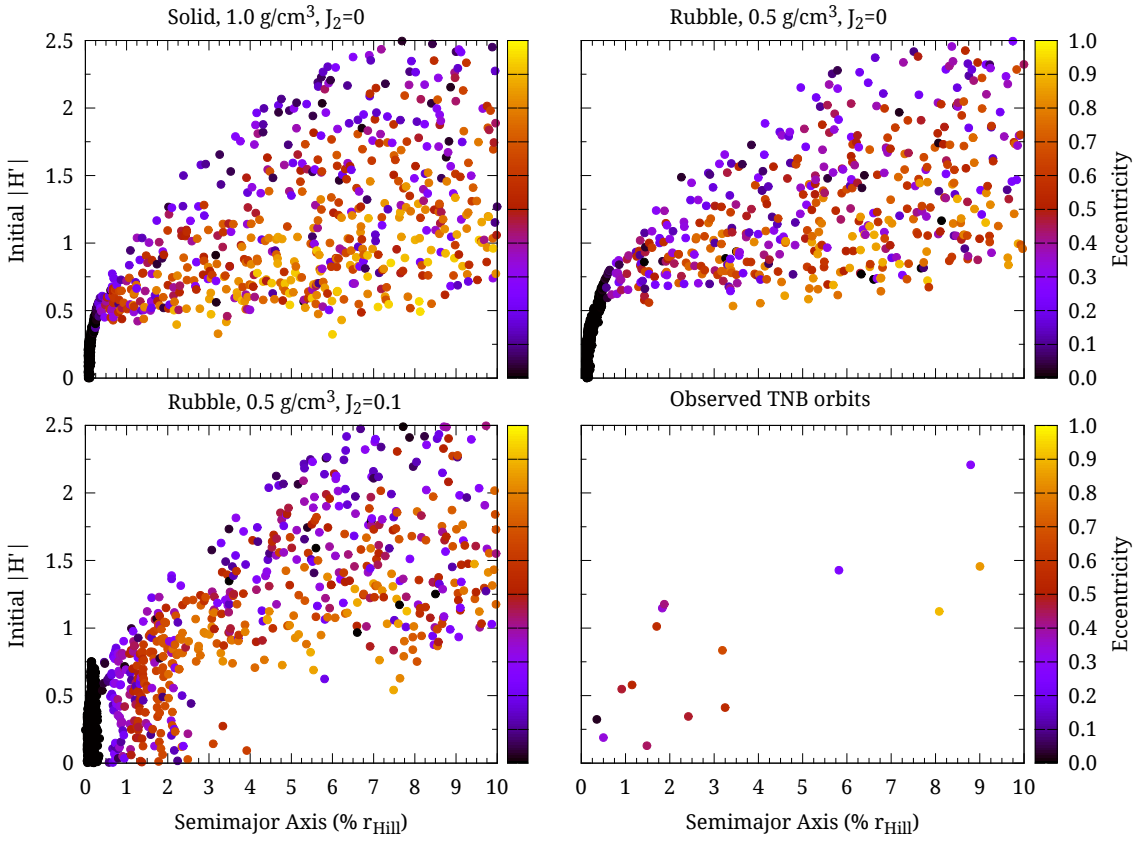

Figure 4.5: A comparison of initial $|H'|$ and final semimajor axis for three different physical properties and observed orbits. The simulations are all equal-mass, $Q = 100$. Observed orbits are as listed in Table 4.2.

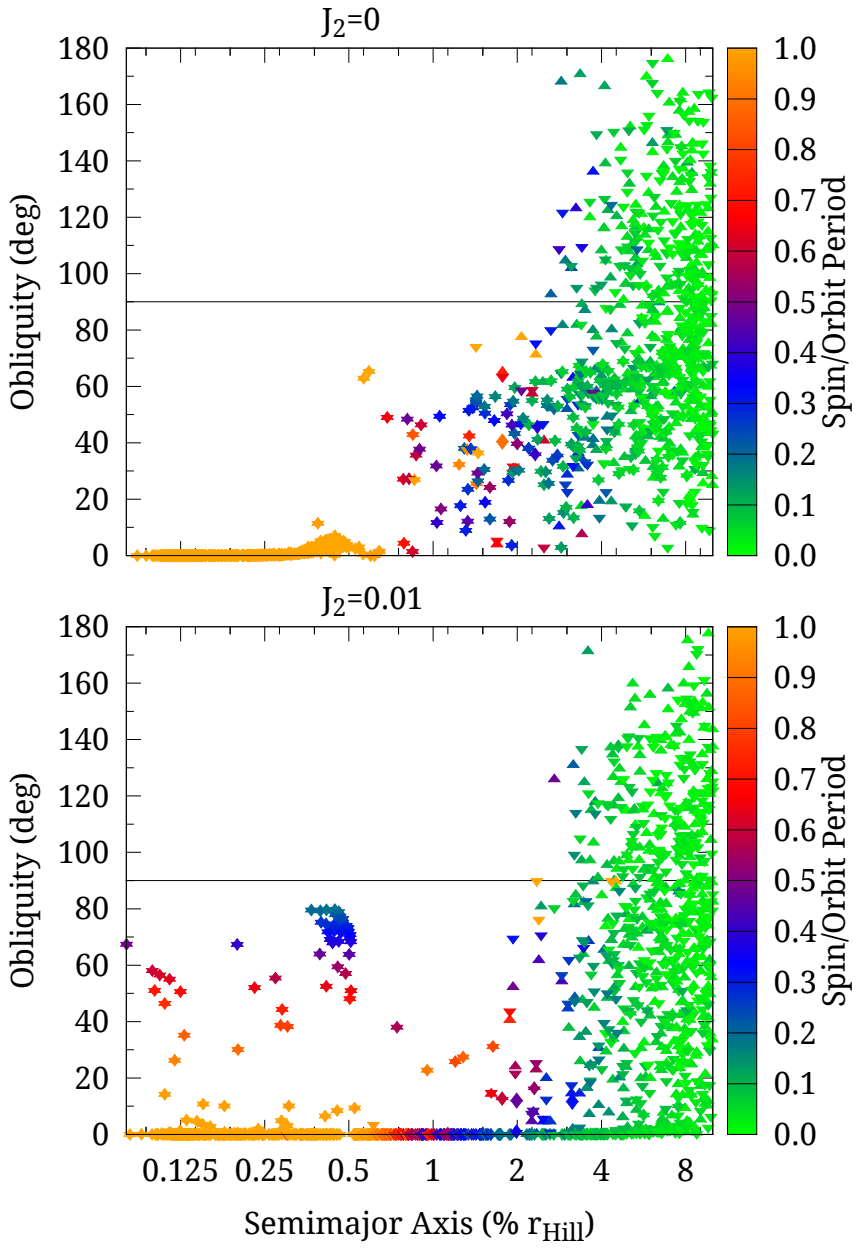

Figure 4.6: The final spin rate and obliquity (to the mutual orbit) with and without J_2; upward-triangles are the primary objects, and downward are the secondaries. The high obliquity of some of the close orbits with J_2 is due to them being captured into Cassini state 2 (see text).

Q	Spin	J_2	m_1/m_2	k_L	ρ	% Circ.	% Dest.	$\lvert H'_{tide}\rvert$	$\lvert H'_{circ}\rvert$
10	fast	0	1	rubble	0.5	56%	3%	1.28	0.620
10	fast	0	1	rubble	1.0	48%	1%	1.19	0.550
10	fast	0	1	solid	0.5	38%	2%	1.05	0.435
10	fast	0	1	solid	1.0	39%	1%	1.03	0.426
100	fast	0	1	rubble	0.5	48%	2%	1.07	0.534
100	fast	0	1	rubble	1.0	42%	1%	0.98	0.488
100	fast	0	1	solid	0.5	29%	11%	0.92	0.380
100	fast	0	1	solid	1.0	34%	5%	0.94	0.324
100	fast	0	10	rubble	0.5	43%	2%	1.05	0.437
100	fast	0	10	rubble	1.0	40%	1%	1.04	0.359
100	fast	0	10	solid	0.5	23%	15%	0.84	0.326
100	fast	0	10	solid	1.0	25%	9%	0.87	0.264
100	fast	0.1	1	rubble	0.5	38%	2%	1.12	0.005
100	fast	0.1	1	rubble	1.0	36%	0%	1.11	0.005
100	fast	0.1	1	solid	0.5	24%	8%	0.90	0.012
100	fast	0.1	1	solid	1.0	28%	5%	0.84	0.001
100	fast	0.01	1	rubble	0.5	36%	1%	1.09	0.028
100	fast	0.01	1	rubble	1.0	34%	1%	1.04	0.054
100	fast	0.01	1	solid	0.5	25%	9%	0.87	0.014
100	fast	0.01	1	solid	1.0	26%	5%	0.90	0.014
100	slow	0	1	rubble	0.5	44%	2%	1.13	0.524
100	slow	0	1	rubble	1.0	43%	1%	1.00	0.514
100	slow	0	1	solid	0.5	27%	14%	0.88	0.364
100	slow	0	1	solid	1.0	33%	5%	0.94	0.362

Table 4.1: Summary of KCTF simulation results: % Circ. are the fraction of surviving orbits with $e < 10^{-4}$, % Dest. are the fraction of initial orbits destroyed over the simulation, and $|H'_{tide}|$ and $|H'_{circ}|$ are as defined in the text.

Designation	Name	a (% r_{Hill})	e	I (deg)	GM (km^3/s^2)	H'
79360	Sila	0.35	0.02	123.1	0.72	-0.32
2001 QC_{298}		0.50	0.34	73.5	0.79	+0.19
66652	Borasisi	0.91	0.47	49.4	0.23	+0.55
42355	Typhon	1.15	0.53	50.5	0.06	+0.58
2004 PB_{108}		1.48	0.44	83.2	0.63	+0.13
2001 XR_{254}		1.70	0.56	21.1	0.27	+1.01
148780	Altjira	1.83	0.34	25.4	0.27	+1.15
275809		1.88	0.42	161.0	0.27	-1.18
26308		2.42	0.47	75.4	0.46	+0.35
2003 QY_{90}		3.19	0.66	51.4	0.03	+0.84
58534	Logos	3.25	0.55	74.2	0.03	+0.41
88611	Teharonhiawako	5.82	0.25	127.7	0.16	-1.43

Table 4.2: H' for observed systems with fully-constrained orbits. I is the angle between the heliocentric and mutual orbital planes, and GM is the system mass. Orbits are from Grundy *et al.* (2011), Parker *et al.* (2011), Sheppard *et al.* (2012) and references therein.

Designation	Name	a (% r_{Hill})	e	GM (km^3/s^2)
120347	Salacia	0.23	0.01	30.28
79360	Sila	0.35	0.02	0.72
90482	Orcus	0.42	0.00	42.40
134860		0.53	0.09	0.14
123509		0.66	0.01	0.07
65489	Ceto	0.71	0.01	0.37

Table 4.3: Observed TNB systems with near-circular orbits. GM is the system mass. Orbits are from Brown *et al.* (2010), Grundy *et al.* (2011), Stansberry *et al.* (2012) and references therein.

Chapter 5

POST-CAPTURE EVOLUTION OF POTENTIALLY HABITABLE EXOMOONS

5.1 Motivation

Exomoons, the satellites of extrasolar planets, have been often featured in fiction as habitable locations. There is no deficit of known giant planets; Exoplanet.org (Wright *et al.*, 2011) lists approximately 40 giant exoplanets (8% of total) within 20% of the equilibrium temperature of Earth, as are 30 (3%) of the *Kepler* planet candidates released in February 2011 (Borucki *et al.*, 2011). Though these observations are preliminary, they do show that habitable-zone giant planets not only exist, but are common. Once a giant planet is known to be in a habitable zone, variations in its orbit, such as Transit Timing Variation (TTV; Sartoretti and Schneider, 1999) and Transit Duration Variation (TDV; Kipping, 2009), photometry (Szabó *et al.*, 2006), or gravitational microlensing (Liebig and Wambsganss, 2010), allow the indirect detection of satellites. Thus, if potentially habitable exomoons exist around transiting giant planets, they may be detected at the same (or even greater) rate as solitary habitable terrestrial planets. As yet, no exomoons have been detected, but the wealth of transit data from the Kepler mission should begin to fill this gap.

Despite the existence of giant planets in stellar habitable zones, it is far from certain how they arrived there. Current giant-planet formation models assume that they are created at distances beyond the stability point of ice (e.g. Lissauer, 1987; Boss, 1997), which implies conditions not suitable to surface habitability. Disk migration can bring giant planets close to the star (Ward, 1997), but generally has a stopping point far too close to the star to be habitable (thus producing "Hot Jupiters"). The

host planets of potentially habitable exomoons therefore likely arrived at their final orbit through late-stage migration, driven either by planetesimals (Kirsh *et al.*, 2009) or other giant planets (Weidenschilling and Marzari, 1996).

In the process of migrating, the satellite systems of these giant planet may have close encounters with terrestrial planets or planetesimals, causing them to be disrupted or replaced. If either the Jovian or Saturnian systems were transported to 1 AU around a solar mass-star, both Callisto and Titan would be at 18% of their planet's Hill radii, thus implying that all the major satellites of the two planets would be on stable orbits. However, a close encounter could either excite their orbits to high eccentricity (thus requiring tidal recircularization), or could result in the capture of a much larger terrestrial satellite. Neptune appears have to experienced this process during its migration through the proto-Kuiper Belt, loosing any original major satellites, while gaining Triton in an inclined, retrograde orbit. This was possibly due to a momentum-exchange reaction that ejected the binary companion of Triton (Agnor and Hamilton, 2006), though other scenarios are possible (at reduced probability). Any capture process, though, will tend to produce very loosely-bound initial orbits, with only a small delta-v to escape velocity at periapse. Therefore, some method must be used to determine the long-term evolution and stability (or lack thereof) for these orbits. Here we use a full KCTF (Kozai Cycle and Tidal Friction) model to find the survival probability for a range of physical conditions and the detectability of the resulting system.

As shown by Donnison (2010) and Sato and Asada (2010), there are a range of stable orbits for Earth-mass planets around giant planets. However, both of those models test only the stability of the orbit, rather than any evolution due to tidal effects. On inclined exomoon orbits, the effects of stellar torques on the orbit can, through initiating Kozai cycles, dramatically accelerate the rate of tidal decay, orbit

circularization, and spin-orbit synchronization. As we will show, this process can allow even very loose, inclined capture orbits to stabilize to tight, circular orbits. Thus, even marginal dynamical captures of former terrestrial planets can produce stable exomoons.

5.2 KCTF Model

In order to understand how exomoon orbits may evolve after being captured, we created a numerical Kozai Cycle and Tidal Friction (KCTF) model. Kozai cycles in this context are the secular oscillations in eccentricity and inclination of the exomoon's orbit caused by stellar torques (Kozai, 1962). In isolation, these oscillations preserve the semimajor axis of the orbit and the quantity $H_k = cos(I) \times \sqrt{1 - e^2}$, where I is the inclination of the exomoon's orbit relative to the planet's stellarcentric orbit, and e is the eccentricity of the exomoon's orbit. In the scenarios simulated, these cycles can initially be as fast as just a few years (see Figure 5.1), causing very rapid evolution of the exomoon's orbit. Since all the initial orbits for this study were highly elliptical, only very low initial inclinations (within about 15° of coplanar) produced values of H_k sufficiently low that Kozai cycles did not occur.

Because the Kozai oscillations from the star attempt to preserve H_k, a drop in the inclination of the orbit can cause the eccentricity to become very high. As the eccentricity of the orbit increases, the periapse of the exomoon's orbit becomes much closer to the planet. Tidal forces become much stronger at these close distances (going as a^{-8} in this model), and so a close periapse due to eccentricity causes the orbit to shrink and thus decay further. This sets up a positive feedback loop, which progressively shrinks and circularizes the orbit. The stair-step semimajor axis decay in Figure 5.1 happens because the obit is initially only decaying at high eccentricities; once the apoapse is close enough to also experience tidal forces, the oscillations stop.

The result is to cause semimajor axis decay and circularization much faster than if the star were not exciting eccentricity. In addition, since the high eccentricity part of the Kozai cycles are at low inclinations, orbits are preferentially frozen near the plane of the stellarcentric orbit.

To simulate this process, we used a KCTF model based on that of Eggleton and Kiseleva-Eggleton (2001), which allows the direct integration of the exomoon orbit's specific angular momentum vector $\mathbf{h}$ and Laplace-Runge-Lenz eccentricity vector $\mathbf{e}$, as well as the spin vectors of the planet and satellite. The tidal properties of the giant planets were based on those presented in Fabrycky and Tremaine (2007) for a Jupiter-mass planet. The tidal properties of the exomoons used the formulation of Ragozzine (2009), along with his addition of solid-body quadrapole gravity. To integrate the system of equations, we used the Burlisch-Stoer method with vector-rational interpolation (Sweatman, 1998) and error control based on the algorithm given in Press *et al.* (2007), with a per-timestep tolerance of 10^{-10}.

This model does not include any dynamical effects from objects external to the exomoon-exoplanet system other than the star itself. In addition, we assumed that the planet did not migrate over the course of the simulation. If it were to migrate, the effect would be to shrink the Hill radius of the planet and shorten the period of the Kozai cycles. The smaller Hill radii would allow more captured satellites to escape, while on the other hand, the faster Kozai cycles would decrease the decay timescale. Thus, if this model works fast enough for a static case, it should also be applicable to a slowly migrating planet.

5.3 Monte Carlo Simulations

To find in what conditions a captured exomoon may survive, we generated 18 sets of synthetic Star-Planet-Moon systems and performed KCTF simulations on them.

Each set contained 1000 synthetic systems, with common masses for all objects, and randomized initial exomoon orbits and spin states. To simulate a loose capture, the initial exomoon orbits all had apoapses beyond 80% of the planet's Hill radius, and eccentricities greater than 0.85. This is most consistent with a low mass ratio momentum-exchange capture (Funato *et al.*, 2004), but generally similar to any low delta-v, non-disruptive capture (or eccentricity excitation due to a close encounter). Again consistent with a capture, both the satellite's initial orbital plane and spin vector were initially pointed at random directions on the sky. This means an approximate equipartition between prograde and retrograde initial orbits and between prograde and retrograde initial spin states for the satellite. The planets had a random obliquity less than 5° from their stellarcentric orbit. Each planet-moon system was at a stellarcentric distance such that the equilibrium temperature was equal to Earth. The stars and stellarcentric orbits used were the Sun (G2) at 1.0 AU, a main-sequence F0 (1.7 M_{Sun}) at 2.1 AU, and a main-sequence M0 (0.47 M_{Sun}) at 0.28 AU. The planets we assumed to have a mass equal to either Jupiter or Neptune, using the tidal parameters given in Fabrycky and Tremaine (2007), though nearly all dissipation was in the exomoon. The simulated exomoons had the mass of either Earth, Mars, or Titan (with Mars uncompressed density), using a tidal Q of 100, modulus of rigidity of $3 \times 10^{10} N/m^2$ (Gladman *et al.*, 1996), and J_2 of 0.001. The initial rotational periods of the planet and satellite were varied randomly between 0.1 and 48 hours. The simulations were run until they reached either 10^9 years or an eccentricity below 10^{-5}. However, the simulations were terminated early if the periapse went below the Roche limit (thus potentially causing breakup of the exomoon) or the apoapse exceeded the Hill radius (allowing the exomoon to become unbound). It is possible that the exomoon could have survived and remained bound to the planet in these scenarios, but that is beyond the fidelity of these simulations.

To estimate the detectability of the resulting systems, we calculated root-mean-squared Transit Timing Variations (TTVs) and Duration Variations (TDVs) for each simulation. The TTV and TDV are due to the orbit of the exomoon causing the exoplanet to begin the transit either sooner or later than the barycenter of the planet-moon system. These effects are maximized for low mass ratios (e.g. Earth mass exomoon around a Neptune-mass planet) and longer period exomoon orbits. Since the majority of resulting systems were low-inclination with respect to the stellarcentric orbit, we used the zero-inclination equations from Kipping (2009). Assuming zero-inclination maximizes the TTV and TDV, allowing an estimate of whether the system would be even detectable in the best case scenario.

5.4 Results and Discussion

The general result of the simulations is that loosely-captured exomoons around giant planets in habitable zones can survive to stabilize into long-lived orbits. Table 5.1 shows the fraction that stabilize for each mass/distance scenario. The exomoons stabilized much easier in the F0 case than the M0 case, with the solar-mass case in-between. The reason for this is readily apparent from the observation that while Hill radius scales linearly with distance from the star, the equilibrium temperature scales as the inverse square of distance. Thus, the super-solar mass star allows a much wider Hill radius at a habitable distance than for a planet of equal mass around a sub-solar mass star. This larger Hill radius provides the post-capture orbit much more room to move around, allowing longer period exomoons to stabilize. The truncation of periods greater than two days for the M0 case in Figure 5.3 is a clear result of this.

However, it also apparent from Figure 5.3 that the fast stellarcentric orbits of the M0 case allow for much more rapid exomoon circularization that for the larger stars. This clearly shows the effect of Kozai-pumped eccentricities accelerating tidal

decay, as otherwise the timescales would be independent of the distance from the star. The median circularization timescales for the M0 cases are of order 10^4 years, 10^5 years for the solar-mass star, and 10^6 years for the F0 star. All of these timescales are very short relative to the lifetime of the star, but 10^6 years may be long enough that the exomoon's orbit could be externally perturbed by a planet or planetesimal disk. On the other hand, as Figure 5.1 shows, the semimajor axis decay typically happens at least an order of magnitude faster than full circularization. Therefore, it is a reasonable assumption that nearly all these orbits would stabilize before any external perturbation would disrupt them.

To gauge the amount of tidal heating on the satellite, we estimated the amount of energy lost from the system from the difference in the initial and final orbits and spins. For the orbits, we first found the energy difference between the initial and final states. Then, we muliplied this an estimate of the fraction of energy that went into the satellite using the masses and tidal Q of the objects, $Q_{planet}M_{sat}/(Q_{planet}M_{sat} + Q_{sat}M_{planet})$. This term was usually near unity, as the planet was assumed to have a very large Q. We then estimated the change in rotational energy of the satellite, subtracted this from the change in orbital energy, and divided the result by the circularization time to produce a heating rate. The rate was dominated by the orbital term, as the initial rotation periods were not too different from the final orbital periods. Generally, this rate was higher per unit mass for larger satellites (which circularized faster) and closer orbits. For the Earth-mass/Jupiter-mass case, the median rates were 0.002 mW/kg around a F0 star, 0.02 mW/kg around a solar-mass star, and 0.5 mW/kg around a M0 star. These rates are higher than for either long-lived ($\approx 10^{-8}$ mW/kg; Desch *et al.*, 2009) or short-lived chondritic radioisotopes ($\approx 10^{-4}$ mW/kg; Schubert *et al.*, 2007). A more through analysis is beyond the

scope of this work, but these rates could create significant short-term heating on the exomoons.

Table 5.1 also shows the fates of the exomoon orbits which did not survive to circularize. The systems around the solar mass star were by far the most prone to separating beyond the Hill radius, with roughly equal impacts as separations. The M0 cases, on the other hand, actually impacted the planet in three-quarters of the cases, due to the very small Hill radius not allowing the periapse to shrink very far before impacting. A majority of F0 cases survived in all scenarios, with the large Hill radius allowing most orbits to circularize. Therefore, for a given capture rate, potentially habitable captured exomoons should be the most common around stars larger than a solar mass.

Figure 5.2 shows that the majority of the resulting orbits, especially around a Jupiter-mass planet, are nearly coplanar with the stellarcentric orbit. This is partially due to the assumed low obliquity of the planet aligning its gravitational quadrapole with the direction of the star. However, as shown by the high inclination of Triton (5.9 day period), an orbit does not need to be very large for this effect to be minimized. And indeed, the orbits around Neptune-mass planets show a much larger diversity of inclinations for periods less than two days, especially for Earth-mass satellites. Beyond this point, solar torques begin to dominate and force nearly all orbits coplanar. Since longer period orbits produce larger TTVs, it is therefore likely that the first exomoons detected will be coplanar with the stellarcentric orbit, and it will take much more observations to detect short-period, high-inclination exomoons.

Also congruent with Triton, Figure 5.2 shows that there is no real preference for either prograde or retrograde orbits. The secular perturbations of Kozai cycles do not allow the directionality of the orbit to change in all but the most inclined initial cases. Thus, each orbit preserves its original direction, evolving towards the plane

of the stellarcentric orbit. All of the final orbits are circular and have semimajor axes less than 28% of the planet-moon system's Hill radius, which as summarized by Donnison (2010), means that they should be stable over the lifetime of the star. Unfortunately, Kipping (2009) shows that TTV and TDV are both degenerate for prograde/retrograde inclinations, and so measuring the relative fractions may be very difficult. However, Simon *et al.* (2010) show that it may be possible to break this degeneracy with very precise measurements of the Rossiter-McLaughlin effect. Since secular perturbations cannot reverse the direction of a satellite's orbit, detection of a retrograde satellite around an exoplanet would be confirmation that this capture process occurred.

The median TTV and TDV for each simulation set are given in Table 5.2. The TTV do vary over a large range, but the upper end of that range is just within the limits of detection for modern transit systems. The Kepler mission has a regular cadence of approximately every 30 minutes, and can run at a cadence of up to once per minute (Koch *et al.*, 2010). This appears sufficient to detect an Earth-mass exomoon in most cases, and just enough to detect a Mars-mass exomoon in the best cases. Larger stars offer wider orbits (and thus stronger TTVs), but much more infrequent transits. Solar mass to early K stars therefore seem to offer a good balance between TTV strength and transit frequency.

The Transit Duration Variation (TDV) introduced by Kipping (2009) allows the unambiguous detection of an exomoon from transits alone. For the systems described in that work, the TDV was of similar duration to the TTV. However, we find that the lower planetary masses and much wider stellarcentric orbits of our study result in relatively weak TDVs for nearly all cases. Thus, it is unlikely that a potentially habitable exomoon will be detected by TDV alone; TDV could, though, allow for follow-up transit observations to confirm the existence of a TTV-detected exomoon.

These results compare well with previous estimates, though both of those simulations assumed much wider orbits than were usually produced by the KCTF model. The consequence of this is both reduce the TDV signal relative to that assumed by Kipping (2009) and the photometric signal of Szabó *et al.* (2006). On the other hand, Table 5.2 shows that even with these closer orbits, some exomoons are still within the range of detectability. The combination of TTV and TDV may offer a stronger detection signal than photometry for these orbits, though both could detect some of the orbits produced.

5.5 Conclusions

Several general conclusions can therefore be drawn from our simulations:

1. Loosely-captured exomoons around giant planets in habitable zones can survive to stabilize into long-lived orbits.

2. The timescale for them to stabilize is enhanced by Kozai torques, and is generally less than a few million years.

3. Most of the surviving orbits are close to the plane of the exoplanet's orbit, but show no prograde/retrograde preference.

4. Some of the resulting orbits should be currently detectable (especially for Earth-mass satellites), with the transit timing variation much stronger than the duration variation.

5. The most promising targets for detecting potentially habitable exomoons by TTV appear to be Neptune-mass exoplanets orbiting stars of solar mass or slightly below.

5.6 Acknowledgments

Special thanks to Travis Barman for donating the approximately 5000 CPU hours it took to complete this project.

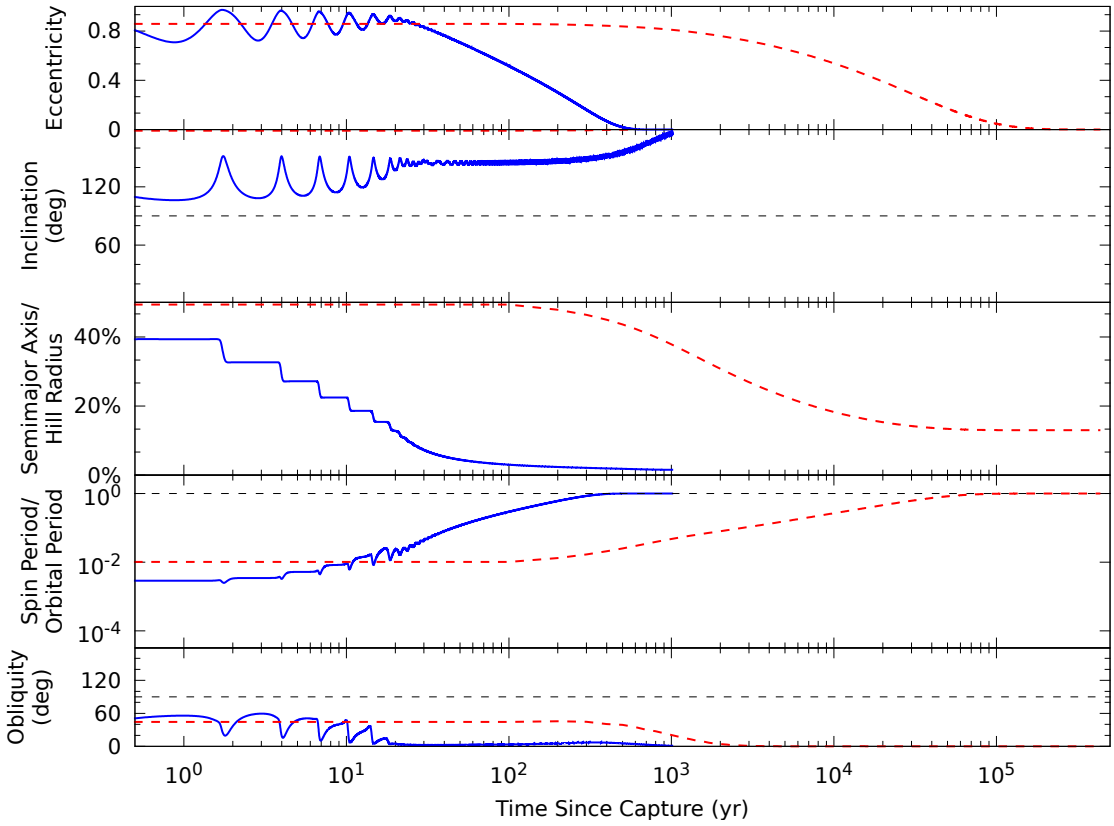

Figure 5.1: Post-capture spin-orbit evolution of two exomoons; the solid line shows a Kozai-enhanced decay, while the dashed line shows a non-Kozai decay.

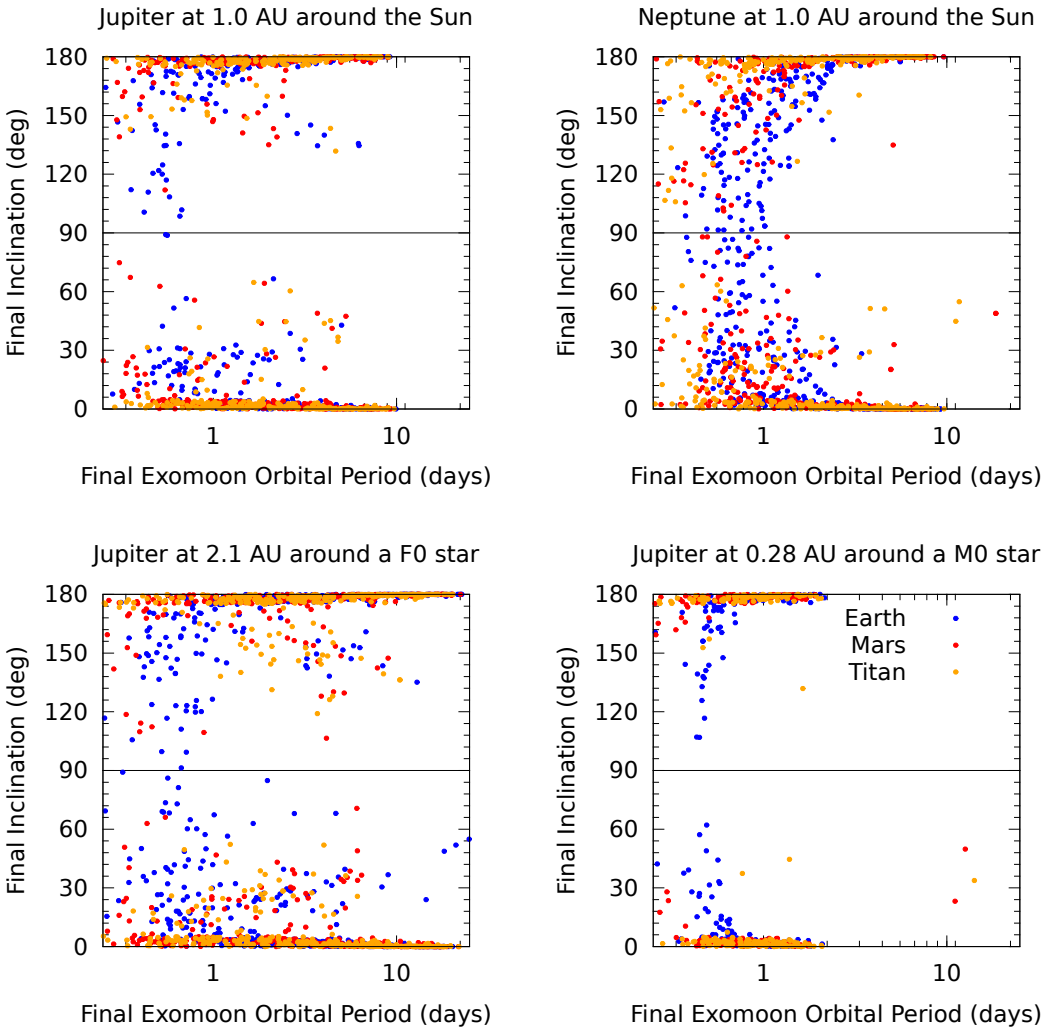

Figure 5.2: Post-evolution orbital period and inclination distribution; most orbits are coplanar with the planet's orbit, with no pro/retrograde preference.

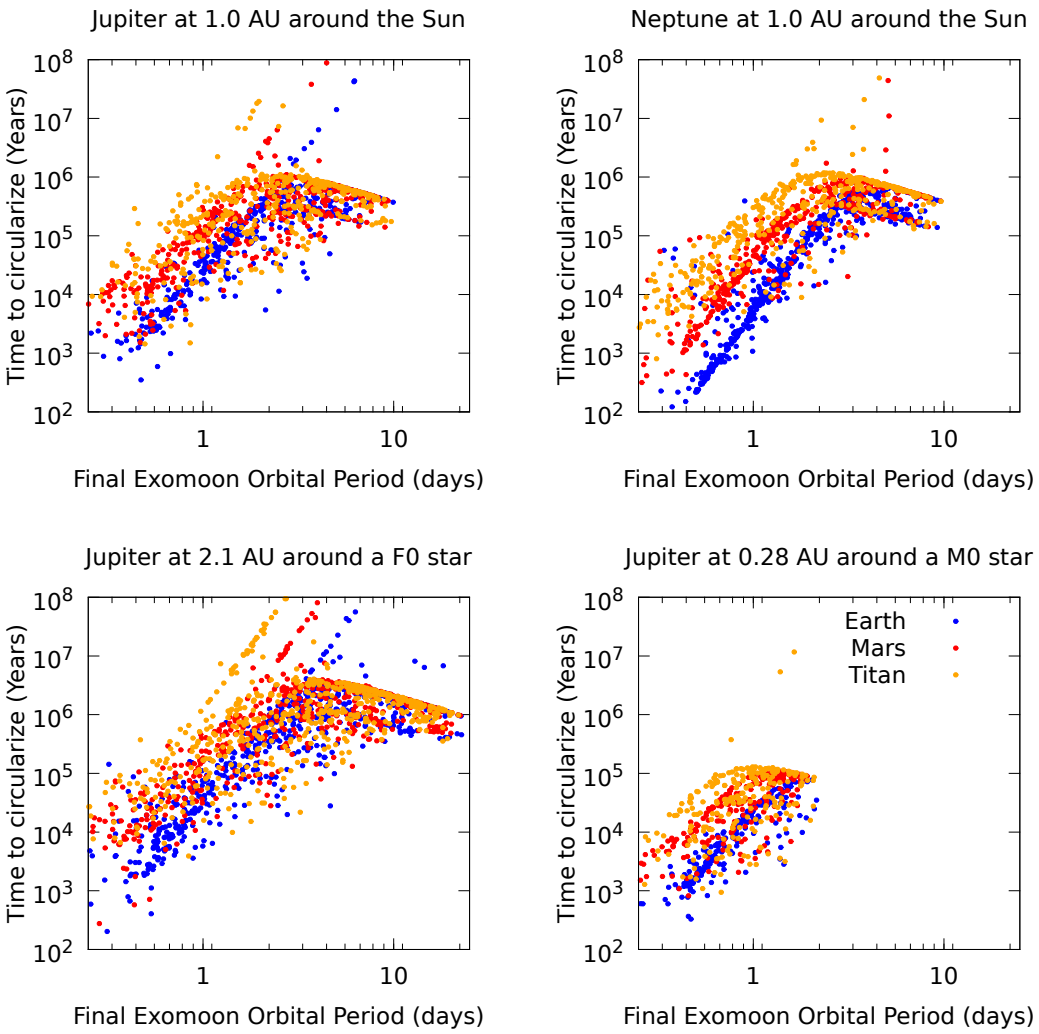

Figure 5.3: Post-capture circularization timescales; note that nearly all are below a few million years, and timescales decrease with stellar mass.

Star	Planet	Moon	Survived	Retrograde	Separated	Impacted
Sun	Jupiter	Earth	43%	52%	21%	35%
		Mars	44%	45%	18%	37%
		Titan	42%	47%	21%	36%
	Neptune	Earth	52%	44%	17%	30%
		Mars	44%	45%	18%	36%
		Titan	45%	47%	19%	35%
F0	Jupiter	Earth	65%	47%	3%	31%
		Mars	59%	46%	4%	35%
		Titan	61%	48%	3%	34%
	Neptune	Earth	77%	44%	4%	18%
		Mars	67%	44%	4%	28%
		Titan	61%	50%	4%	33%
M0	Jupiter	Earth	23%	50%	2%	74%
		Mars	23%	51%	3%	73%
		Titan	23%	44%	2%	74%
	Neptune	Earth	24%	50%	1%	73%
		Mars	25%	52%	1%	73%
		Titan	22%	50%	3%	74%

Table 5.1: Relative fraction of end states for fully evolved exomoon systems.

Star	Planet	Moon	Period (d)	TTV (min)	TDV	edge-on (min)
Sun	Jupiter	Earth	2.17	5.44	0.114%	0.93
		Mars	2.34	0.59	0.012%	0.10
		Titan	2.52	0.12	0.002%	0.02
	Neptune	Earth	1.65	36.69	0.835%	6.41
		Mars	1.89	4.11	0.089%	0.69
		Titan	2.16	0.86	0.018%	0.14
F0	Jupiter	Earth	3.68	11.33	0.111%	1.45
		Mars	4.26	1.22	0.011%	0.15
		Titan	4.14	0.26	0.002%	0.03
	Neptune	Earth	2.38	75.70	0.860%	10.60
		Mars	3.79	8.51	0.083%	1.03
		Titan	3.50	1.78	0.018%	0.22
M0	Jupiter	Earth	0.94	1.63	0.122%	0.54
		Mars	1.00	0.18	0.013%	0.06
		Titan	1.00	0.04	0.003%	0.01
	Neptune	Earth	0.85	10.97	0.836%	3.36
		Mars	0.79	1.22	0.098%	0.39
		Titan	0.83	0.26	0.020%	0.08

Table 5.2: Median Exomoon orbital period, Transit Timing Variation (TTV), and Transit Duration Variation (TDV) for full-evolved exomoon systems.

Chapter 6

CONCLUSION

This dissertation covers four distinct but interrelated topics. We have shown that orbital mechanics can be a complex and chaotic process, often only stabilizing after millions of orbits. Through this chaos, satellites and binaries can be left in otherwise unattainable configurations. We also showed that even the smallest particles of dust can have significant and observable effects on the surfaces of outer solar system objects. The trajectories of this dust can be complex and dominated by gravitational focusing or solar radiation pressure, both of which can determine the location and energy of the dust's impact onto larger bodies.

In Chapter 2, we showed that dust impacts onto the surfaces of giant planet icy satellites and Kuiper Belt objects can crystallize ice on their surfaces. Since the amount of annealing is determined by the kinetic energy of the impact, gravitationally focused interplanetary dust particles (IDPs) dominate the annealing process. The most amount of annealing is therefore on the innermost regular satellites of the giant planets with less annealing on the outer satellites and Kuiper Belt objects.

In Chapter 3, showed that dust from the small satellites of Pluto can impact impact on to either Pluto or Charon. Which of the two it hits is mostly a function of the ejection velocity, with low velocity ejecta being swept up by Charon, and high velocity ejecta by Pluto. The dust typically impacts or is ejected within 100 days, and only the lowest-velocity ejecta is stable for much longer than this. The dust does not impact uniformly on the surface of Pluto and Charon, but rather at particular longitudes as a fucntion of ejection velocity. The observed albedo distribution of Pluto is best fit to the higher-velocity ejecta.

In Chapter 4, we showed that the orbits of trans-neptunian binary (TNB) systems can be transformed by solar perturbations. The weak gravitational torques on the binary system from the Sun can cause wide and inclined TNB systems to become very eccentric, thus triggering runway tidal decay to close circular orbits. These close circular orbits are very stable and mostly beyond the ability of current telescopes to resolve. A fraction of orbits do not decay fully, but instead reach slightly wider, moderate eccentricity orbits where the perturbations from their shapes cancel out the solar perturbations. In addition, we introduced a stability parameter to quickly check if a given orbit is stable to these perturbations.

Finally, in Chapter 5, we modeled the orbital evolution of an Earth-like planet captured as an exomoon, a satellite of an exosolar giant planet. The same perturbations as in Chapter 4 come in to play, except from the host star of the giant planet. These perturbations cause all the captured exomoons to either impact the giant planet or stabilize to circular orbits with 0.5-5 day periods. On average, about half of the captured exomoons survived when the giant was presumed to be in the habitable zone of a solar-type star. More survived in the habitable zone of a F0 star, and fewer for the habitable zone of an M0 star. Some of the exomoons are potentially detectable from their effect on transit timing, especially the largest moons captured around the smallest giants.

6.1 Future Work

There is great potential for future investigations in all four of these topics. Chapter 2 could benefit from more detailed studies of the micrometeorite impact process and the subsequent diffusion of heat. A smooth-particle hydrodynamic code, modified to account for the amorphous-crystalline phase change, would be appropriate for these simulations. In addition, a more through estimation of the high-energy ra-

diation amorphization rate would allow for much more accurate predictions of the fraction of crystalline ice to be expected on the surfaces of icy satellites and TNOs. Better knowledge of the relative effects of each class of radiation (UV, Gamma/X-ray, solar proton/electron, and heavy ion) would help tremendously, especially as most laboratory studies focus on only one radiation source.

There are some potential observations which could test the micrometeorite annealing process. Unlike most endogenic processes, micrometeorite annealing is a strong function of distance to the host planet, due to gravitational focusing. Thus, the ideal observational test would be two satellites which are otherwise similar but experience very different gravitational focusing. The second- and third-largest satellites of Neptune, Nereid and Proteus, appear to fit these conditions. They are approximately the same size and density (Karkoschka, 2003), and are small enough that they likely do not have endogenic processes (Voyager 2 showed both to be irregular). Previous spectra of Nereid have been able to detect water ice (Brown *et al.*, 1998). Since both objects are quite dim and Proteus is very close to Neptune, obtaining near-infrared spectra of their surfaces with enough resolution to measure the crystalline fraction will be difficult, but rewarding.

Future work for Chapter 3 would likely be focused on better predicting what surface effects (if any) would be detectable by the *New Horizons* spacecraft during its encounter with Pluto and Charon. This would include an accounting of Pluto's atmosphere and its effect on the impact locations and velocities of the micrometeorites. In addition, a useful comparison would be between the expected accumulation rates and the amount of seasonally-transported volatiles on the surface of Pluto. Determining the real rates of accumulation would also require a more rigorous estimate of the impact rate and size frequency distribution on the small satellites of Pluto. This

in turn could be used to predict the expected cratering on the surfaces of the small satellites.

Chapter 4 raises many questions about binary and multiple TNO systems. Most of these issues are not easily addressed with the limited KCTF model used in Chapter 4, and instead would be much better addressed by more complex model. The ability to model shapes that are not axisymmetric would be very useful; many of the end states of the simulations were controlled by shape, but the model was insufficient to correctly determine those states. The next complication would be the ability to model triple and higher systems. At least one such system has been identified (1999 TC_{36}, Benecchi *et al.*, 2010) and more are likely to as telescope angular resolutions continue to improve. Finally, the ability to examine different tidal models be useful to check the sensitivity of the assumed physical parameters to the final results of the simulations.

With this more complex model, the rotational states of close-in trans-neptunian binaries could be investigated. This may offer a pathway to produce contact binaries through tidal decay, something the KCTF model was never able to do. The formation and subsequent tidal evolution of the triple 1999 TC_{36} could be modeled, and the potential configurations of currently unresolved triples predicted. Both of these would offer both predictions for future high-angular resolution astrometry and help to constrain the true size-frequency distribution of TNOs, de-bias for multiple systems.

Finally, Chapter 5 offers potentially the most future investigation. That study was focused on the evolution of large exomoons after capture, and did investigate at all the capture process itself, nor any of the planetary migration before the capture. These are such complex problems that a through examination either of those events could constitute an entire dissertation.

The capture process is a more discrete problem, and could be approached with a large number of n-body simulations. The two dynamical methods of capture would be either the splitting of binary system (e.g. the Earth and Moon) or a solitary interloper which exchanges momentum with an existing smaller satellite. Both of these scenarios require special circumstances, and examining the statistics of many simulations will allow an estimation of just how special those circumstances are. Once these capture orbits are known, they can be fed back into the already-developed KCTF model and stabilized, thus proving an estimate of the number of large exomoons per close encounter.

Estimating the number and relative velocity of the close encounter is a more difficult problem, but also a much deeper one. The NASA *Kepler* mission has shown that tight-packed planetary systems with multiple giant planets are common, and approximately 1% of systems have a giant in or near the star's habitable zone (Batalha *et al.*, 2013). Explaining the evolution of these close-in giants would be beyond the scope of an exomoon investigation, but the number and relative velocity of planetary close encounters would naturally fall out of planetary migration simulations. Thus, this would be best done in collaboration with a team that is already studying migration and could provide information on the close encounters their simulations produce. A realistic estimate of close encounter frequency would then allow a true prediction of the frequency of large, potentially detectable exomoons.

Agnor, C. B. and D. P. Hamilton, "Neptune's capture of its moon Triton in a binary-planet gravitational encounter", Nature **441**, 192–194 (2006).

Andersson, O. and H. Suga, "Thermal conductivity of amorphous ices", Phys. Rev. B **65**, 14, 140201 (2002).

Baragiola, R. A., "Water ice on outer solar system surfaces: Basic properties and radiation effects", Planet. Space Sci. **51**, 953–961 (2003).

Barkume, K. M., M. E. Brown and E. L. Schaller, "Near-Infrared Spectra of Centaurs and Kuiper Belt Objects", AJ **135**, 55–67 (2008).

Barucci, M. A., F. Merlin, A. Guilbert, C. de Bergh, A. Alvarez-Candal, O. Hainaut, A. Doressoundiram, C. Dumas, T. Owen and A. Coradini, "Surface composition and temperature of the TNO Orcus", A&A **479**, L13–L16 (2008).

Batalha, N. M., J. F. Rowe, S. T. Bryson, T. Barclay and et al, "Planetary Candidates Observed by Kepler. III. Analysis of the First 16 Months of Data", ApJS **204**, 24 (2013).

Bauer, J. M., T. L. Roush, T. R. Geballe, K. J. Meech, T. C. Owen, W. D. Vacca, J. T. Rayner and K. T. C. Jim, "The Near Infrared Spectrum of Miranda: Evidence of Crystalline Water Ice", Icarus **158**, 178–190 (2002).

Benecchi, S. D., K. S. Noll, W. M. Grundy and H. F. Levison, "(47171) 1999 TC36, A transneptunian triple", Icarus **207**, 978–991 (2010).

Bills, B. G. and F. Nimmo, "Forced obliquity and moments of inertia of Titan", Icarus **196**, 293–297 (2008).

Borucki, W. J., D. G. Koch, G. Basri, N. Batalha, T. M. Brown, S. T. Bryson, D. Caldwell, J. Christensen-Dalsgaard, W. D. Cochran, E. DeVore, E. W. Dunham, T. N. Gautier, III, J. C. Geary, R. Gilliland, A. Gould, S. B. Howell, J. M. Jenkins, D. W. Latham, J. J. Lissauer, G. W. Marcy, J. Rowe, D. Sasselov, A. Boss, D. Charbonneau, D. Ciardi, L. Doyle, A. K. Dupree, E. B. Ford, J. Fortney, M. J. Holman, S. Seager, J. H. Steffen, J. Tarter, W. F. Welsh, C. Allen, L. A. Buchhave, J. L. Christiansen, B. D. Clarke, J.-M. Désert, M. Endl, D. Fabrycky, F. Fressin, M. Haas, E. Horch, A. Howard, H. Isaacson, H. Kjeldsen, J. Kolodziejczak, C. Kulesa, J. Li, P. Machalek, D. McCarthy, P. MacQueen, S. Meibom, T. Miquel, A. Prsa, S. N. Quinn, E. V. Quintana, D. Ragozzine, W. Sherry, A. Shporer, P. Tenenbaum, G. Torres, J. D. Twicken, J. Van Cleve and L. Walkowicz, "Characteristics of planetary candidates observed by Kepler, II: Analysis of the first four months of data", ArXiv e-prints (2011).

Boss, A. P., "Giant planet formation by gravitational instability.", Science **276**, 1836–1839 (1997).

Brown, M. E., C. D. Koresko and G. A. Blake, "Detection of Water Ice on Nereid", ApJ **508**, L175–L176 (1998).

Brown, M. E., D. Ragozzine, J. Stansberry and W. C. Fraser, "The Size, Density, and Formation of the Orcus-Vanth System in the Kuiper Belt", AJ **139**, 2700–2705 (2010).

Brown, R. H., D. P. Cruikshank, Y. Pendleton and G. J. Veeder, "NOTE: Water Ice on Nereid", Icarus **139**, 374–378 (1999).

Buie, M. W., W. M. Grundy, E. F. Young, L. A. Young and S. A. Stern, "Pluto and Charon with the Hubble Space Telescope. II. Resolving Changes on Pluto's Surface and a Map for Charon", AJ **139**, 1128–1143 (2010).

Burns, J. A., "Orbital evolution", in "IAU Colloq. 28: Planetary Satellites", edited by J. A. Burns, pp. 113–156 (1977).

Burns, J. A., M. R. Showalter, D. P. Hamilton, P. D. Nicholson, I. de Pater, M. E. Ockert-Bell and P. C. Thomas, "The Formation of Jupiter's Faint Rings", Science **284**, 1146 (1999).

Canup, R. M., "A Giant Impact Origin of Pluto-Charon", Science **307**, 546–550 (2005).

Cash, J. R., "A variable step runge-kutta-nystrom integrator for reversible systems of second order initial value problems", SIAM J. Sci. Comput. **26**, 3, 963–978, URL `http://dx.doi.org/10.1137/S030601727` (2005).

Christy, J. W., "The discovery of Charon", in "Pluto and Charon", edited by Stern, S. A., Tholen, D. J., pp. xvii–xxi (University of Arizona Press, 1997).

Colombo, G., D. A. Lautman and I. I. Shapiro, "The Earth's Dust Belt: Fact or Fiction?, 2, Gravitational Focusing and Jacobi Capture", J. Geophys. Res. **71**, 5705 (1966).

Cook, J. C., S. J. Desch, T. L. Roush, C. A. Trujillo and T. R. Geballe, "Near-Infrared Spectroscopy of Charon: Possible Evidence for Cryovolcanism on Kuiper Belt Objects", ApJ **663**, 1406–1419 (2007).

Cooper, B. L., J. W. Salisbury, R. M. Killen and A. E. Potter, "Midinfrared spectral features of rocks and their powders", Journal of Geophysical Research (Planets) **107**, 5017 (2002).

Davies, J., *Beyond Pluto* (Cambridge UP, 2001).

Desch, S. J., J. C. Cook, T. Doggett and S. B. Porter, "Thermal evolution of kuiper belt objects, with implications for cryovolcanism", Icarus **202**, 2, 694 – 714 (2009).

Divine, N., "Five populations of interplanetary meteoroids", J. Geophys. Res. **98**, 17029–17048 (1993).

Donnison, J. R., "The Hill stability of the possible moons of extrasolar planets", MNRAS **406**, 1918–1934 (2010).

Dumas, C., B. A. Smith and R. J. Terrile, "Hubble Space Telescope NICMOS Multiband Photometry of Proteus and Puck", AJ **126**, 1080–1085 (2003).

Eggleton, P. P. and L. Kiseleva-Eggleton, "Orbital Evolution in Binary and Triple Stars, with an Application to SS Lacertae", ApJ **562**, 1012–1030 (2001).

Eggleton, P. P. and L. Kisseleva-Eggleton, "A Mechanism for Producing Short-Period Binaries", Ap&SS **304**, 75–79 (2006).

Elliot, J., E. Adams, S. D. Kern, L. H. Wasserman, E. I. Chiang, J. R. Lovering, M. W. Buie, R. L. Millis, S. N. Hylton, K. B. Clancy, D. E. Trilling, L. E. Hutchison and B. G. Marsden, "2001 PK47, 2004 PB108, 2004 PA112, 2004 VT75", Minor Planet Electronic Circulars p. 56 (2005).

Fabrycky, D. and S. Tremaine, "Shrinking Binary and Planetary Orbits by Kozai Cycles with Tidal Friction", ApJ **669**, 1298–1315 (2007).

Fabrycky, D. C., E. T. Johnson and J. Goodman, "Cassini States with Dissipation: Why Obliquity Tides Cannot Inflate Hot Jupiters", ApJ **665**, 754–766 (2007).

Fang, J., J.-L. Margot, M. Brozovic, M. C. Nolan, L. A. M. Benner and P. A. Taylor, "Orbits of Near-Earth Asteroid Triples 2001 SN263 and 1994 CC: Properties, Origin, and Evolution", AJ **141**, 154 (2011).

Filacchione, G., F. Capaccioni, T. B. McCord, A. Coradini, P. Cerroni, G. Bellucci, F. Tosi, E. D'Aversa, V. Formisano, R. H. Brown, K. H. Baines, J. P. Bibring, B. J. Buratti, R. N. Clark, M. Combes, D. P. Cruikshank, P. Drossart, R. Jaumann, Y. Langevin, D. L. Matson, V. Mennella, R. M. Nelson, P. D. Nicholson, B. Sicardy, C. Sotin, G. Hansen, K. Hibbitts, M. Showalter and S. Newman, "Saturn's icy satellites investigated by Cassini-VIMS. I. Full-disk properties: 350-5100 nm reflectance spectra and phase curves", Icarus **186**, 259–290 (2007).

Funato, Y., J. Makino, P. Hut, E. Kokubo and D. Kinoshita, "The formation of Kuiper-belt binaries through exchange reactions", Nature **427**, 518–520 (2004).

Gladman, B., D. Dane Quinn, P. Nicholson and R. Rand, "Synchronous Locking of Tidally Evolving Satellites", Icarus **122**, 166–192 (1996).

Goldreich, P., Y. Lithwick and R. Sari, "Formation of Kuiper-belt binaries by dynamical friction and three-body encounters", Nature **420**, 643–646 (2002).

Goldreich, P. and R. Sari, "Tidal Evolution of Rubble Piles", ApJ **691**, 54–60 (2009).

Goldreich, P. and S. Soter, "Q in the Solar System", Icarus **5**, 375–389 (1966).

Grundy, W., S. Benecchi, D. Rabinowitz, S. Porter, L. Wasserman, B. Skiff, K. Noll, A. Verbiscer, M. Buie, S. Tourtellotte, D. Stephens and H. Levison, "Mutual events in the cold classical transneptunian binary system sila and nunam", Icarus **220**, 1, 74–83 (2012).

Grundy, W. M., M. W. Buie, J. A. Stansberry, J. R. Spencer and B. Schmitt, "Near-Infrared Spectra of Icy Outer Solar System Surfaces: Remote Determination of H_2O Ice Temperatures", Icarus **142**, 536–549 (1999).

Grundy, W. M., K. S. Noll, M. W. Buie, S. D. Benecchi, D. C. Stephens and H. F. Levison, "Mutual orbits and masses of six transneptunian binaries", Icarus **200**, 627–635 (2009).

Grundy, W. M., K. S. Noll, F. Nimmo, H. G. Roe, M. W. Buie, S. B. Porter, S. D. Benecchi, D. C. Stephens, H. F. Levison and J. A. Stansberry, "Five new and three improved mutual orbits of transneptunian binaries", Icarus **213**, 678–692 (2011).

Grundy, W. M., J. A. Stansberry, K. S. Noll, D. C. Stephens, D. E. Trilling, S. D. Kern, J. R. Spencer, D. P. Cruikshank and H. F. Levison, "The orbit, mass, size, albedo, and density of (65489) Ceto/Phorcys: A tidally-evolved binary Centaur", Icarus **191**, 286–297 (2007).

Grundy, W. M., L. A. Young, J. R. Spencer, R. E. Johnson, E. F. Young and M. W. Buie, "Distributions of H_2O and CO_2 ices on Ariel, Umbriel, Titania, and Oberon from IRTF/SpeX observations", Icarus **184**, 543–555 (2006).

Hansen, G. B. and T. B. McCord, "Amorphous and crystalline ice on the Galilean satellites: A balance between thermal and radiolytic processes", Journal of Geophysical Research (Planets) **109**, E18, 1012 (2004).

Hapke, B., "On the sputter alteration of regoliths of outer solar system bodies", Icarus **66**, 270–279 (1986).

Hartmann, W. K., "Impact experiments. I - Ejecta velocity distributions and related results from regolith targets", Icarus **63**, 69–98 (1985).

Horányi, M., V. Hoxie, D. James, A. Poppe, C. Bryant, B. Grogan, B. Lamprecht, J. Mack, F. Bagenal, S. Batiste, N. Bunch, T. Chanthawanich, F. Christensen, M. Colgan, T. Dunn, G. Drake, A. Fernandez, T. Finley, G. Holland, A. Jenkins, C. Krauss, E. Krauss, O. Krauss, M. Lankton, C. Mitchell, M. Neeland, T. Reese, K. Rash, G. Tate, C. Vaudrin and J. Westfall, "The Student Dust Counter on the New Horizons Mission", Space Science Reviews **140**, 387–402 (2008).

Humes, D. H., "Results of Pioneer 10 and 11 meteoroid experiments - Interplanetary and near-Saturn", J. Geophys. Res. **85**, 5841–5852 (1980).

Jacobson, R. A., J. E. Riedel and A. H. Taylor, "The orbits of Triton and Nereid from spacecraft and earthbased observations", A&A **247**, 565–575 (1991).

Jacobson, S. A. and D. J. Scheeres, "Dynamics of rotationally fissioned asteroids: Source of observed small asteroid systems", Icarus **214**, 161–178 (2011).

Jenniskens, P. and D. F. Blake, "Crystallization of Amorphous Water Ice in the Solar System", ApJ **473**, 1104 (1996).

Jewitt, D., J. Luu and B. G. Marsden, "1992 QB1", IAU Circ. **5611**, 1 (1992).

Jewitt, D. C. and J. Luu, "Crystalline water ice on the Kuiper belt object (50000) Quaoar", Nature **432**, 731–733 (2004).

Jones, H. S., *John Couch Adams and the Discovery of Neptune* (Cambridge UP, 1947).

Karkoschka, E., "Sizes, shapes, and albedos of the inner satellites of Neptune", Icarus **162**, 400–407 (2003).

Kipping, D. M., "Transit timing effects due to an exomoon", MNRAS **392**, 181–189 (2009).

Kirsh, D. R., M. Duncan, R. Brasser and H. F. Levison, "Simulations of planet migration driven by planetesimal scattering", Icarus **199**, 197–209 (2009).

Klinger, J., "Influence of a phase transition of ice on the heat and mass balance of comets", Science **209**, 271 (1980).

Knop, R. E., "Algorithm 381: random vectors uniform in solid angle", Commun. ACM **13**, 5, 326 (1970).

Koch, D. G., W. J. Borucki, G. Basri, N. M. Batalha, T. M. Brown, D. Caldwell, J. Christensen-Dalsgaard, W. D. Cochran, E. DeVore, E. W. Dunham, T. N. Gautier, J. C. Geary, R. L. Gilliland, A. Gould, J. Jenkins, Y. Kondo, D. W. Latham, J. J. Lissauer, G. Marcy, D. Monet, D. Sasselov, A. Boss, D. Brownlee, J. Caldwell, A. K. Dupree, S. B. Howell, H. Kjeldsen, S. Meibom, D. Morrison, T. Owen, H. Reitsema, J. Tarter, S. T. Bryson, J. L. Dotson, P. Gazis, M. R. Haas, J. Kolodziejczak, J. F. Rowe, J. E. Van Cleve, C. Allen, H. Chandrasekaran, B. D. Clarke, J. Li, E. V. Quintana, P. Tenenbaum, J. D. Twicken and H. Wu, "Kepler Mission Design, Realized Photometric Performance, and Early Science", ApJ **713**, L79–L86 (2010).

Kominami, J. D., J. Makino and H. Daisaka, "Binary Formation in Planetesimal Disks. I. Equal Mass Planetesimals", PASJ **63**, 1331–1344 (2011).

Kozai, Y., "Secular perturbations of asteroids with high inclination and eccentricity", AJ **67**, 591–598 (1962).

Krivov, A. V., M. Sremcevic, F. Spahn, V. V. Dikarev and K. V. Kholshevnikov, "Impact-generated dust clouds around planetary satellites: spherically symmetric case", Planet. Space Sci. **51**, 3, 251 – 269 (2003).

Lacerda, P., D. Jewitt and N. Peixinho, "High-Precision Photometry of Extreme Kbo 2003 EL_{61}", AJ **135**, 1749–1756 (2008).

Lee, E. A., S. A. Astakhov and D. Farrelly, "Production of trans-Neptunian binaries through chaos-assisted capture", MNRAS **379**, 229–246 (2007).

Leto, G. and G. A. Baratta, "Ly-alpha photon induced amorphization of Ic water ice at 16 Kelvin. Effects and quantitative comparison with ion irradiation", A&A **397**, 7–13 (2003).

Levy, D. H., *Clyde Tombaugh: Discoverer of Planet Pluto* (University of Arizona Press, Tucson, 1991).

Liebig, C. and J. Wambsganss, "Detectability of extrasolar moons as gravitational microlenses", A&A **520**, A68+ (2010).

Liou, J.-C. and H. A. Zook, "Signatures of the Giant Planets Imprinted on the Edgeworth-Kuiper Belt Dust Disk", AJ **118**, 580–590 (1999).

Lissauer, J. J., "Timescales for planetary accretion and the structure of the protoplanetary disk", Icarus **69**, 249–265 (1987).

Lissauer, J. J., D. Ragozzine, D. C. Fabrycky, J. H. Steffen, E. B. Ford, J. M. Jenkins, A. Shporer, M. J. Holman, J. F. Rowe, E. V. Quintana, N. M. Batalha, W. J. Borucki, S. T. Bryson, D. A. Caldwell, J. A. Carter, D. Ciardi, E. W. Dunham, J. J. Fortney, T. N. Gautier, III, S. B. Howell, D. G. Koch, D. W. Latham, G. W. Marcy, R. C. Morehead and D. Sasselov, "Architecture and Dynamics of Kepler's Candidate Multiple Transiting Planet Systems", ApJS **197**, 8 (2011).

Lodge, O., *Pioneers of Science* (Macmillan and Company, London, 1893).

Lopes, R. M. C., K. L. Mitchell, E. R. Stofan, J. I. Lunine, R. Lorenz, F. Paganelli, R. L. Kirk, C. A. Wood, S. D. Wall, L. E. Robshaw, A. D. Fortes, C. D. Neish, J. Radebaugh, E. Reffet, S. J. Ostro, C. Elachi, M. D. Allison, Y. Anderson, R. Boehmer, G. Boubin, P. Callahan, P. Encrenaz, E. Flamini, G. Francescetti, Y. Gim, G. Hamilton, S. Hensley, M. A. Janssen, W. T. K. Johnson, K. Kelleher, D. O. Muhleman, G. Ori, R. Orosei, G. Picardi, F. Posa, L. E. Roth, R. Seu, S. Shaffer, L. A. Soderblom, B. Stiles, S. Vetrella, R. D. West, L. Wye and H. A. Zebker, "Cryovolcanic features on Titan's surface as revealed by the Cassini Titan Radar Mapper", Icarus **186**, 395–412 (2007).

Malhotra, R., "The origin of Pluto's peculiar orbit", Nature **365**, 819–821 (1993).

Mastrapa, R. M., M. P. Bernstein, S. A. Sandford, T. L. Roush, D. P. Cruikshank and C. M. D. Ore, "Optical constants of amorphous and crystalline H_2O-ice in the near infrared from 1.1 to 2.6 μm", Icarus **197**, 307–320 (2008).

Mastrapa, R. M. E. and R. H. Brown, "Ion irradiation of crystalline H_2O-ice: Effect on the 1.65-μm band", Icarus **183**, 207–214 (2006).

Messenger, S., L. P. Keller, F. J. Stadermann, R. M. Walker and E. Zinner, "Samples of Stars Beyond the Solar System: Silicate Grains in Interplanetary Dust", Science **300**, 105–108 (2003).

Naoz, S., W. M. Farr, Y. Lithwick, F. A. Rasio and J. Teyssandier, "Hot Jupiters from secular planet-planet interactions", Nature **473**, 187–189 (2011).

Nesvorný, D., A. N. Youdin and D. C. Richardson, "Formation of Kuiper Belt Binaries by Gravitational Collapse", AJ **140**, 785–793 (2010).

Newman, S. F., B. J. Buratti, R. H. Brown, R. Jaumann, J. Bauer and T. Momary, "Photometric and spectral analysis of the distribution of crystalline and amorphous ices on Enceladus as seen by Cassini", Icarus **193**, 397–406 (2008).

Noll, K. S., W. M. Grundy, E. I. Chiang, J.-L. Margot and S. D. Kern, "Binaries in the Kuiper Belt", in "The Solar System Beyond Neptune", edited by Barucci, M. A., Boehnhardt, H., Cruikshank, D. P., Morbidelli, A., & Dotson, R., pp. 345–363 (University of Arizona Press, 2008a).

Noll, K. S., W. M. Grundy, D. C. Stephens, H. F. Levison and S. D. Kern, "Evidence for two populations of classical transneptunian objects: The strong inclination dependence of classical binaries", Icarus **194**, 758–768 (2008b).

Osip, D. J., J. L. Elliot, S. D. Kern, R. L. Millis and B. G. Marsden, "2001 QC298", Minor Planet Electronic Circulars p. 49 (2002).

Parker, A. H., J. Kavelaars, J.-M. Petit, L. Jones, B. Gladman and J. Parker, "Characterization of Seven Ultra-Wide Trans-Neptunian Binaries", Astrophys. J. (in press) (2011).

Parker, A. H. and J. J. Kavelaars, "Destruction of Binary Minor Planets During Neptune Scattering", ApJ **722**, L204–L208 (2010).

Peale, S. J., "Generalized Cassini's Laws", AJ **74**, 483 (1969).

Pedersen, B. M., N. Meyer-Vernet, M. G. Aubier and P. Zarka, "Dust distribution around Neptune - Grain impacts near the ring plane measured by the Voyager planetary radio astronomy experiment", J. Geophys. Res. **96**, 19187 (1991).

Perets, H. B. and S. Naoz, "Kozai Cycles, Tidal Friction, and the Dynamical Evolution of Binary Minor Planets", ApJ **699**, L17–L21 (2009).

Petit, J.-M. and O. Mousis, "KBO binaries: how numerous were they?", Icarus **168**, 409–419 (2004).

Pinilla-Alonso, N., R. Brunetto, J. Licandro, R. Gil-Hutton, T. L. Roush and G. Strazzulla, "The surface of (136108) Haumea (2003 EL61), the largest carbon-depleted object in the trans-Neptunian belt", A&A **496**, 547–556 (2009).

Pires dos Santos, P. M., S. M. Giuliatti Winter, R. Sfair and D. C. Mourão, "Small particles in Pluto's environment: effects of the solar radiation pressure", MNRAS **430**, 2761–2767 (2013).

Poppe, A. and M. Horányi, "The effect of Nix and Hydra on the putative Pluto-Charon dust cloud", Planet. Space Sci. **59**, 1647–1653 (2011).

Porter, S. B., S. J. Desch and J. C. Cook, "Micrometeorite impact annealing of ice in the outer Solar System", Icarus **208**, 492–498 (2010).

Porter, S. B. and W. M. Grundy, "Post-capture Evolution of Potentially Habitable Exomoons", ApJ **736**, L14 (2011).

Porter, S. B. and W. M. Grundy, "KCTF evolution of trans-neptunian binaries: Connecting formation to observation", Icarus **220**, 947–957 (2012).

Press, W. H., S. A. Teukolsky, W. T. Vetterling and B. P. Flannery, *Numerical Recipes: The Art of Scientific Computing* (Cambridge University Press, 2007), 3 edn.

Rabinowitz, D. L., K. Barkume, M. E. Brown, H. Roe, M. Schwartz, S. Tourtellotte and C. Trujillo, "Photometric Observations Constraining the Size, Shape, and Albedo of 2003 EL61, a Rapidly Rotating, Pluto-sized Object in the Kuiper Belt", ApJ **639**, 1238–1251 (2006).

Ragozzine, D. A., *Orbital dynamics of Kuiper Belt object satellites, a Kuiper Belt family, and extra-solar planet interiors*, PhD dissertation, California Institute of Technology (2009).

Roush, T. L., "Physical state of ices in the outer solar system", J. Geophys. Res. **106**, 33315–33324 (2001).

Sartoretti, P. and J. Schneider, "On the detection of satellites of extrasolar planets with the method of transits", A&AS **134**, 553–560 (1999).

Sato, M. and H. Asada, "Transiting Extrasolar Planet with a Companion: Effects of Orbital Eccentricity and Inclination", PASJ **62**, 1203–1213 (2010).

Scheeres, D. J., "Rotational fission of contact binary asteroids", Icarus **189**, 370–385 (2007).

Schenk, P. M. and K. Zahnle, "On the negligible surface age of Triton", Icarus **192**, 135–149 (2007).

Schlichting, H. E. and R. Sari, "The Ratio of Retrograde to Prograde Orbits: A Test for Kuiper Belt Binary Formation Theories", ApJ **686**, 741–747 (2008).

Schubert, G., J. D. Anderson, B. J. Travis and J. Palguta, "Enceladus: Present internal structure and differentiation by early and long-term radiogenic heating", Icarus **188**, 345–355 (2007).

Sheppard, S. S., D. Ragozzine and C. Trujillo, "2007 TY430: A Cold Classical Kuiper Belt Type Binary in the Plutino Population", AJ **143**, 58 (2012).

Showalter, M. R., D. P. Hamilton, S. A. Stern, H. A. Weaver, A. J. Steffl and L. A. Young, "New Satellite of (134340) Pluto: S/2011 (134340) 1", IAU Circ. **9221**, 1 (2011).

Showalter, M. R., H. A. Weaver, S. A. Stern, A. J. Steffl, M. W. Buie, W. J. Merline, M. J. Mutchler, R. Soummer and H. B. Throop, "New Satellite of (134340) Pluto: S/2012 (134340) 1", IAU Circ. **9253**, 1 (2012).

Simon, A. E., G. M. Szabó, K. Szatmáry and L. L. Kiss, "Methods for exomoon characterization: combining transit photometry and the Rossiter-McLaughlin effect", MNRAS **406**, 2038–2046 (2010).

Smith, B. A., L. A. Soderblom, D. Banfield, C. Barnet, R. F. Beebe, A. T. Bazilevskii, K. Bollinger, J. M. Boyce, G. A. Briggs and A. Brahic, "Voyager 2 at Neptune - Imaging science results", Science **246**, 1422–1449 (1989).

Smith, B. A., L. A. Soderblom, R. Beebe, D. Bliss, R. H. Brown, S. A. Collins, J. M. Boyce, G. A. Briggs, A. Brahic, J. N. Cuzzi and D. Morrison, "Voyager 2 in the Uranian system - Imaging science results", Science **233**, 43–64 (1986).

Spahn, F., N. Albers, M. Hörning, S. Kempf, A. V. Krivov, M. Makuch, J. Schmidt, M. Seiß and Miodrag Sremčević, "E ring dust sources: Implications from Cassini's dust measurements", Planet. Space Sci. **54**, 1024–1032 (2006).

Standage, T., *The Neptune File* (Walker and Company, New York, 2000).

Stansberry, J., W. Grundy, M. Mueller, S. Benecchi, G. Rieke, K. Noll, M. Buie, H. Levison, S. Porter and H. Roe, "Physical properties of trans-neptunian binaries (120347) salaciaactaea and (42355) typhonechidna", Icarus **219**, 2, 676–688 (2012).

Steffl, A. J. and S. A. Stern, "First Constraints on Rings in the Pluto System", AJ **133**, 1485–1489 (2007).

Stephens, D. C. and K. S. Noll, "Detection of Six Trans-Neptunian Binaries with NICMOS: A High Fraction of Binaries in the Cold Classical Disk", AJ **131**, 1142–1148 (2006).

Stern, S. A., H. A. Weaver, A. J. Steffl, M. J. Mutchler, W. J. Merline, M. W. Buie, E. F. Young, L. A. Young and J. R. Spencer, "A giant impact origin for Pluto's small moons and satellite multiplicity in the Kuiper belt", Nature **439**, 946–948 (2006).

Strom, R. G., "The solar system cratering record - Voyager 2 results at Uranus and implications for the origin of impacting objects", Icarus **70**, 517–535 (1987).

Sweatman, W. L., "Vector rational interpolation algorithms of bulirsch-stoer-neville form", The Royal Society Proceedings: Mathematical, Physical and Engineering Sciences **454**, 1975, pp. 1923–1932 (1998).

Szabó, G. M., K. Szatmáry, Z. Divéki and A. Simon, "Possibility of a photometric detection of "exomoons"", A&A **450**, 395–398 (2006).

Thiessenhusen, K.-U., A. V. Krivov, H. Krüger and E. Grün, "A dust cloud around Pluto and Charon", Planet. Space Sci. **50**, 79–87 (2002).

Thirouin, A., J. L. Ortiz, R. Duffard, P. Santos-Sanz, F. J. Aceituno and N. Morales, "Short-term variability of a sample of 29 trans-Neptunian objects and Centaurs", A&A **522**, A93 (2010).

Tholen, D. J., M. W. Buie, W. M. Grundy and G. T. Elliott, "Masses of Nix and Hydra", AJ **135**, 777–784 (2008).

Trilling, D. E. and G. M. Bernstein, "Light Curves of 20-100 km Kuiper Belt Objects Using the Hubble Space Telescope", AJ **131**, 1149–1162 (2006).

Trujillo, C. A., M. E. Brown, K. M. Barkume, E. L. Schaller and D. L. Rabinowitz, "The Surface of 2003 EL_{61} in the Near-Infrared", ApJ **655**, 1172–1178 (2007).

Tsiganis, K., R. Gomes, A. Morbidelli and H. F. Levison, "Origin of the orbital architecture of the giant planets of the Solar System", Nature **435**, 459–461 (2005).

Verbiscer, A. J., M. F. Skrutskie and D. P. Hamilton, "Saturn's largest ring", Nature **461**, 1098–1100 (2009).

Waite, J. H., M. R. Combi, W.-H. Ip, T. E. Cravens, R. L. McNutt, W. Kasprzak, R. Yelle, J. Luhmann, H. Niemann, D. Gell, B. Magee, G. Fletcher, J. Lunine and W.-L. Tseng, "Cassini Ion and Neutral Mass Spectrometer: Enceladus Plume Composition and Structure", Science **311**, 1419–1422 (2006).

Ward, W. R., "Protoplanet Migration by Nebula Tides", Icarus **126**, 261–281 (1997).

Weaver, H. A., S. A. Stern, M. J. Mutchler, A. J. Steffl, M. W. Buie, W. J. Merline, J. R. Spencer, E. F. Young and L. A. Young, "Discovery of two new satellites of Pluto", Nature **439**, 943–945 (2006).

Weidenschilling, S. J. and F. Marzari, "Gravitational scattering as a possible origin for giant planets at small stellar distances", Nature **384**, 619–621 (1996).

Wright, J. T., O. Fakhouri, G. W. Marcy, E. Han, Y. Feng, J. A. Johnson, A. W. Howard, D. A. Fischer, J. A. Valenti, J. Anderson and N. Piskunov, "The Exoplanet Orbit Database", PASP **123**, 412–422 (2011).

Yasui, M. and M. Arakawa, "Rate-dependent strength of porous ice - silica mixtures and its implications for the shape of small to middle-sized icy satellites", Icarus **210**, 956–967 (2010).

Youdin, A. N., K. M. Kratter and S. J. Kenyon, "Circumbinary Chaos: Using Pluto's Newest Moon to Constrain the Masses of Nix and Hydra", ApJ **755**, 17 (2012).

Young, L. A., S. A. Stern, H. A. Weaver, F. Bagenal, R. P. Binzel, B. Buratti, A. F. Cheng, D. Cruikshank, G. R. Gladstone, W. M. Grundy, D. P. Hinson, M. Horanyi, D. E. Jennings, I. R. Linscott, D. J. McComas, W. B. McKinnon, R. McNutt, J. M. Moore, S. Murchie, C. B. Olkin, C. C. Porco, H. Reitsema, D. C. Reuter, J. R. Spencer, D. C. Slater, D. Strobel, M. E. Summers and G. L. Tyler, "New Horizons: Anticipated Scientific Investigations at the Pluto System", Space Sci. Rev. **140**, 93–127 (2008).

Zhang, K. and D. P. Hamilton, "Orbital resonances in the inner neptunian system. II. Resonant history of Proteus, Larissa, Galatea, and Despina", Icarus **193**, 267–282 (2008).